MECHANICAL CHARACTERIZATION OF SILICON NANOWIRES

by

EVREN FATİH ARKAN

A Thesis Submitted to the
Graduate School of Engineering
in Partial Fulfillment of the Requirements for
the Degree of

Master of Science
in
Mechanical Engineering

KOC UNIVERSITY
DECEMBER 2011

Koç University
Graduate School of Sciences and Engineering

This is to certify that I have examined this copy of a master's thesis by

Evren Fatih Arkan

and have found that it is complete and satisfactory in all respects,
and that any and all revisions required by the final
examining committee have been made.

Committee Members:

____

B. Erdem Alaca, Ph.D. (Advisor)

____

Arda D. Yalçınkaya, Ph.D.

____

Yusuf Leblebici, Ph.D.

Date: ____

To my beloved parents and lovely sister

ABSTRACT

The challenge of mechanical characterization of silicon nanowires is addressed in this study by developing different devices and fabrication approaches for tensile and resonance-based testing. A novel microtensile device for the determination of elastic modulus and fracture strength of silicon nanowires is designed. An electromechanical simulation is carried out and a proposed fabrication flow is presented. Uniaxial deformation of the silicon nanowire is induced by an electrostatic comb actuator and the resulting displacements and load are measured by a triplate differential capacitive sensor. The silicon nanowire is positioned between the electrostatic comb drive and the triplate capacitive sensors. The issue of positioning and clamping is overcome by monolithic fabrication of silicon nanowires using the scalloping effect associated with the Bosch process. Analytical expressions for studying stability and linearity, including the effect of the electrostatic force generated by the excitation signal on the sensing electrodes, are derived and discussed for quasi-static applications. A MATLAB code is contrived for optimization of the device geometry. The overall performance of the device is examined via finite element analysis. A comparison with analytical results yields less than 1% deviation.

The same fabrication approach is utilized for dynamic mechanical characterization, where a combination of Bosch-process-based nanowire fabrication with surface micromachining and chemical-mechanical-polishing-based metal electrode/contact formation is employed to contrive a silicon nanowire resonator on an SOI wafer. Nanowires up to a length of 50 µm with a diameter of 200 nm are achieved while retaining submicron nanowire-to-electrode gaps specifically of 900 nm. The scalability of the technique is demonstrated through using no patterning method other than optical lithography on conventional SOI substrates. Structural integrity of double-clamped nanowires is evaluated through three-point bending test, where good clamping quality and fracture strengths of 14 GPa are observed.

As a result of the unique fabrication method the device exhibits perfect geometry for resonator and switch applications which are two areas of interest for CMOS-compatible electromechanical solutions. Resulting devices are characterized with all-electrical actuation and readout schemes. Resonance frequency of 1.97 MHz with a quality factor 75 is measured.

The resonance frequency is in close agreement with continuum modeling and indicates a tensile intrinsic stress of 2.8 MPa in silicon. Switch characterization is conducted by sweeping a voltage difference which is introduced between an electrode and the silicon nanowire. At a certain voltage difference pull-in occurs and the phenomenon exhibits itself as an abrupt increase in the current between the aforementioned electrode and silicon nanowire. Repeatable and hysteretic pull-in and pull-out behavior is found in a range of 30-40 V. The device exhibits an on/off current gain between 10 and 1000 depending on the light intensity of the experiment environment. The pull-in voltage can be further decreased by decreasing silicon nanowire-electrode gap or silicon nanowire radius.

Although exhibited performance parameters such as resonance frequency, quality factor and pull-in voltage are impractical for prospective appliance, they are highly malleable. By small alterations of the geometry of the device, such as nanowire diameter, length and nanowire-to-electrode gap, a diverse range of these parameters is producible. The fabrication process is also adjustable to fabricate silicon nanowire arrays perpendicular to the plane of substrate, enabling multiple nanowire devices along with single nanowire devices. Hence, a large spectrum of performance is addressable.

ÖZETÇE

İşbu araştırmada silisyum nanotellerin mekanik nitelendirme sorunu germe ve çınlanım temelli testler için çeşitli cihazlar ve üretim yöntemleri geliştirilerek ele alınmaktadır. Silisyum nanotellerinin esneklik modülü ve kırılma mukavemetinin tayini için yeni bir mikrogerme cihazı tasarlanmıştır. Söz konusu cihazın elektromekanik benzetimi gerçekleştirilmiş ve bir üretim akışı önerilmiştir. Tasarlanan cihazda silisyum nanoteller elektrostatik tarak tahrik mekanizması ile tek eksenli deformasyona uğrar ve doğan deplasman ve yük üçlü plakalı diferansiyel sığa sensörü ile ölçülür. Silisyum nanotel tahrik mekanizması ve yük sensörü arasına konumlandırılır. Nanotelin konumlandırılma ve mesnetlenme sorunları silisyum nanotellerin Bosch sürecinin kendine özgü oyma yöntemini kullanarak yekpare üretimi ile üstesinden gelinir. Kararlılık ve doğrusallık incelemeleri için gereken analitik çözümlemeler, tahrik sinyalinin oluşturacağı elektrostatik kuvvetin ölçüm elektrotlarına etkisi de göz önüne alınarak, durağan uygulamalar için tartışılmış ve türetilmiştir. Cihazın eniyilenmiş geometrisini elde etmek için bir MATLAB kodu türetilmiştir. Cihazın bütünlenmiş başarım incelemesi için sonlu eleman analizi kullanılmıştır. Analitik sonuçlarla yapılan karşılaştırma sonucu %1'den az bir sapma gözlenmiştir.

Devingen nitelendirme için, benzer bir üretim yaklaşımı benimsenerek Bosch süreci temelli nanotel üretimi ve kimyasal-mekanik-cilalama temelli metal elektrot tesisinden yararlanılmış ve bir SOI pulu üzerinde silisyum çınlaç üretilmiştir. 50 µm uzunluğa ve 200 nm çapa sahip nanoteller, 900 nm'lik nanotel-elektrot arası boşluklar korunarak elde edilmiştir. Kullanılan yöntemin ölçeklenebilirliği, standart SOI pulu üzerinde desenlendirme yöntemi olarak yalnızca optik litografi kullanılarak gösterilmiştir. Çift mesnetlenmiş nanotellerin yapısal bütünlüğü üç-nokta-bükme testi vasıtasıyla denetlenmiştir ve yüksek bağlama kalitesi yanı sıra 14 GPa kırılma mukavemeti gözlenmiştir.

Benzersiz imalat yönteminin bir sonucu olarak cihaz, CMOS uyumlu elektromekanik cihazlar arasında bulunan çınlaç ve şalter uygulamaları için mükemmel bir geometri sergilemektedir. Söz konusu uygulamalardan elektrik tahrik ve okuma kullanarak yararlanılmış ve cihazlar nitelendirilmiştir. Sonuç olarak çınlanım frekansı 1.97 MHz ve

kalite faktörü 75 olarak ölçülmüştür. Ölçülen çınlanım frekansı süreklilik modeli ile anlaşmakta olup, 2.8 MPa kadar bir içsel gerilmeye işaret etmektedir. Şalter nitelendirmesi elektrot ve silisyum nanotel arasında tanıtılan gerilim farkının süpürülmesi ile yürütülmüştür. Belli bir gerilim farkına ulaşıldığında "pull-in" kararsızlığı meydana gelmekte ve bu görüngü bahsi geçen elektrot ve nanotel arasında ani bir akım artışı olarak kendini sergiler. Cihazda 30-40 V arası tekrarlanabilir ve isterik çekme ve bırakma davranışı gözlenmiştir. Cihaz deney çevresinin ışık yoğunluğuna bağlı olmak üzere 10 ve 1000 arası açık/kapalı oranı teşhir etmiştir. Cihazın "pull-in" kararsızlık gerilimi silisyum nanotel çapının düşürülmesi veyahut silisyum nanotel ve elektrot arası boşluğun daraltılması ile mümkündür.

Gözlemlenen bazı başarım parametreleri arasında, çınlanım frekansı, kalite faktörü ve "pull-in" gerilimi gibi potansiyel uygulamalara elverişsiz görünen değerler elde edilmiş parametreler olsa da, bu değerler oldukça değişkendir. Cihaz geometrisinde silisyum nanotel çapı, uzunluğu ve nanotel-elektrot arası boşluk gibi çeşitli parametrelerde yapılacak küçük değişikliklerle geniş bir yelpazede başarım parametreleri elde edilebilir. Buna ilaveten üretim süreci pul yüzeyine dik silisyum nanotel dizinleri imal edecek şekilde ayarlanıp çoklu silisyum nanotel cihazları üretilebilir.

ACKNOWLEDGEMENTS

I would like to thank Dr. Erdem Alaca for welcoming me to work with his group and the guidance he has given me for the past three years and especially for the inexhaustible patience he has shown and wisdom he has shared with me throughout my study. I am deeply grateful to Prof. Yusuf Leblebici for his very much admired advices to my research and above all for inviting me to LSM-EPFL and providing me the opportunity of conducting my experiments. I am thankful to Dr. Arda Yalçınkaya for his recommendations on the improvements of the design.

I thank Christophe Canales for his crucial aid in mechanical characterization experiments, the CMI staff in their valuable suggestions for the fabrication flow and Dr. Selim Hanay for his precious suggestions for the characterization experiments.

I am deeply appreciative of Davide Sacchetto for being a patient and understanding mentor along with an invaluable friend throughout my stay in EPFL.

I am indebted to the greatest extent to my family for their amaranthine support and encouragement I cherished throughout my academic venture.

Alongside all these, I am deeply obliged to all my dearest friends İzzet Yıldız, Şeyda İpek, Osman Eryurt, Deniz Şanlı, Yasin Kılınç, Gökhan Nadar, Berkay Gümüş, İsmail Yorulmaz, Zuhal Taşdemir, Serhat Yavuz, Salih M. Kılıç, Erdal Uzunlar, Sibel Kalyoncu, İbrahim Gür and many more for the support and especially the many wonderful memories they have given me and made my last three years the most enjoyable years of my life.

This project was supported in part by TÜBİTAK under grant no. 104M216, and TÜBA-GEBİP.

TABLE OF CONTENTS

LIST OF TABLES ... xi
LIST OF FIGURES ... xi
NOMENCLATURE ... xv
Chapter 1 ... 1
INTRODUCTION ... 1
Chapter 2 ... 3
LITERATURE REVIEW ... 3
2.1. Testing Techniques ... 3
2.1.1. Simple uniaxial tensile test for NWs ... 3
2.1.2. Simple uniaxial tensile test chips for thin films ... 9
2.1.3. Resonance-based testing ... 13
2.1.4. Three-point bending ... 18
2.1.5. Static Bending Test ... 20
2.2. Size Dependency of Properties of Nanowires ... 21
2.3. Intrinsic Sample Properties Affecting Test Results ... 26
2.3.1. Intrinsic stress ... 26
2.3.2. Crystalline Orientation ... 31
2.3.3. Oxide Thickness ... 32
Chapter 3 ... 33
MICROTENSILE TESTING DEVICE ... 33
3.1. Model of the Microtensile Device ... 34
3.2. Actuator of the Microtensile Device ... 36
3.3. Load Sensor of the Microtensile Device ... 38
3.4. Design Criteria ... 39
3.4.1 Force and Displacement Demand of the Device ... 39
3.4.2 Simplicity of the Device ... 40
3.4.3 Stability of the Device ... 40
3.4.4 Nonlinearity of Measurements ... 43
3.4.5 Parametric Analysis ... 44
3.4.6 Finite Element Analysis ... 57
3.5. Proposed Fabrication Flow ... 66
Chapter 4 ... 73
RESONANCE AND THREE POINT BENDING CHARACTERIZATION ... 73
4.1 Introduction ... 73
4.2. System Architecture and Instrumentation ... 78
4.2.1 Nanoelectromechanical Resonator Geometry and Instrumentation ... 79
4.2.2 Nanoelectromechanical Switch Geometry and Instrumentation ... 82

4.3. Fabrication 84
4.4. Results and Discussion 88
4.4.1 Resonator Characterization 88
4.4.2. Switch Characterization 91
4.4.3. Three-Point Bending Results 93
Chapter 5 95
CONCLUSION 95
Appendix A 97
MATLAB CODE OF PARAMETRIC ANALYSIS 97
Appendix B 104
MATLAB DESIGN CODE 104
Appendix C 113
RESONANCE CHARACTERIZATION EXPERIMENTS 113
Appendix D 118
SWITCH CHARACTERIZATION EXPERIMENTS 118
BIBLIOGRAPHY 126

LIST OF TABLES

Table 2.1: Comparison of modulus of elasticity of NWs and bulk…………………………...25
Table 3.1: Variable values of actuator and load sensor………..…………………………….57

LIST OF FIGURES

Figure 2.1: Mechanical model of uniaxial tensile test………………………………….………....4
Figure 2.2: a) Suspended NW. b) Free-standing NW suspended between device jaws [8]........5
Figure 2.3: a) SEM micrograph of the device used by Desai and Haque. b) Posts fabricated on the jaw. Posts were fabricated by FIB to ensure strong gripping [7]……..……….…………..5
Figure 2.4: a) Uniaxial tensile test chip with electrostatic comb actuators. b)Microcompression test chip fabricated by Espinosa [9]...………………....………..……......6
Figure 2.5: a) SEM micrograph of the chip fabricated by Espinosa b) NW specimen suspended between thermal actuator and load sensor. Specimen ends were welded to the testing system by electron beam induced deposition of platinum [11]………………………...7
Figure 2.6: a) Uniaxial tensile test chip and b) Microcompression test chip fabricated by Zhang *et al* [12]…………………………………….……………..……………………..…8
Figure 2.7: Schematic of the electrical connections of the tensile testing device fabricated by Zhang *et al*. Inset: SEM image of a cobalt nanowire bridging on a gap [12]..........................8
Figure 2.8: a) SEM image of the MEMS-based loading device. b) Finite element simulation of the device operation, and enlarged views of c) the specimen and d) the displacement sensors [13]……………………………………………….……...……...………………...………..9
Figure 2.9: Schematic of the tensile testing device designed by Haque and Saif. The set of verniers are cofabricated with the actuator are used to measure its axial displacement [14]...10
Figure 2.10: Schematic of the tensile testing device manufactured by Haque and Saif showing its various components [15]...……11
Figure 2.11: a) Schematics of test structure of device manufactured by Gaspar *et al* b) Schematic overview of fabrication process c) Sample measured force-deflection curves [16]……………………………………………………………...……....……………12

Figure 2.12: a) Schematic view and b) enlarged view of the structure of microtensile device manufactured by QinHua *et al* [17]..13

Figure 2.13: Simplification of a resonance-based test……...…..14

Figure 2.14: a) SEM image of a Ge NW cantilever: the NW is attached to the Cu substrate with Pt deposited by electron beam-induced deposition in the SEM/FIB tool. b) SEM image of a Ge NW vibrating in response to a sinusoidal potential applied by the nearby tungsten probe. (Inset) Device schematic [18]...……15

Figure 2.15: Electron micrographs of the electromechanical deflections of a carbon NT Uncharged NT (V_s=0) b) Charged NT (V_s=20 V) Here an electrical potential difference was applied between the NT (which was connected to a NT fiber) and a counterelectrode (not shown) [19]...…16

Figure 2.16: Simple configuration of three point bending………….....................…………18

Figure 2.17: a) AFM image of a SWNT rope adhered to the polished alumina ultrafiltration membrane, with a portion bridging a pore of the membrane [28]…............................……19

Figure 2.18: Simple configuration of static bending test.......................................……..21

Figure 2.19: Measurement setup for the detection of the resonance frequency of a microbeam [43]………...28

Figure 2.20: A sketch of intrinsic stress gauge designed by Lin *et al* [44]...........................29

Figure 2.21: a) A sketch and b) an SEM micrograph of the intrinsic stress gauge designed by Ericson *et al* [45]..…29

Figure 2.22: Schematic of released spiral and deformation parameters: rotation angle Δθp, change of the lateral size ΔR = R2 −R1, and structure height h at the free end point P [47]...30

Figure 2.23: Etch pattern emerging on a wagon wheel mask on a <100> wafer [48]...........31

Figure 3.1: Top view of the microtensile testing device. All units are in meters……...............34

Figure 3.2: Spring mass model of the microtensile testing device…...................................35

Figure 3.3: Schematic illustration of close-up view of a single pair of interdigitated comb fingers……...…37

Figure 3.4: Schematic illustration of close-up view of a single pair of interdigitated comb fingers of load sensor [12]...…38

Figure 3.5: Graphical solution of a tri-plate load sensor. The area in red is the area subsequent pull-in instability……...42

Figure 3.6: Effects of a) d_1, b) V_e, c) b and d) $\tilde{x}_m$ on the total induced capacitance difference of the load sensor. ……...46

Figure 3.7: Effects of a) d_1,b) V_e,c) b and d) $\tilde{x}_m$ on the nonlinearity of the load sensor. Nonlinearity due to displacement is indicated in red whereas the nonlinearity due to electrostatic force is indicated in blue……..49
Figure 3.8: Effects of a) d_1, b) V_e, c) b and d) $\tilde{x}_m$ on the stability of the load sensor. The area in red denotes the area subsequent pull-in instability……..…51
Figure 3.9: Effects of a) d_1, b) b and c) $\tilde{x}_m$ (here denoted as x_fracture/d1) on the number of load sensor finger sets needed………...53
Figure 3.10: Effects of a) g_x and b) g_y on the number of actuator comb fingers needed…...55
Figure 3.11: Effects of a) g_x and b) g_y on the distance of pull-in instability…....................…..56
Figure 3.12: The deformed form of initial actuator analysis……..58
Figure 3.13: The deformed form of second actuator analysis…………..................................59
Figure 3.14: The deformed form of final actuator analysis…..…60
Figure 3.15: Displacement vs applied voltage graph and graph of the difference. The theoretical displacement is in blue and FEM simulation result is in red…………..............61
Figure 3.16: Capacitance difference vs displacement graph of FEM and theoretical results. Theoretical result is in blue and FEM result is in red……...63
Figure 3.17: Deformed form of half load sensor……………………………........................63
Figure 3.18: Deformed form of full load sensor……………………….................................64
Figure 3.19: Voltage induced on the movable plate of the load sensor due to displacement...65
Figure 3.20: Voltage induced on the movable plate of the load sensor due to displacement. Theoretical result is in blue and FEM result is in red……………………….................…65
Figure 3.21: Fabrication flow of the microtensile testing device. a) The left side demonstrate the AA' cross-section and the right side demonstrate the BB' cross-section as shown. a) LPCVD SiO_2 growth c) e-beam lithography d) Oxide etch e) PR strip f) Photolithography g) Oxide etch h) PR strip i) Bosch process j) Oxidation k) Photolithography l) Oxide etch m) Cr-Au evaporation n) PR strip o) Oxide etch………………………….....................................72
Figure 4.1: Different approaches to single-crystalline SiNW formation using top-down patterning and etching……………………………...76
Figure 4.2: SEM image of the device.......................................……………………………79
Figure 4.3: Schematic setup for resonator application……………………….......................80

Figure 4.4: Schematic of the switch application setup. -40 V was applied from port A and the voltage applied by port B was swept from -40 to 40 V. The current between the ports C and D was measured. Inset is the micrograph of a SiNW after pull-in……………………………......83

Figure 4.5: Fabrication flow of the device a) Hard mask definition b) ICP-DRIE c) Oxidation d) Metal coating e) PR coating f) CMP g) Al etch h) Oxide etch………………….....................87

Figure 4.6: a) Direct results obtained from the network analyzer. b) Differential signal readout indicating net motional/dynamic current. Inset provides a close-up view of the obtained peak indicating strong dependence of the obtained signal on SiNW bias………………..................90

Figure 4.7: a) Effect of incident white light on the magnitude of current jump upon pull-in. b) Hysteretic behavior of the switch……………………..….92

Figure 4.8: Scanning electron micrographs of a loading sequence in three-point bending configuration. In three-point bending samples, Al electrodes are etched deliberately to provide space for probe motion and SiNW bending deflection…………………………....................94

NOMENCLATURE

NT/CNT	Nanotube / Carbon nanotube
NW/ SiNW	Nanowire / Silicon nanowire
NEMS/MEMS	Nano / Micro electro mechanical systems
SEM/TEM	Scanning / Transmission electron microscope
FIB	Focused ion beam
FEBID/FIBID	Focused electron / ion beam induced deposition
RIE/DRIE	Reactive / Deep reactive ion etching
ICP-DRIE	Inductively coupled plasma deep reactive ion etching
SCS	Single crystal silicon
AFM	Atomic force microscope
FEA	Finite element analysis
SOI	Silicon on insulator
LPCVD	Low pressure chemical vapor deposition
PR	Photoresist
VLS	Vapor-liquid-solid
CMP	Chemical mechanical polish
BOX	Buried oxide layer
ω_{res}	Fundamental resonance frequency
β	First mode shape parameter
I	Moment of inertia
E/ E_e	Modulus / Effective modulus of elasticity
L/l	Length of the beam
δ_{beam}	Deflection
F	Force
A_s	Cross-section area of the sample
σ	Uniaxial tensile stress
ε	Strain
F_s	Force on the sample
F_{ls}	Force on the load sensor
F_{ac}	Force on the actuator springs
U_{ac}	Actuator displacement
U_{ls}	Load sensor displacement
ΔU_s	Difference in length of the sample
k_{ac}	Actuator spring constant
k_{ls}	Load sensor spring constant
k_s	Sample spring constant
F_{es}	Electrostatic force
V	Voltage difference on the actuator
l_s	Length of the sample
w	Width of each comb finger
t	Zero voltage overlap length between the fingers
g_x, g_y	Gap distances in x- and y-directions
x	Displacement in x-direction
W_{es}	Electrostatic work
C_{total}	Total capacitance
h	Height of the device

N_{ac}, N_{ls}	Number of fingers of the comb drive and load sensor
ε_0	Permittivity of the free space
l	Length of the fingers
d_1, d_2	Initial gap distances between movable and fixed fingers
ΔC	Capacitive difference
V_{out}	Voltage obtained by the load sensor
V_e	Voltage applied on the fixed fingers
a	A constant that depends on interface dynamics
F_{net}	Net force
F_{mech}	Restoring force or mechanical force
F_t	External force
δ	Ratio between electrostatic force and the restoring force
b	Ratio between d_2 and d_1
$\tilde{x}$	Ratio between x and d_1
$\tilde{x}_m$	Maximum displacement of the movable finger
NL_d	Nonlinearity due to displacement
k_{eff}, K_{eff}	Effective spring constant
NL_F	Force measurement nonlinearity
I	Total current
I_p	Parasitic current
I_m	Motional current
C_p	Parasitic capacitance
V_{dc}, V_{ac}	DC , AC voltage
ε_s	Longitudinal strain
ρ	Density
V_{PI}	Pull-in voltage
d_0	Zero-voltage gap between SiNW and read-out electrode
b_{eff}	Effective stiffness
b	Width of the SiNW
N	Axial force

Chapter 1

INTRODUCTION

Nanotechnology uses a great variety of structures. These structures not only vary in material but also in size and shape. This wide range of nanoentities such as nanotubes (NTs) and nanowires (NWs) has created vast potential applications. Moreover these nanoentities have superior properties compared to bulk materials and broaden their area of application. These differences are mainly caused by the surface effects dominating below a critical size. These surface effects alter some of the mechanical properties such as the modulus of elasticity, tensile strength and fracture strength of the material. However, to build reliable systems understanding the governing deformation and failure mechanisms and testing the physical properties of these nanostructures have crucial importance. Furthermore the dependence of physical properties on the size and crystalline orientation of the material becomes an issue in nanostructures. Numerous techniques were introduced for nanomechanical characterization of different nanostructures. The techniques can be listed as:

- Uniaxial tensile test
- Resonance-based test
- Three-point bending test
- Static bending test

Nanomechanical characterization is crucial for every nanostructure. However, this study focuses on nanomechanical characterization of Si nanowires (SiNWs). SiNWs have been the focus of intense research efforts for the last few decades. They are known to impart valuable capabilities to existing systems thanks to a variety of interesting physical properties including giant piezoresistivity due to electron and hole trapping [1], fracture strengths approaching the theoretical strength of crystalline Si [2] and ultra-high resonance frequencies on the order of hundreds of MHz [3]. Their uses within nanoelectronic and nanoelectromechanical systems (NEMS) are especially appealing due to their compatibility with existing process

technologies. This compatibility raises the possibility of batch processing and hence constitutes a major advantage for system-level integration.

In this study, a comprehensive review and examples of the aforementioned nanomechanical characterization methods for SiNWs is submitted.

Chapter 2 provides necessary background and literature review on nanomechanical characterization. The fundamentals of each method are explained along with examples in literature.

Chapter 3 describes the design and fabrication flow of a microtensile testing device for SiNWs. The design procedures for the fundamental elements of the device are explained in detail. Afterwards, finite element analysis of each element is carried out. Finally, a fabrication flow for this device is proposed.

A resonance based and three point bending nanomechanical characterizations of SiNWs are given in Chapter 4. A novel device designed by Yildiz *et al* [4] is utilized in these characterizations. A novel fabrication method was contrived for this device. The fabrication process is the first of its kind and challenging. Therefore optimization and development is still under study. The device geometry and instrumentation is explained thoroughly followed by conclusion of these characterizations.

The thesis is concluded with a short summary of the performed study and future research proposals.

Chapter 2

LITERATURE REVIEW

2.1. Testing Techniques

Nanomechanical characterization utilizes numerous methods. The nanostructures are deformed utilizing different actuation methods and the deformations are measured tractably. The techniques can be categorized as:

- Uniaxial tensile test
- Resonance-based test
- Three-point bending test
- Static bending test

2.1.1. Simple uniaxial tensile test for NWs

The uniaxial tensile test is the most common test used in macro structures to obtain the modulus of elasticity. Commercial testing devices are available for samples of a few millimeters of diameter. However, as the sample size decreases to micro or nanometer scale the test mechanism becomes harder to construct. The main purpose of the test mechanism is to measure the force and the displacement of the sample as it is loaded under uniaxial load. The most simplified mechanism of uniaxial tensile testing at microscale is constructed with the sample and two springs of known stiffness. A simple representation can be found in Figure 2.1. The displacements of the springs and the load are measured, where the difference of the displacements indicates the strain in the sample. Modulus of elasticity can thus be calculated.

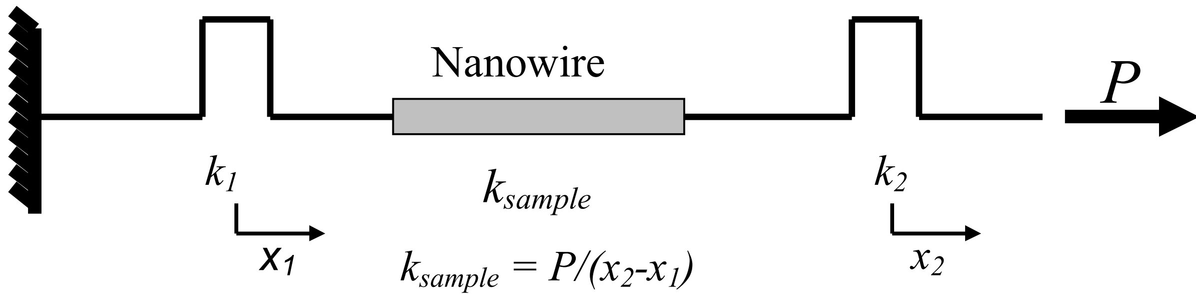

Figure 2.1: Mechanical model of uniaxial tensile test

Generally AFM tips are used for uniaxial tensile testing as they can measure force reliably. Yu *et al* [5] used two AFM tips to measure strain and force by attaching multi-walled carbon NTs using a solid carbonaceous deposit between them. By moving the AFM tips apart, the sample was loaded in tension. The loading of the NTs was carried out in a scanning electron microscope (SEM). Hence, measurement of the displacement of both AFM tips and the NT was carried out in SEM. Load was applied until the sample fractured and fractured samples were investigated under transmission electron microscope (TEM).

AFM tip was also used by Kizuka *et al* [6]. The sample tested was a Si NW of 6 nm diameter that was grown between the Si base and the AFM tip and was loaded until fracture. The testing was conducted under high resolution TEM providing elaborate observation of the strain and deformation process.

Apart from AFM tips MEMS devices have also been constructed to measure force and displacement throughout testing. One such chip was manufactured by Desai and Haque [7]. The substrate was of Si and consisted of two main bodies with a trench between them. One side of the trench was fixed to the base and other was mobile. ZnO NWs synthesized elsewhere were dispersed in methanol by ultrasonication. The drop of methanol with ZnO NWs was introduced to a free standing oxide grid. Methanol was evaporated and some NWs were suspended over a hole of the porous material. After an appropriate NW was located, it was fixed with focused ion beam (FIB) platinum deposition (Figure 2.2.a). The grid was then cut using FIB and fixed to a tungsten probe with FIB Pt deposition. The grid was manipulated to the jaws of the device. FIB was used to detach the tungsten probe and attach the grid to the jaws of the device (Figure 2.2.b). Loading was carried out under SEM. The external force actuator was piezoelectric. Post-buckling mechanics was used to measure the force. As the displacement was applied to the chip, the slender columns that are shown in Figure 2.3

buckled. Lateral displacements (as shown in Figure 2.3) of the buckled beams were dependent on the force. Due to their very low stiffness; they acted as high resolution force sensors. Lateral displacements were also used as displacement sensors due to their amplification vertical deformation. The displacements were measured from micrographs.

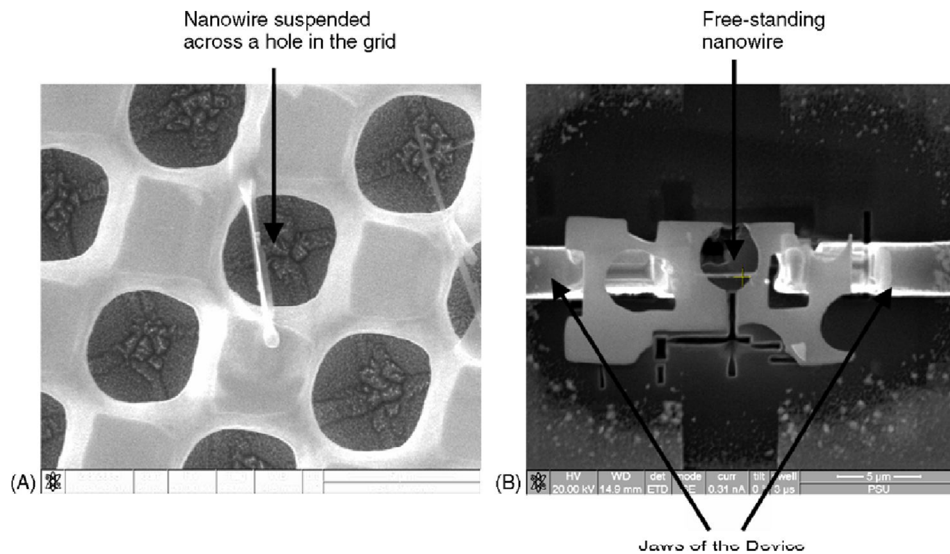

Figure 2.2: a) Suspended NW.

b) Free-standing NW suspended between device jaws [8]

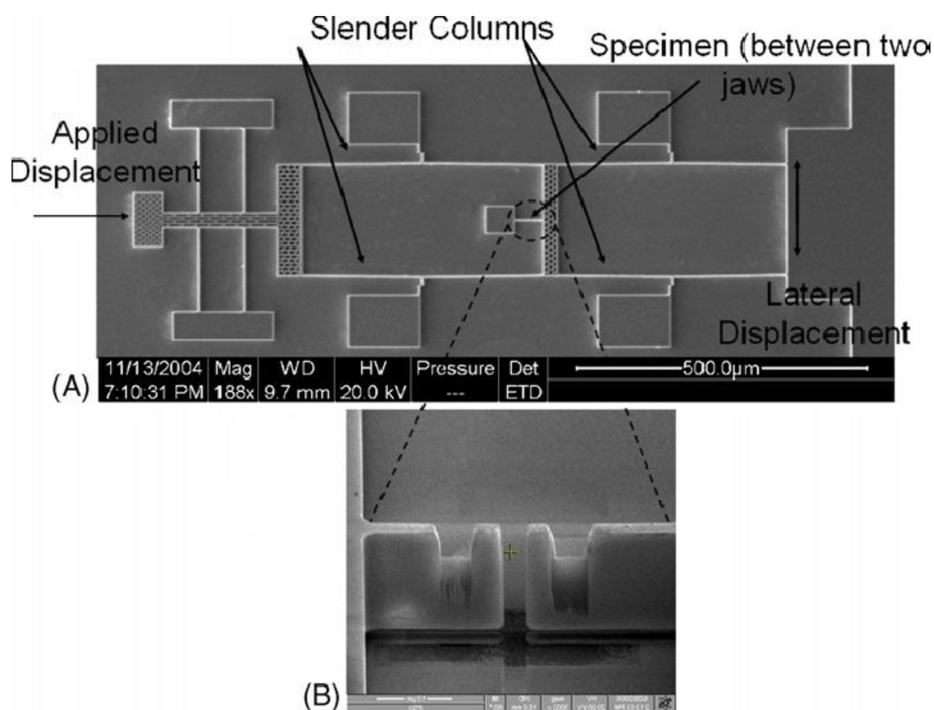

Figure 2.3: a) SEM micrograph of the device used by Desai and Haque.

b) Posts fabricated on the jaw. Posts were fabricated by FIB to ensure strong gripping. [7]

The device fabricated by Espinosa *et al* [9] was also Si (Figure 2.4 and Figure 2.5). The device consisted of two bodies with a trench between them. Thermal actuators were on one of the bodies and capacitive load sensors on the other body. The sample was placed between the bodies and on the trench. The aforementioned logic of using two springs with known stiffness was used in this chip. The thermal actuator is displacement-controlled. Therefore its displacement was known by the voltage difference applied between the anchors on either side of the actuator. Capacitive differential sensing was used to measure the displacement of the load sensor. The range of the load sensor was designed considering the sample properties. The stiffness was measured through resonance testing to minimize calculation errors. Hence, by multiplying the displacement with the stiffness of the folded beams the force could be calculated. To minimize parasitic capacitive effects the load sensor was placed as close to the sample as possible. The difference of the displacements of the thermal actuator and the load sensor would be the displacement of the sample. A hole was etched in the substrate beneath the sample so that it could be used under TEM. The sample of interest would be micropipette manipulated and afterwards attached to the chip by FIB Pt deposition. Figure 2.4 displays the chip and a sample over the trench. Similar chips with the same approach were fabricated with electrostatic comb actuators instead of thermal actuators and reversed thermal actuators for compression testing (Figure 2.4.) [10]

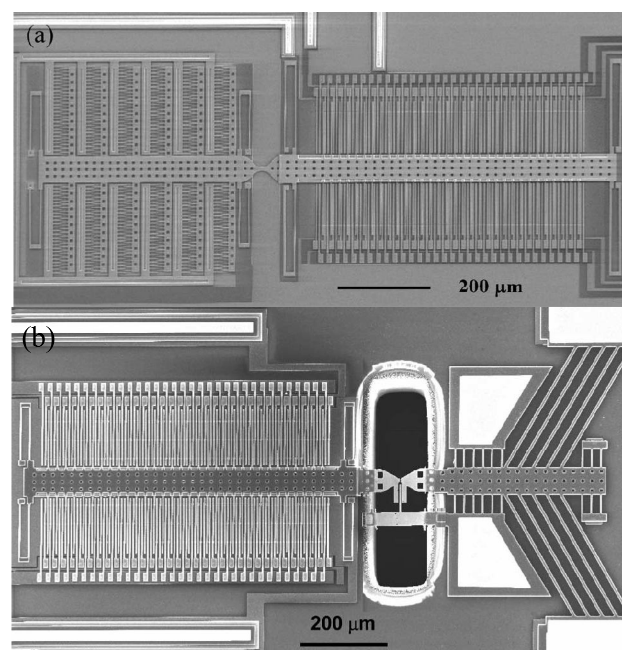

Figure 2.4: a) Uniaxial tensile test chip with electrostatic comb actuators.
b)Microcompression test chip fabricated by Espinosa [9]

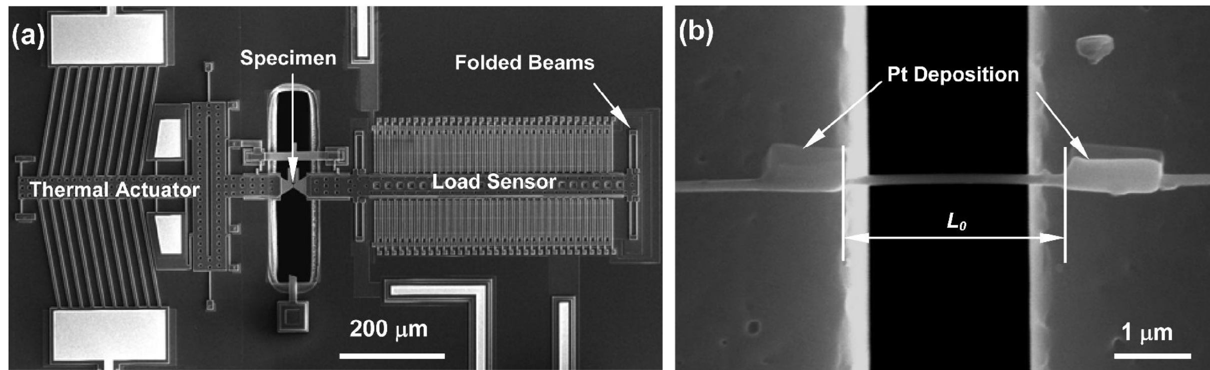

Figure 2.5: a) SEM micrograph of the chip fabricated by Espinosa
b) NW specimen suspended between thermal actuator and load sensor.
Specimen ends were welded to the testing system by electron beam induced deposition of platinum. [11]

Zhang *et al* [12] also manufactured microtensile and microcompression testing devices from Si. The device consisted of a trench between the actuator and load sensor for tensile testing and a trench between a fixed body and actuator and load sensor attached for compression testing as seen in Figure 2.6. Electrostatic actuators and capacitive load sensors were used. The sample was placed on the trench. The aforementioned logic of using two springs with known stiffness was used in this chip. By applying voltage difference between the anchors on either side of the actuator compressive or tensile force is applied on the sample. Capacitive differential sensing was used to measure the displacement of the load sensor. The range of the load sensor was designed considering the sample properties. The stiffness of the load sensor and actuator springs was measured through resonance testing to minimize calculation errors. Hence, by multiplying the displacement with the stiffness of the folded beams the force could be calculated. A hole was etched in the substrate beneath the sample so that in situ TEM testing is enabled. Moreover the MEMS device was designed to enable electrical conductance experiments on the samples as seen in Figure 2.7. Samples were positioned on the trench using a pick-and-place nanomanipulation and fixed via focused electron/ion beam induced deposition (FEBID/FIBID) of copper-carbon composite as seen in the inset of Figure 2.7. Samples were removed from the device after the experiments by the means of FIB milling to enable reusability.

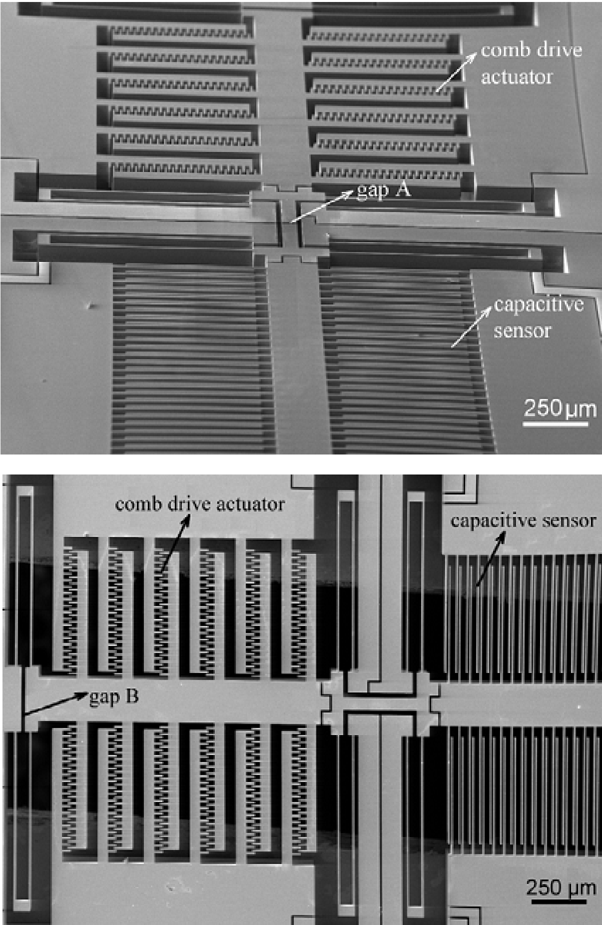

Figure 2.6: a) Uniaxial tensile test chip and b) Microcompression test chip fabricated by Zhang *et al* [12]

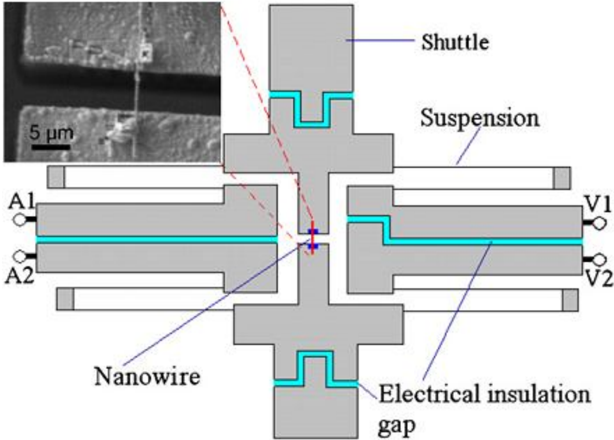

Figure 2.7: Schematic of the electrical connections of the tensile testing device fabricated by Zhang *et al*. Inset: SEM image of a cobalt nanowire bridging on a gap. [12]

2.1.2. Simple uniaxial tensile test chips for thin films

MEMS are also used for mechanical property measurement of thin films. The design of these chips is of great help to overcome problems associated with micro material testing. The approach is the similar as before. The sample is loaded between a spring of known stiffness and a fixed end.

The MEMS device manufactured by Hosokawa *et al* [13] was of Si. The device consisted of a mobile and fixed part similar to the one manufactured by Desai and Haque [7]. The sample of interest was Al and Au thin films. Al and Au thin films were positioned over the trench by a pick-and-place device. After correctly positioning, the sample was attached to the test frame and notched using FIB Pt deposition. The notch radius was needed to calculate plane stress fracture toughness. Loading of the specimen was carried out in SEM with an external piezomotor. The force, displacement of the specimen and the displacement of the slender beams were calculated from the lateral displacement of the buckled slender beams and the vernier gauges connected to the slender beams. Figure 2.8 displays the device and the finite element simulation of slender beams. The lateral displacement was measured from micrograph. The samples were loaded until fracture.

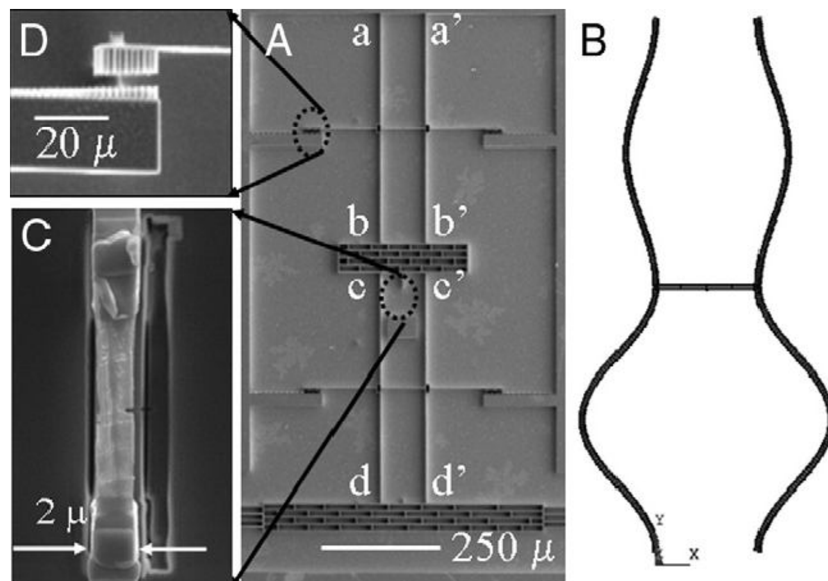

Figure 2.8: a) SEM image of the MEMS-based loading device.
b) Finite element simulation of the device operation, and enlarged views of
c) the specimen and d) the displacement sensors. [13]

A different design by Haque and Saif [14] was able to test different thin film samples. The device was fabricated out of Si and consisted of an electrostatic comb drive actuator and a static microgripper as it can be seen in Figure 2.9. The loading was measured with the use of a force calibration beam. Similar to [13], during loading the beam experienced compressive force and buckled. Hence reading the displacements of the chip and the beam, the strain and force could be calculated. One disadvantage was that the samples had to be specially manufactured so that the gripper could hold the sample. Moreover the alignment between the sample and the chip had to be carefully corrected so that no bending was introduced in the sample.

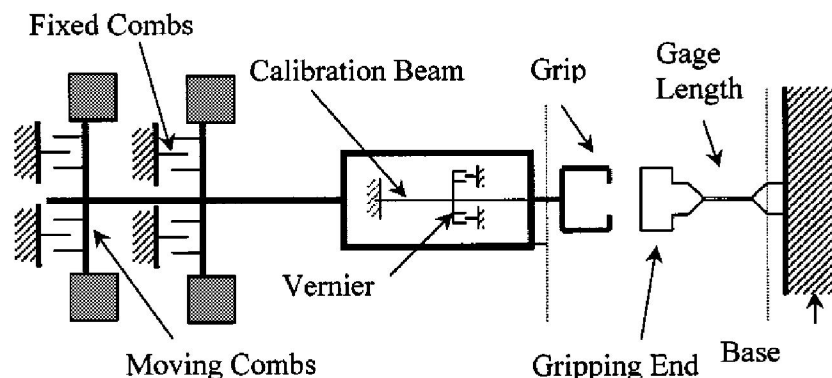

Figure 2.9: Schematic of the tensile testing device designed by Haque and Saif [14] The set of verniers are cofabricated with the actuator are used to measure its axial displacement.

Haque and Saif [15] also manufactured a displacement-based tensile tester which can be seen in Figure 2.10. The sample was placed between an actuator and a clamped-clamped beam which acted as a force sensor. The sensor had a gap between the main body of the chip and itself that worked as a displacement sensor. The displacement measured could be multiplied with the stiffness of the force sensor to calculate the force. The other side of the sample was fixed to a rigid backbone supported by springs to guarantee only uniaxial loading was introduced to the sample by preventing rotations. Another displacement sensor similar to the previous read the displacement of this end of the sample. The difference of the measured displacements was equal to the elongation of the sample. Hence, the force displacement curve could be plotted. The samples were assembled with the use of a pick and place device. The adhesion between Si substrate and the sample was generally sufficient. However, for

materials with poor adhesion to Si such as Au an intermediate layer (Ti for example) was used.

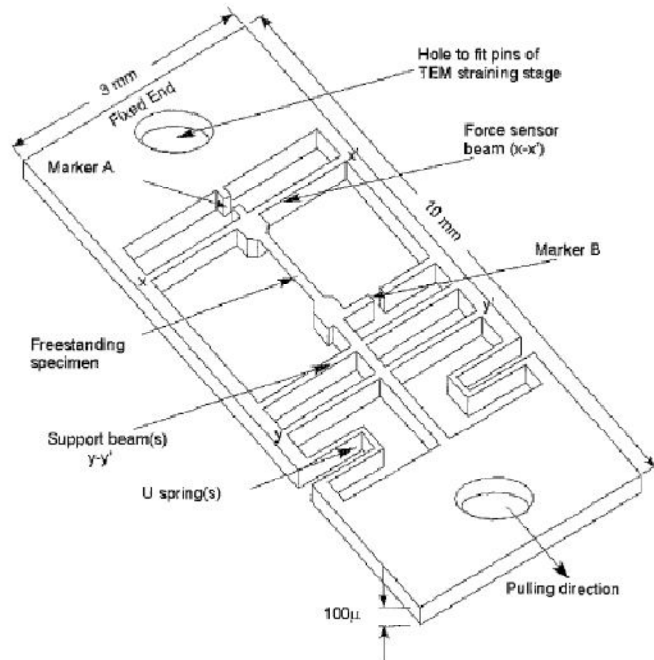

Figure 2.10: Schematic of the tensile testing device manufactured by Haque and Saif showing its various components [15]

A similar working principle was used to measure the modulus of elasticity of poly crystalline silicon (poly Si), Si nitride (SiN_x) and Al by Gaspar *et al* [16]. In the microtensile testing device manufactured by Gaspar *et al* the specimen stated between the substrate and mobile part as seen in Figure 2.11. The mobile portion of the device consisted of parallel springs and a large frame (>1 mm^2). The specimen material was evaporated on the substrate and patterned into microtensile specimens using reactive ion etching (RIE) before the Si was etched by deep RIE (DRIE) (Figure 2.11.a). The loading was applied to the frame by a commercial piezoactuator. The displacement was measured by a laser-deflection position sensor and loading was measured by a commercial force sensor. The measured force deflection curve was of the resultant of the specimen, the parallel springs, load cells and substrate. To determine the load cell and substrate stiffness the loading was carried out on devices with no specimen. To extract the specimen stiffness test were carried on beyond the

fracture. The difference between the measured stiffness before and after fracture, as seen in Fig. 9, provided the stiffness of the specimen.

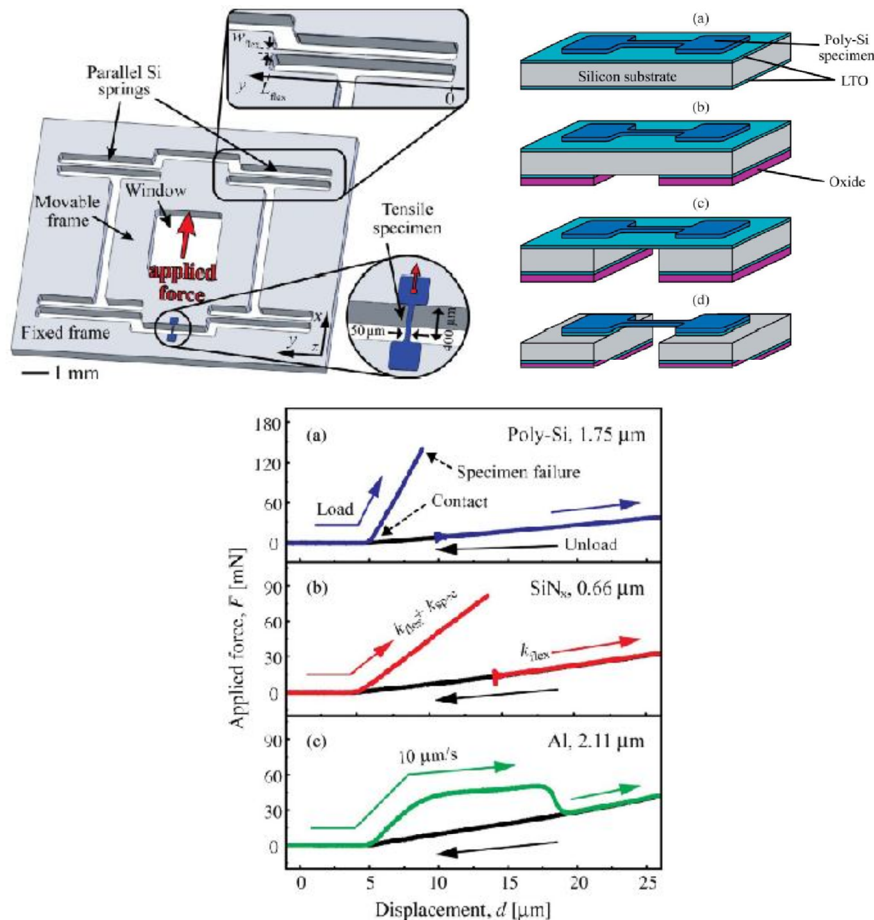

Figure 2.11: a) Schematics of test structure of device manufactured by Gaspar *et al*

b) Schematic overview of fabrication process

c) Sample measured force-deflection curves [16]

QinHua *et al* [17] tested single crystal Si (SCS) nanobeam through a similar device. The specimen was stated between a force sensor beam and electrostatic actuators as seen in Figure 2.12. An electrobeam hole was etched to integrate the device to TEM. SCS was evaporated on the wafer and microtensile structures were etched. Loading was carried out in TEM. To exterminate any bending forces three supporting beams were etched on the actuator side. The displacement of the nanobeam and displacement of force sensor beam were measured from micrographs.

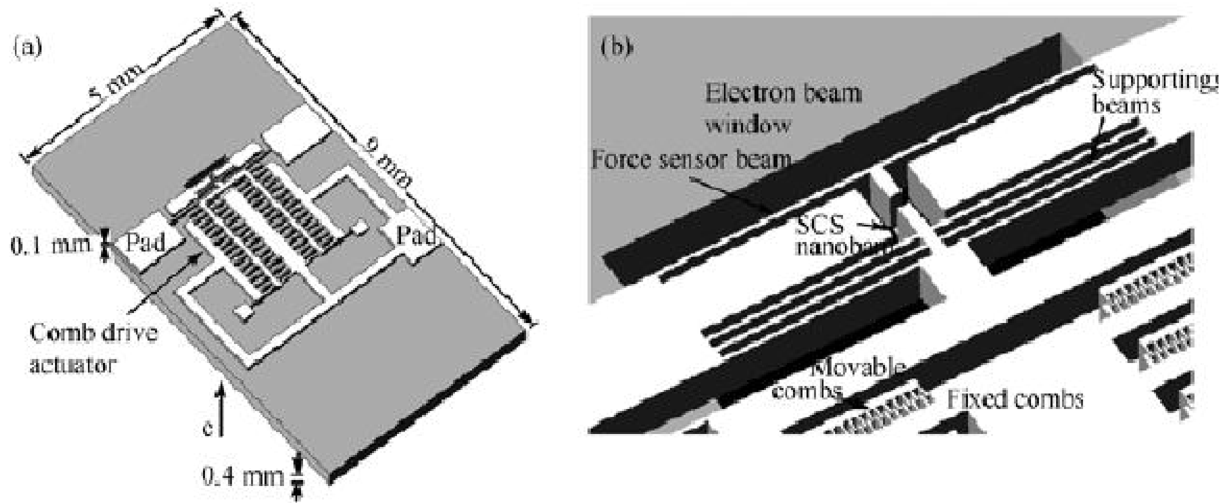

Figure 2.12: a) Schematic view and b) enlarged view of the structure of microtensile device manufactured by QinHua *et al* [17]

2.1.3. Resonance-based testing

The main idea of resonance-based testing is that the first modal resonance frequency is dependent on modulus of elasticity. The equation of the first modal resonance frequency of the commonly used system, fixed-free system, can be written as:

$$\omega_{\mathrm{res}} = (\beta^2 / 2\pi)(EI / m)^{1/2} / L^2 \qquad (2.1)$$

where ω_{res} is the fundamental resonance frequency, $\beta = 1.875$, *EI* is the flexural rigidity (or bending stiffness), *E* is the modulus of elasticity, *I* is the moment of inertia about a particular axis of the rod, *L* is the length of the beam, and *m* is its mass per unit length. The NWs are brought to mechanical resonance. Then by measuring the frequency and other parameters the modulus of elasticity is obtained.

For the NW to be in resonance, reciprocating force actuation is needed. The most common procedure is applying a DC and AC field between two electrodes. The NW of the material of interest should be fixed to one of the electrodes as it can be seen in Figure 2.13.

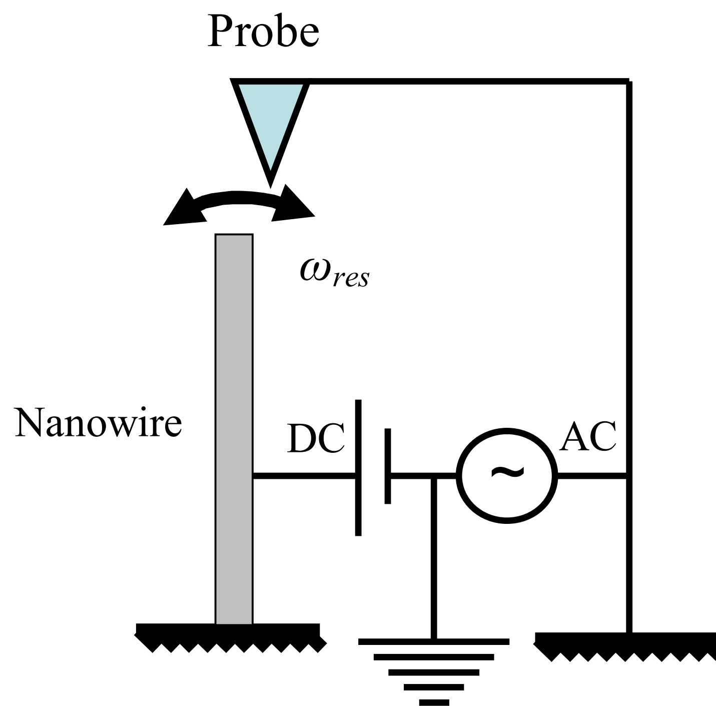

Figure 2.13: Simplification of a resonance-based test

Smith *et al* [18] measured the modulus of elasticity of Ge NWs through resonance analysis. Figure 2.14 shows the SEM images of Ge NWs attached to Cu substrate and the NW oscillating. Ge NWs were grown separately and then were dispersed in chloroform. The droplet was then dried over a lacey carbon TEM grid. After a series of procedures the NWs were glued to the copper substrate by electron-beam-induced Pt deposition. The NWs were then actuated at resonance by introducing two tungsten probes, one within a distance of one micrometer to the free end of the NW and the other one touching the Cu substrate. AC current was applied to both probes. A frequency sweep of the AC current was conducted in SEM and fine tuning was carried out by the images of the oscillating NW until resonance was observed. Along with the resonant frequency, NW length, vibrational amplitude and tilt angle were measured from the SEM images.

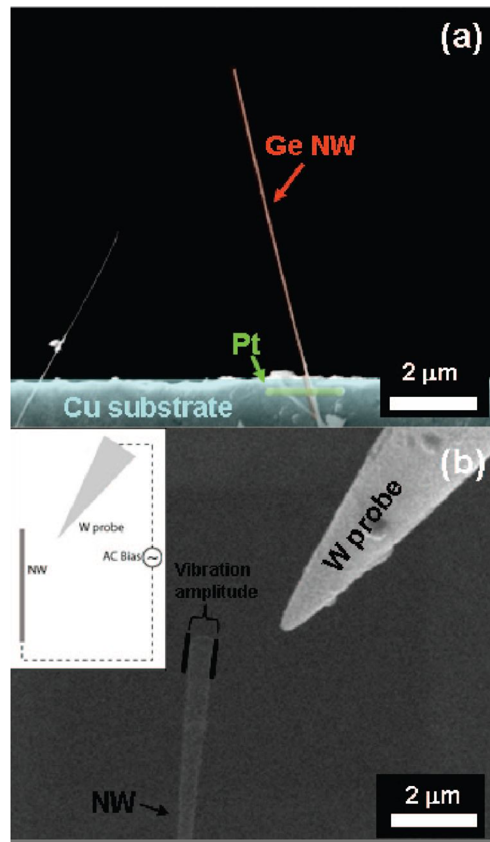

Figure 2.14: a) SEM image of a Ge NW cantilever: the NW is attached to the Cu substrate with Pt deposited by electron beam-induced deposition in the SEM/FIB tool. b) SEM image of a Ge NW vibrating in response to a sinusoidal potential applied by the nearby tungsten probe. (Inset) Device schematic [18]

Poncharal *et al* [19] examined the modulus of elasticity of carbon nanotubes (CNTs). Arc-produced multi-walled CNTs were used. The CNTs formed compact fibers. The fibers had several particularly long protruding CNTs from the tip. One fiber was attached to a Au wire colloidal silver paint [20]. The wire was mounted on an insulated support. The setup was then inserted to a custom-built TEM holder about 5 to 20 μm near the grounded counter electrode. Piezo-driven translation stage was used to position and align the sample. When a voltage was applied protruded NWs became electrically charged and were attracted to the electrode. The micrographs of deformed CNTs can be seen in Figure 2.15. To understand the loading conditions the shape of bent NWs were compared with the shape of tip-loaded and uniformly loaded cantilevers. The comparison led to the conclusion that the loading was entirely on the tip. Therefore, the time dependent forces induced when an alternating voltage

was applied were also entirely on the tip. Sweeping the frequency of the voltage the CNTs were brought to mechanical resonance. All measurements were made in TEM.

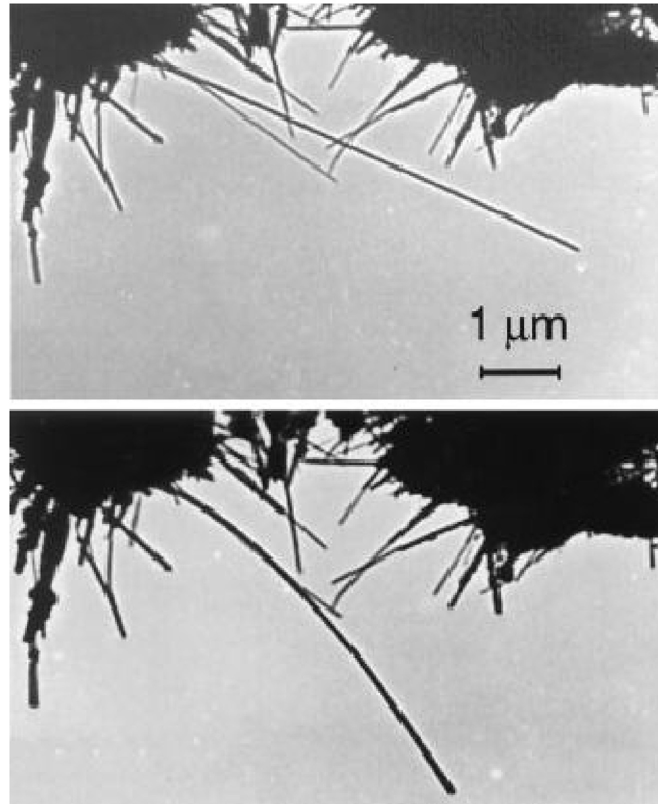

Figure 2.15: Electron micrographs of the electromechanical deflections of a carbon NT
a) Uncharged NT (V_s=0) b) Charged NT (V_s=20 V)
Here an electrical potential difference was applied between the NT
(which was connected to a NT fiber) and a counterelectrode (not shown) [19]

Wang *et al* used the same setup on Si and SiC NWs [21]. The NWs were attached to a Au wire using Ag paste. A mercury droplet or a Au ball was used as the counterelectrode. The sample was directly imaged in TEM. Images recorded from the NW directly gave the morphological and structural information of the NW. The distance between the NW and counter electrode could be adjusted.

Jaroenapibal *et al* [22] used the same setup proposed by Poncharal *et al* [19] to determine the modulus of elasticity of SWCNT bundles. SWCNT bundles were attached by Ag paste to the sample holder and positioned by a micrometer translation stage. Applied Ac voltage was tuned manually until resonance was observed from the micrographs. From the

nonlinear behavior and the low modulus of elasticity that was calculated the interaction between SWCNTs in SWCNT bundles resulted to be very low.

Nam *et al* [23]measured the modulus of elasticity of GaN NWs. However, GaN NWs had triangular cross sections and hence SEM images of the samples were used to calculate the moment of inertia of the NWs. A cluster of NWs were transferred from the growth substrate to a sharpened tungsten tip and attached with Ag paste. The mechanical vibration was induced by applying a 3 to 10 V sine wave frequency sweep between the tungsten tip and the counterelectrode under TEM. Fine tuning was carried out *in-situ* by adjusting the frequency manually based on the images obtained.

Liu *et al* [24]used a similar setup to examine the mechanical properties of WO_3 NWs. The NWs were grown directly on a sharpened tungsten tip. After growth, the tip was loaded to a sample holder in TEM in vacuum of 10^{-7} Torr at room temperature. The tip was driven to approach its Pt counterelectrode by a piezomanipulator. A 1–10 V sine wave signal was applied across the tip and its electrode, and the resonance is stimulated by tuning the applied frequency. However, another DC signal was used to adjust the vibration. The DC signal affects the forcing such that only when the NWs vibrate under the natural frequency, a selected dc voltage can stop the resonance. The diameter, tilt angle, and structure of the NWs were examined through TEM images and energy dispersive spectroscopy.

Belov *et al* [25] on the other hand used base excitation to measure the modulus of elasticity of Si NWs. The NWs were grown on a SOI wafer using chemical vapor deposition (CVD). The NWs were grown along a trench in which they would be allowed to vibrate freely. An interferometric method was adopted to carry out the resonance testing. The Si die was mounted on a piezoelectric element that is contained within a small vacuum chamber pumped down to the 10^{-5} Torr range. The piezoelectric element was actuated by the tracking output of a spectrum analyzer. A He-Ne gas laser beam was directed through a beamsplitter and focused onto the devices to observe the vibration. The substrate was excited and frequency sweep of the cantilevered and bridged NWs were carried out.

Treacy *et al* [26] examined modulus of elasticity of CNTs through the thermal vibrations. The CNT bundles were attached to a TEM observation Ni ring. The samples were examined in TEM at different temperatures. The increase in their vibrational amplitude with temperature suggested the vibrations origin was thermal. Using the equations for vibration modes and vibration energy modulus of elasticity was calculated.

Chen *et al* [27] examined the modulus of elasticity of ZnO NWs. ZnO NWs were grown on a cylindrical substrate and the substrate was fixed to the specimen holder in SEM. Very sharp tungsten probes were used as counter electrodes. The alignment of the NW and the tungsten probes was taken into consideration and the difference in resonance frequencies were measured. The difference was due to forced and parametric vibrations. An extended formula considering the surface effects was used to calculate modulus of elasticity.

2.1.4. Three-point bending

Three-point bending consists of the clamped-clamped NW loaded at its midsection. A representative drawing can be seen in Figure 2.16. The deformation module is known for large and small deflections and the modulus of elasticity can be calculated if the force and displacement is known throughout the process. For small deflections the deflection can be written as:

$$\delta_{beam} = FL^3/(192E_eI) \qquad (2.2)$$

Where δ_{beam} is the deflection, F is the force, E_e is the effective modulus of elasticity and I is the moment of inertia. Hence, the modulus of elasticity can be calculated. The formula gets more complicated as the deflection increases. The forcing could be lateral or vertical. However, the sample must be placed over a trench to reduce the effects of friction and other parasitic results.

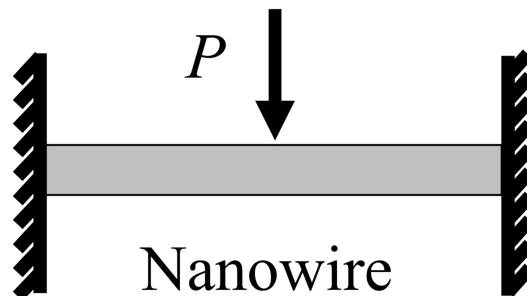

Figure 2.16: Simple configuration of three point bending

Salvetat *et al* [28, 29] devised a method for positioning NWs over trenches. NWs were dispersed in ethanol and then the droplet was laid on porous alumina membrane. After the droplet was dried, some NWs end up over the pores. NWs that were appropriate for three-

point bending testing were found by the AFM images of the substrate. An image of a sample appropriate for testing can be seen in Figure 2.17. The samples diameter, width of the trench and other necessary properties of the sample were obtained from the AFM imaging. The samples were then loaded with the use of an AFM tip and the force-deflection curves were obtained. The adhesive forces were larger than the forces exerted from the AFM tip; hence, no external clamping was considered to be necessary. Salvetat *et al* measured the elastic properties of single [28] and multi-walled [29] CNTs. The same method was used by Lukic *et al* [30] to measure the elastic properties of CNT bundles. Hence the friction between the CNTs and the other deformation effects were taken into account.

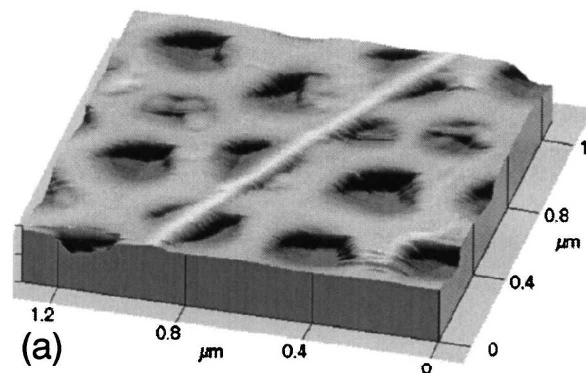

Figure 2.17: a) AFM image of a SWNT rope adhered to the polished alumina ultrafiltration membrane, with a portion bridging a pore of the membrane [28].

Lee *et al* [31] used three-point bending to measure the modulus of elasticity of multi-walled CNTs. Two methods were used to deposit the CNTs. For some CNTs the deposition process was the same used by Salvetat *et al* [29]. Other CNTs were deposited by AC dielectrophoresis over a GaAs wafer with trenches microfabricated intermittently. Gold electrodes were prepared on the substrate by thermal evaporation. While an AC voltage was applied between the two electrodes, a few droplets containing dispersed NTs were placed at the gap and were left to dry. The aim was to minimize the time spent for finding suitable CNTs as most of the NTs were deposited at the electrode boundaries. AFM tips were used to deflect the NTs and the force deflection curve was obtained. The force deflection curve of a flat surface was subtracted from the obtained curve. This way the effect of the stiffness of the substrate could be eliminated. Since the force used to deflect the NT was much smaller then

the adhesive forces, a clamped-clamped configuration was used in calculating the modulus of elasticity.

Sun *et al* [32] examined the modulus of elasticity of polymeric nanofibers. The nanofibers were manufactured by electrospinning. While the electrospinning took place the Si substrate laced with holes was electrically charged and the nanofibers were collected on it. The substrate was scanned for appropriately positioned samples. The adhesive forces were higher than the forces introduced by the AFM tip so that no extra clamping was used.

The NWs could also be dispersed over a previously etched trench. However, the trenches have to be at an appropriate width to prevent drooping of the NWs. Ngo *et al* [33] dispersed Ge NWs in isopropyl alcohol and sonicated them. Then the NWs were micropipetted to the trench and dried. Finally a NW was clamped by electron-beam-induced Pt deposition. The clamping was done as near as possible to the edges of the trench minimize errors. The NWs were then manipulated with an AFM tip laterally and the force displacement curve was obtained.

Wu *et al* [34] examined the modulus of elasticity of hardened Ag NWs. Similar to Ngo *et al* the NWs were dispersed, positioned over trenches and fixed by electron-beam-induced Pt deposition. AFM tips were used to deform the NWs until fracture so that the yield point and fracture stress could be examined. The same method was used by Heidelberg *et al* [35] on Si NWs and Au NWs. However, the large deflections obtained forced them to use an extended formula of the deflection.

Using the same testing methods Xiong *et al* [36] measured the modulus of elasticity of ZnS NWs. However, Xiong *et al* preferred etching the trench under clamped sample.

2.1.5. Static Bending Test

Similar to the three-point bending test, the static bending test consists of bending a nanoentity. However, the specimen used is not in clamped-clamped figuration but in clamped free figuration. A simple figure of the testing configuration can be seen in Figure 2.18.

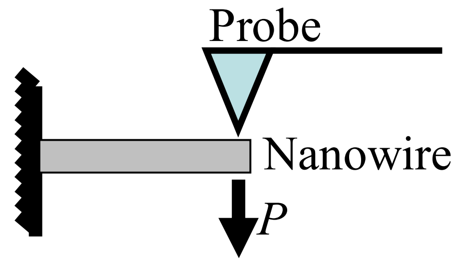

Figure 2.18: Simple configuration of static bending test

The deformation module is also well known. For small displacements the displacement can be written as:

$$\delta_{beam} = Fl^3/(3EI) \quad (2.3)$$

Where δ_{beam} is the deflection, F is the force, l is the length, E is the modulus of elasticity and I is the moment of inertia. Modulus of elasticity can be calculated from the force-displacement graph of the sample. AFM tips are used as force actuators and force and displacement sensors. Also SEM micrographs can be used to measure displacement and observe the deformation (see Manoharan *et al* [37], Hoffmann *et al* [2, 38]). Positioning of the NWs is a challenge. Usually the process used to manufacture NWs result with samples that are clamped on one end to the substrate and free on the other end as reported by Hoffmann et al [2], Gordon *et al* [39] and Hoffmann *et al* [38]. The NWs can also be manufactured by etching the substrate as reported by Nilsson *et al* [40]. This simplifies the clamping issue. The NWs could also be dispersed in a liquid droplet and evaporated on the desired position and fixed by EBID as done by Manoharan *et al* [37]. Wong *et al* [41] preferred to disperse the NWs randomly on the substrate and attach them to contact pads and choose appropriately positioned NWs as specimens. Although the system is simple, the friction among other effects should be taken in account. Moreover, the measurement of the length of the sample is also problematic in static bending test. The end point of the substrate and starting point of the sample is hard to measure.

2.2. Size Dependency of Properties of Nanowires

The many tests that have been conducted on NWs and NTs agreed on several aspects. As the size decreases the surface defects and intrinsic dislocations are encountered less. This reduction increases the strength and allows higher elasticity regardless of their material.

However, modulus of elasticity is a different issue. As modulus of elasticity is mainly dependent on the atomic bonding of the material, it is expected that no alteration is observed in the elastic response as long as the crystallography is the same. This assumption agrees with the results of several researches such as [18, 25, 33, 35]. However, generally results suggested that modulus of elasticity of NWs are either significantly lower than bulk values [6, 7, 36-38] or larger [34]. This difference could be explained as the change of materials crystal structure as a result of the manufacturing process. Moreover some articles argue that as the diameter crosses a critical value the modulus of elasticity becomes diameter-dependent and decreases [23, 40, 42] or increases [11, 24, 30-32, 39] while some articles observe no size dependency [18, 25, 34, 37]. Table 2.1 shows the results presented.

Test Type	Sample Material	Sample Diameter	Force Degree	Integration Techniques	Scale Dependence	Comparison with Bulk	Ref
Uniaxial Tensile Test	Si	d=6nm	F=10nN	Grown between AFM and substrate	Not mentioned	Very low	[6]
Uniaxial Tensile Test	ZnO	d=200-500nm	F=100μN	Clamped by Pt deposition	Not mentioned	Significantly lower	[7]
Uniaxial Tensile Test	ZnO	d=20-400nm	F=100μN	Clamped by Pt deposition	Increases as diameter decreases	Same as bulk for large NWs	[11]
Uniaxial Tensile Test	Pd	d=200nm	F=100nN	Clamped by Pt deposition	Decrease as diameter decreases	Significantly lower	[9]
Uniaxial Tensile Test	ZnO	d=60-130nm	Not mentioned	Grown on substrate clamped by C deposition	Not mentioned	Lower	[2]
Resonance-based	SiC,Si02	d=40-190nm	Not mentioned	Bundle of nanowires, clamped sample holder	Not mentioned	Lower	[21]

Test Type	Sample Material	Sample Diameter	Force Degree	Integration Techniques	Scale Dependence	Comparison with Bulk	Ref
Resonance-based	Ge	d=50-140nm	Not mentioned	Clamped by Pt deposition	Not diameter dependent	Near bulk	[18]
Resonance-based	Si	d=40-400nm	Not mentioned	Grown on wafer	Not diameter dependent	Near bulk	[25]
Resonance-based	MWCNT	d=8-40nm	Not mentioned	Bundle of nanowires, clamped sample holder	A sharp decrease explained in a new defm buckle	Not mentioned	[19]
Resonance-based	GaN	d=36-84nm	Not mentioned	Affixed to W tip with Ag Paste	Decrease as diameter decreases	Same as bulk for large NWs	[23]
Resonance-based	WO3	d=16-53nm	Not mentioned	Grown on tip	Increases as diameter decreases	Same as bulk for large NWs	[24]
Resonance-based	ZnO	d=17-550nm	Not mentioned	Grown on substrate substrate clamped	Increases as diameter decreases	Same as bulk for large NWs	[27]
3 point bending	Au, Si	d=115(Au)-(100-200)(Si)nm	F=10μN	Clamped by Pt deposition	Not mentioned	Same as bulk for large NWs	[35]
3 point bending	MWCNT	d=10-25nm	F=10nN	Deposited over holes and trenches	Increases as diameter decreases	Near bulk	[31]

Test Type	Sample Material	Sample Diameter	Force Degree	Integration Techniques	Scale Dependence	Comparison with Bulk	Ref
3 point bending	MWCNT	d=1-16nm	F=10nN	Deposited over holes and trenches	Increases as diameter decreases	Not mentioned	[30]
3 point bending	Ge	d=20-80nm	F=10mN	Clamped by Pt deposition	Not mentioned	Near bulk	[33]
3 point bending	ZnS	d=40-190nm	F=10nN	Trench etched underneath specimens	Not mentioned	Lower	[36]
3 point bending	Polymeric NF	d=100-2500nm	Not mentioned	Deposited over holes and trenches	Increases as diameter decreases	Same as bulk for large NWs	[32]
3 point bending	Ag	d=22-35nm	F=100nN	Clamped by Pt deposition	Not diameter dependent	Higher	[34]
Static bending	Cr	Cantilever	F=10nN	Grown and tested on substrate	Decrease as diameter decreases	Lower	[40]
Static bending	Si	d=100-700nm	F=100nN	Grown and tested on substrate	Increases as diameter decreases	Near bulk	[39]
Static bending	ZnO	d=200-750nm	Not mentioned	Grown and tested on substrate	Not diameter dependent	Lower	[37]

Table 2.1: Comparison of modulus of elasticity of NWs and bulk

Several theories were suggested considering the size dependency. One speculation is that as the atomic bonding remains the same and the dislocations decrease as transition is made from bulk to nanoscale the modulus of elasticity should remain the same or increase. However, due to the increasing effect of surface forces if the atomic bonding is comparable to the interactions of the neighboring atoms the modulus of elasticity could decrease as the diameter of the NW decrease [7].

2.3. Intrinsic Sample Properties Affecting Test Results

The major objective of aforementioned experiments was to measure the size dependency of the materials modulus of elasticity and observe the deformation models and defect densities of NWs. However, the calculated modulus of elasticity can be affected by the intrinsic properties of the material. These properties and their effects on the calculations should be taken into account to ensure reliable results. The most important properties of concern can be listed as:

- Intrinsic stress
- Crystalline orientation
- Oxide thickness

Alongside the stress strain curve these values should also be measured and their effects should be used in any modeling effort.

2.3.1. Intrinsic stress

Intrinsic stress is the stress already accumulated in the sample or device before the testing has started. Intrinsic stress reflects to the internal structure of the thin film of

interest and can be compressive or tensile. The main reason of intrinsic stress in the device layer of an SOI wafer is the manufacturing process. The lapping process is done under high temperature and as the wafer is cooled intrinsic stress emerges. Moreover processes done to the wafer also build intrinsic stress. Intrinsic stress build in the chip will cause deformation of thin members when released. This deformation is the main element of measuring the intrinsic stress. The deflection of a pre-known geometry can be used to calculate the intrinsic stress. The most common geometries used are discs and beams. For example, Baek *et al* [43] used beam structures to measure the average intrinsic stress and stress gradient. Clamped-clamped and clamped-free beam structures were fabricated using UV-LIGA surface micromachining and dry release methods. Clamped-free and clamped-clamped beams were electrostatically excited to resonance. The resonance frequency was measured optically with the setup seen in Figure 2.19. As modulus of elasticity differs from the bulk values as the system is miniaturized it was measured from the data acquired from the clamped-free beams. Intrinsic stress affects the resonance frequency of structures. Thus the difference was used to calculate the average intrinsic stress. Stress gradient inside the thin film causes bending inside the film thus causing vertical deflections. The gradient was measured from the end tip deflection of the clamped-free beams. The vertical deflection was measured with a laser surface profiler.

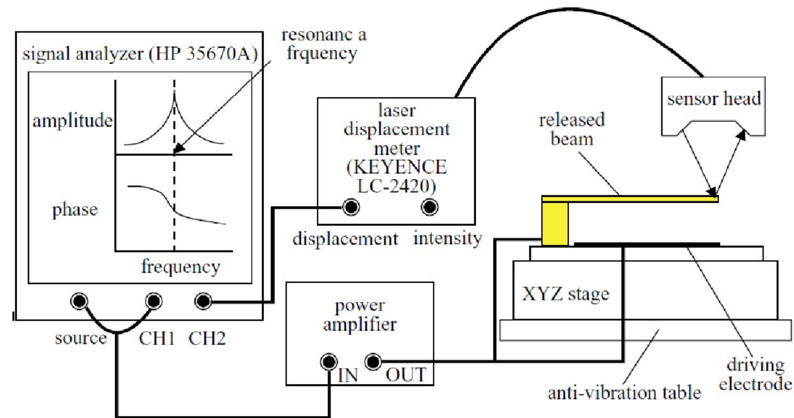

Figure 2.19: Measurement setup for the detection
of the resonance frequency of a microbeam [43]

More compact methods have also been used to determine the intrinsic stress. Lin *et al* [44] and Ericson *et al* [45] used amplifiers to measure the intrinsic stress. The devices consisted of one fixed beam and a released beam. The released beam would cause a rotation and the rotation would be amplified through a rigid beam. Vernier gauges between the released and fixed beams provided quick optical readout for the user. The structures can be seen in Figure 2.20 and Figure 2.21. Ericson *et al* also supplied long free standing beams for stress gradient measurement.

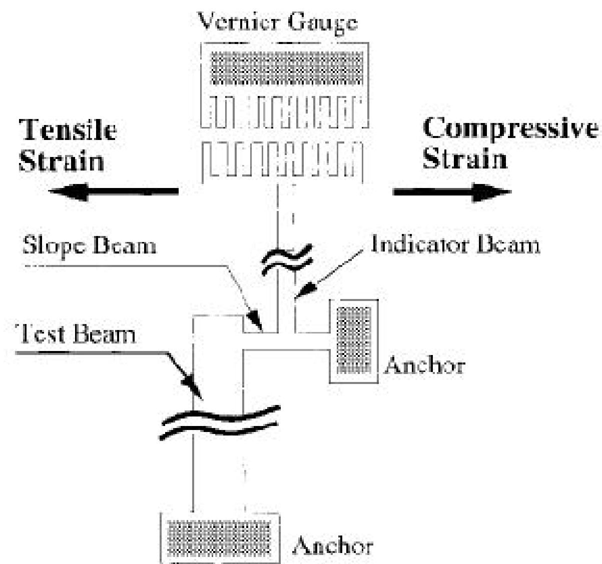

Figure 2.20: A sketch of intrinsic stress gauge designed by Lin *et al* [44]

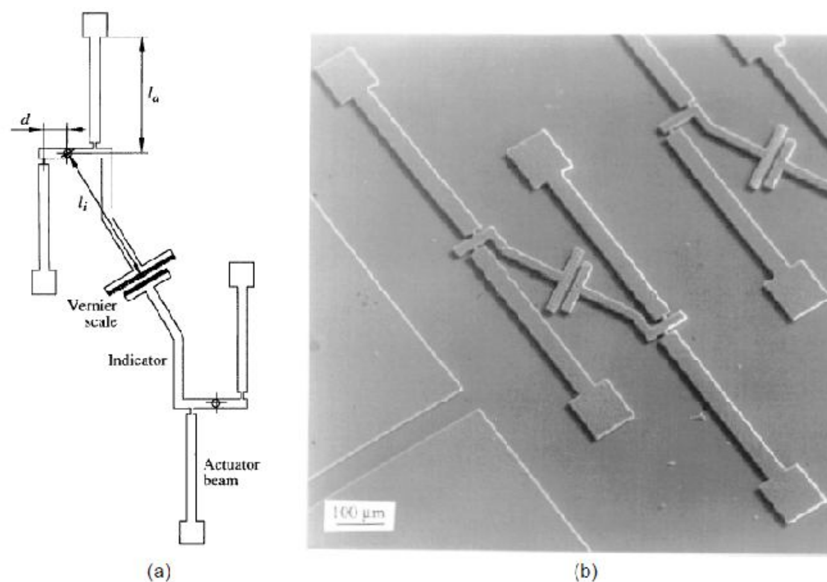

Figure 2.21: a) A sketch and b) an SEM micrograph of the intrinsic stress gauge designed by Ericson *et al* [45]

Fan *et al* [46] used micromachined spirals as stress gradient gauges. The spiral geometry amplifies the vertical deflection and thus the evaluation of the stress gradient is quicken and simplified. The spiral would extend upward if there was a positive stress gradient and downward if there was a negative stress gradient. By anchoring spirals from their spiral center or at their end both positive and negative stress gradients could be observed. Li *et al* [47] extended this method by calculating the average intrinsic stress from the lateral size difference. Thus micro spirals could be used as a measurement device for intrinsic stress and stress gradient. A schematic for a released spiral can be seen in Figure 2.22.

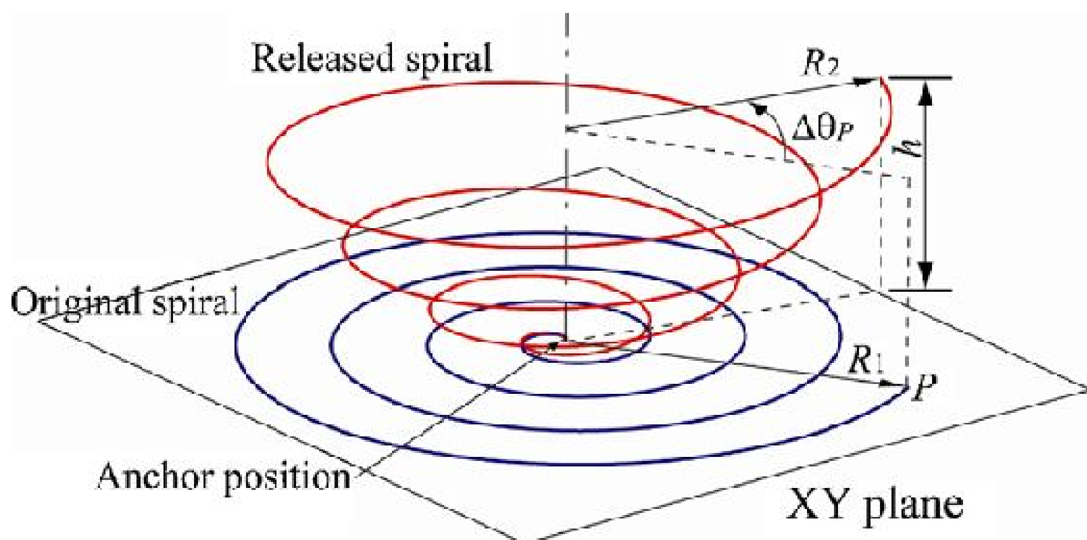

Figure 2.22: Schematic of released spiral and deformation parameters: rotation angle $\Delta\theta p$, change of the lateral size $\Delta R = R2 - R1$, and structure height h at the free end point P.[47]

2.3.2. Crystalline Orientation

Si is an anisotropic material. Hence the properties, especially modulus of elasticity, of Si depend on orientation. Therefore the crystalline orientation should be considered and determined before the testing. The wafers are cut on one side to indicate the crystalline orientation. The cut often parallels the (111) direction. However, the precision is about ± 1˚. To increase the precision alignment targets are needed. The general method is to use a test pattern of closely spaced lines, a wagon wheel, to determine the orientation as used by Seidel *et al* [48]. As the Si wafer undergoes anisotropic etching undercut occurs depending on the orientation. The etchant develops a blossom-like pattern as in Figure 2.23. Minima and maxima state crystalline orientation lines where the absolute minimum states the (111) direction. The mask can then be aligned considering the orientation.

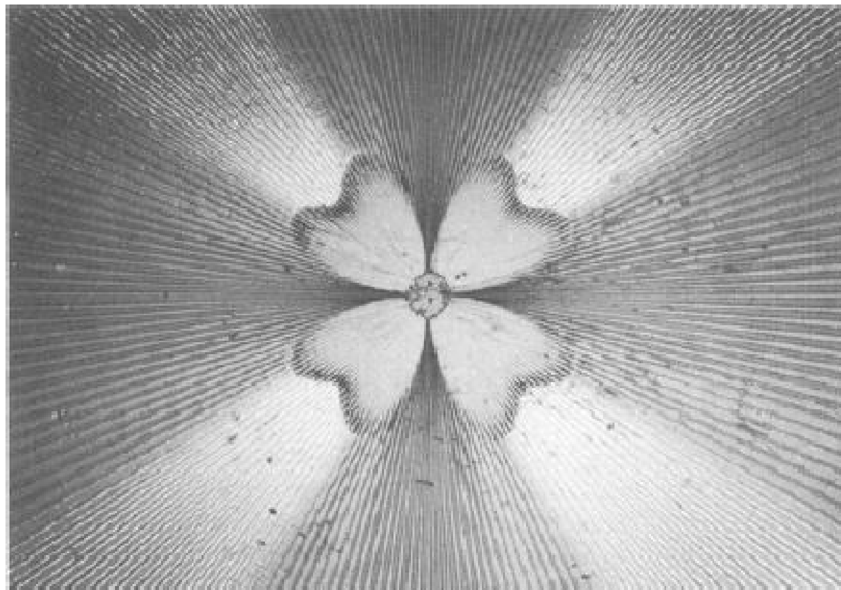

Figure 2.23: Etch pattern emerging on a wagon wheel mask on a <100> wafer [48]

2.3.3. Oxide Thickness

As a system scales down to nanometer scales the surface effect starts to dominate. Therefore the surface of a NW should be considered in mechanical testing. The surface of a Si NW has a native oxide film which is approximately 2 nm thick. Other than the mechanical effects this native oxide layer can have surface effects that alter the data. The native oxide thickness can be measured by cutting a NW by FIB and examining it in SEM. However, generally the native oxide effect is assumed to be negligible.

Chapter 3

MICROTENSILE TESTING DEVICE

MEMS devices are generally preferred on conducting uniaxial tensile testing of NWs. Although such devices increase the complexity of fabrication, they facilitate the handling and read-out of the experiment. A general limitation is the dependence on microscopic imaging on determining the load on the sample and the integration of the sample on the device. Certain designs were carried out to overcome the imaging limitation [7, 8, 10-13, 37, 42, 49]. In such designs electronic load sensors were introduced to the design. However, samples are still integrated to the device by FIB Pt deposition. To overcome this issue the sample should be fabricated on the device.

Design of such a MEMS device includes design of the physical system, layout and fabrication process. Design of the physical system of the device is the foundation step of the design process. Hence, has crucial importance on functionality of the device.

Finite element analysis (FEA) enables simulation of the physical system at hand. Simulation of the device as a design step applies as a scrutiny of the system and eliminates subsequent repeated fabrication trials.

In this chapter design procedures of a microtensile testing device is explained in detail. Afterwards, FEA of the device is described and results are presented.

3.1. Model of the Microtensile Device

Considering precedent microtensile devices different actuation and readout methods were investigated. In conclusion a model similar to the device designed by Zhang *et al* [12] is chosen. The microtensile device comprises of three main components as seen in Figure 3.1. These components are the actuator, load sensor and the sample that is to be tested. The device including the sample is composed of Si. The actuator is an electrostatic comb drive that provides the force to deform the sample. As the device is under quasi-static equilibrium the load sensor is used to measure the deformation and hence the load on the sample. The load sensor is chosen to be a differential capacitive sensor in tri-plate geometry.

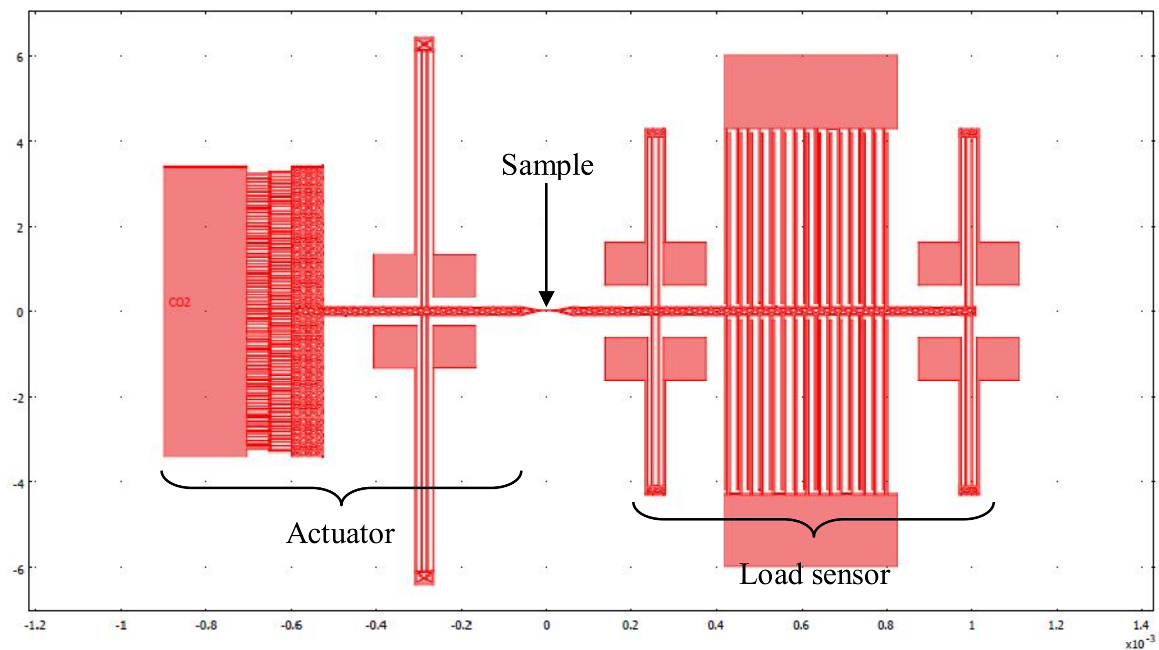

Figure 3.1: Top view of the microtensile testing device. All units are in meters.

The device operates electrically. As a DC voltage difference is applied to the actuator, an electrostatic force is applied to the system and the displacement of the load sensor side is measured by the applied AC voltage to the fixed electrodes of the load sensor. The test is conducted until the sample fractures. Following the fracture a frequency sweep is conducted on the load sensor and the actuator side to measure the spring constants.

The device can be modeled as a spring mass system as seen in Figure 3.2. In the mathematical model F_{es} is the electrostatic force, U_{ac} is the actuator displacement, U_{ls} is the load sensor displacement, k_{ac} is the actuator spring constant, k_{ls} is the load sensor spring constant, and k_s is the sample spring constant.

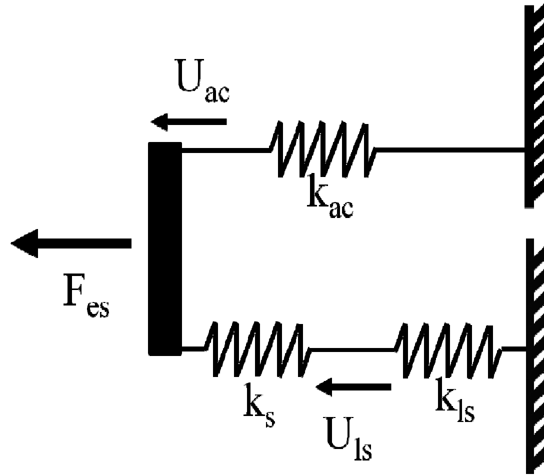

Figure 3.2: Spring mass model of the microtensile testing device.

The stress strain curve of the sample is obtained by the following equations.

$$\sigma = \frac{F_s}{A_s} = \frac{F_{ls}}{A_s} = \frac{k_{ls}U_{ls}}{A_s} \tag{3.1}$$

$$\varepsilon = \frac{\Delta U_s}{l_s} = \frac{U_{ac}-U_{ls}}{l_s} = \frac{\frac{F_{ac}}{k_{ac}}-U_{ls}}{l_s} = \frac{\frac{F_{es}-F_{ls}}{k_{ac}}-U_{ls}}{l_s} = \frac{F_{es}-k_{ls}U_{ls}-k_{ac}U_{ls}}{k_{ac}l_s} \quad (3.2)$$

Where, A_s is the cross-section area of the sample, F_s is the force on the sample, F_{ls} is the force on the load sensor, F_{ac} is the force on the actuator springs, l_s is the length of the sample and ΔU_s is the difference in length of the sample. To calculate the strain, F_{es} is needed to be calculated. F_{es} is a function of the voltage difference on the actuator denoted by V and U_{ac} such that $F_{es} = F_{es}(U_{ac}, V)$. Taking into account that:

$$U_{ac} = \frac{F_{es} - k_{ls}U_{ls}}{k_{ac}} \quad (3.3)$$

F_{es} can be calculated from V and U_{ls}. Hence the stress and strain of the sample can be directly calculated from the voltage on the actuator and the output of the load sensor.

3.2. Actuator of the Microtensile Device

As stated, the model of the actuator is electrostatic comb drive. Electrostatic comb drives are commonly used as actuators for MEMS devices as they require low power, supply high precision and are easily fabricated. Beside these advantages, the comb drive actuators have some disadvantages as well. The main disadvantage is that the limited force output of the comb drive actuators.

The electrostatic comb drive consists of interdigitated fixed and movable fingers. Actuation is based on the electrostatic force between the fixed and movable comb structures. By applying electrical voltage difference, an electrostatic force is generated between fixed and movable fingers that pull the shuttle along the moving axis which creates a tensile force on the specimen. A schematic of a single finger can be seen in Figure 3.3.

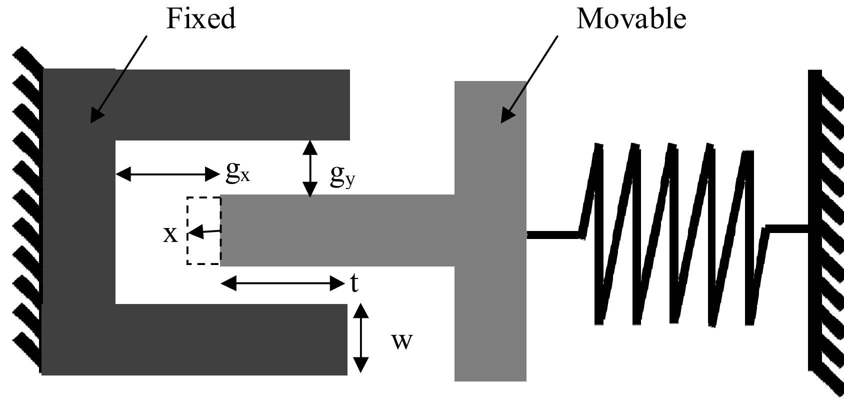

Figure 3.3: Schematic illustration of close-up view of a single pair of interdigitated comb fingers.

As seen in the above schematic, w is width of each comb finger, t is the zero voltage overlap length between the fingers, g_x and g_y are gap distances in x- and y-directions respectively, and x is the displacement in x-direction. Expression of the resulting electrostatic force can be obtained by the derivation and simplification of the energy formula.

$$F_{es} = -\frac{dW_{es}}{dx} = -\frac{d(C_{total}V^2/2)}{dx} = -\frac{d}{dx}\left[N_{ac}\varepsilon_0 h\left(\frac{w}{g_x - x} + \frac{t+x}{g_y}\right)V^2\right] \quad (3.4)$$

$$F_{es} = -N_{ac}\varepsilon_0 h\left(\frac{w}{(g_x - x)^2} + \frac{1}{g_y}\right)V^2 \quad (3.5)$$

In the above expression, W_{es} is the electrostatic work, C_{total} is the total capacitance, h is height of the actuator device, N_{ac} is the number of fingers of the comb drive, ε_0 is the permittivity of the free space, $\varepsilon_0 = 8.854 \times 10^{-12}\ F/m$ since relative permittivity of air is equal to 1.

3.3. Load Sensor of the Microtensile Device

The load sensor is the direct source of the measurements of the tensile test. A differential capacitive sensor with tri-plate geometry is utilized in the proposed geometry as stated. The tri-plate geometry consists of interdigited movable fingers between two fixed fingers as seen in Figure 3.4. The displacement induced by the actuator causes a displacement on the load sensor which results in a capacitive difference between the movable fingers and the two fixed fingers.

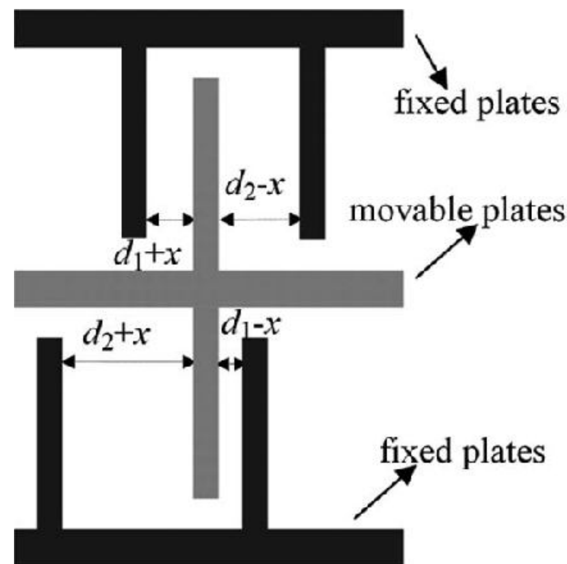

Figure 3.4: Schematic illustration of close-up view of a single pair of interdigitated comb fingers of load sensor [12].

As seen in the above schematic, w is width of each comb finger, l is the length of the fingers, d_1 and d_2 are the initial gap distances between movable and fixed fingers, and x is the displacement in x-direction.

Denoting the height of the load sensor as h, the number of finger sets as seen in Figure 3.4 as N_{ls}, the capacitive difference induced in the load sensor as ΔC and assuming small displacement such that $x \ll d_1$ and $x \ll d_2$ the capacitive difference induced on the load sensor can be written as:

$$\Delta C = 2N_{ls}\varepsilon_0 hl\left(\frac{1}{d_1^2-x^2}-\frac{1}{d_2^2-x^2}\right)x \tag{3.6}$$

By applying two AC voltages with 180º phase difference to the fixed fingers the capacitance difference can be transformed to an AC signal. The voltage of the AC signal can be written as:

$$V_{out} = aV_e\Delta C = 2aN_{ls}\varepsilon_0 hlV_e\left(\frac{1}{d_1^2-x^2}-\frac{1}{d_2^2-x^2}\right)x \tag{3.7}$$

In the equation above, V_{out} denotes the voltage obtained by the load sensor, V_e denotes the voltage applied on the fixed fingers and a denotes a constant that depends on interface dynamics.

3.4. Design Criteria

Certain criteria are taken into account in the design process. The main criteria are the force and displacement demand for the fracture of the sample, simplicity and stability of the actuator and the load sensor and nonlinearity of the measurements.

3.4.1 Force and Displacement Demand of the Device

The force demand of the device is directly related to the sample size. As the sample size increases force needed for fracture increases resulting as alteration in the geometry in the actuator. Literature suggests that as the SiNW radius decreases the modulus of elasticity

of the sample decreases. However, a safe assumption in designing the device is that the modulus of elasticity of the SiNW is the same as the bulk modulus of Si. As the fracture displacement is directly proportional to the length of the SiNW, displacement demand is directly related to the length of the SiNW. Literature suggests a fracture strain of 6% a reasonable estimation. However, a safe assumption of 10% is used during the design.

3.4.2 Simplicity of the Device

Number of fingers of the actuator and load sensor increases the complexity of the device. Complexity of the device increases the possibility of manufacture errors, hence malfunctioning devices. Therefore the optimum design obtains minimum sets of fingers.

3.4.3 Stability of the Device

Due to electrostatic actuation and detection stability arises as an issue. Electrostatic force increases proportional to the inverse square of the increasing gap distance, where mechanical restoring force increases linearly. Hence, at a certain point of displacement and voltage difference attraction force becomes higher than the restoring force and failure occurs. The name of this failure is pull-in. Both the actuator and the load sensor are prone to this failure. The maximum displacement the actuator and load sensor can sweep is determined by the pull-in displacement.

To determine the point of instability, net force and the derivative of the net force must be zero as seen in Equations 3.8 and 3.9.

$$F_{net} = F_{es} + F_{mech} = 0 \tag{3.8}$$

$$\frac{dF_{net}}{dx} = \frac{dF_{es}}{dx} + \frac{dF_{mech}}{dx} = 0 \tag{3.9}$$

Where F_{net} denotes the net force, F_{es} denoted the electrostatic force and F_{mech} denotes the restoring force or in other words the mechanical force on the element.

The stability analysis for the actuator is relatively simple. For the electrostatic comb drive, F_{es} and F_{mech} can be written as seen in Equations 3.10 and 3.11.

$$F_{es} = -N_{ac}\varepsilon_0 h\left(\frac{w}{(g_x - x)^2} + \frac{1}{g_y}\right)V^2 \tag{3.10}$$

$$F_{mech} = k_{eq}x = \frac{k_{ac}(k_s + k_{ls})}{k_{ac} + k_s + k_{ls}}x \tag{3.11}$$

Voltage and displacement values in which pull-in occur can be obtained by inserting these components into Equations 3.8 and 3.9.

However, stability analysis of the load sensor is somewhat more complicated. The F_{es} is affiliated to the voltage on the fixed fingers and is more complicated due to the tri-plate geometry. For the load sensor, F_{es} and F_{mech} can be written as seen in Equations 3.12 and 3.13.

$$F_{es} = 2N_{ls}\varepsilon_0 hlV_e{}^2 x\left(\frac{d_1}{(d_1^2 - x^2)^2} + \frac{d_2}{(d_2^2 - x^2)^2}\right) \tag{3.12}$$

$$F_{mech} = k_{ls}x \tag{3.13}$$

Therefore a different approach is taken to obtain the voltage and displacement values in which pull-in occurs. Therefore some variables were assumed. δ is the ratio between electrostatic force and the restoring force, $F_t = ma$ is the external force, b is the ratio between d_2 and d_1 and $\tilde{x}$ is the ratio between x and d_1. Considering the new variables, the variable δ and the systems equation of motion could be reduced to Equations 3.14 and 3.15.

$$\delta = \frac{2V_e{}^2 N_{ls}\varepsilon_0 A}{k_{ls}d_1{}^3} \tag{3.14}$$

$$\frac{F_t}{k_{ls}d_1} = \tilde{x}\left(1 - \delta\left[\frac{1}{b^3\left(1-\frac{\tilde{x}^2}{b^2}\right)^2} + \frac{1}{(1-\tilde{x}^2)^2}\right]\right) \tag{3.15}$$

The displacement in which the pull-in occurs can be obtained by graphing the $\frac{F_t}{k_{ls}d_1}$ vs $\tilde{x}$. As seen in Figure 3.5 the curve has a single maxima. The pull-in instability occurs at this maxima point.

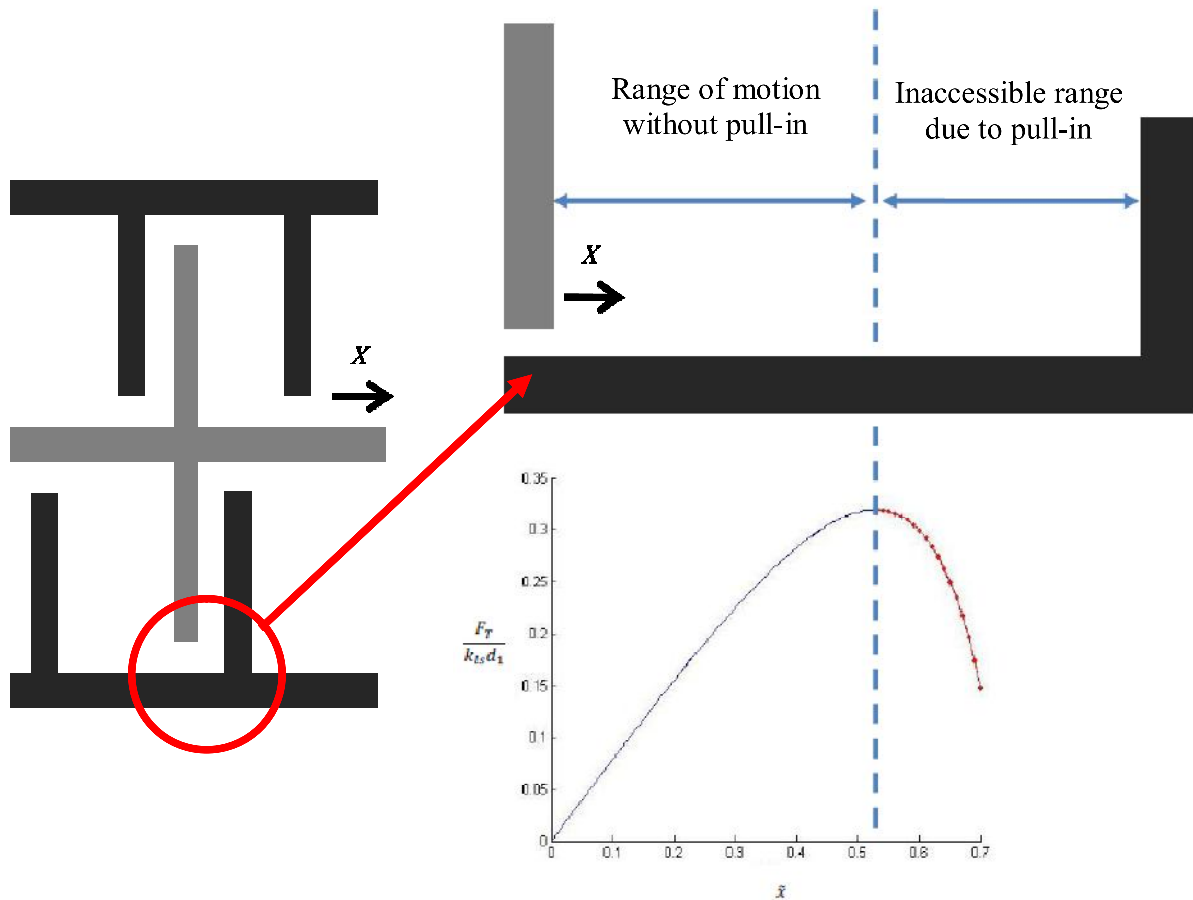

Figure 3.5: Graphical solution of a tri-plate load sensor. The area in red is the area subsequent pull-in instability.

3.4.4 Nonlinearity of Measurements

To simplify measurements linear output from the sensor is desired. However, due to the tri-plate geometry and the electrostatic forces, the output of the load sensor is always nonlinear. Using terminal linearity definition in which nonlinearity is defined as the deflection from a hypothetical curve connecting the end points of the curve, a value of nonlinearity can be calculated. Nonlinearity due to the tri-plate geometry of the load sensor can be calculated from the Equation 3.16.

$$NL_d(\tilde{x}) = \frac{\tilde{x}}{\tilde{x}_m}\left[\frac{\left(\frac{1}{1-\tilde{x}^2}-\frac{1}{b^2-\tilde{x}^2}\right)}{\left(\frac{1}{1-\tilde{x}_m{}^2}-\frac{1}{b^2-\tilde{x}_m{}^2}\right)} - 1\right] \quad (3.16)$$

Where $\tilde{x}_m$ denotes the maximum displacement of the movable finger of the load sensor and $NL_d(\tilde{x})$ denotes the nonlinearity due to displacement.

However, voltage applied to the fixed fingers introduces additional force, causing spring softening. As a result the effective spring constant decreased and can be obtained from the Equation 3.17.

$$k_{eff} = k_{ls} - 2V_e{}^2 N_{ls}\varepsilon_0 A\left(\frac{d_1}{(d_1{}^2-x^2)^2} - \frac{d_2}{(d_2{}^2-x^2)^2}\right) \quad (3.17)$$

Where k_{eff} denotes the effective spring constant of the load sensor.

Taking the spring softening effect into account the observed nonlinearity of the load sensor can be obtained. The value of the force measurement nonlinearity, denoted as $NL_F(\tilde{x})$, can be calculated as seen in Equation 3.18.

$$NL_F(\tilde{x}) = \frac{\tilde{x}}{\tilde{x}_m}\left\{\frac{\left(\frac{1}{1-\tilde{x}^2}-\frac{1}{b^2-\tilde{x}^2}\right)}{\left(\frac{1}{1-\tilde{x}_m{}^2}-\frac{1}{b^2-\tilde{x}_m{}^2}\right)} - \frac{\left[1-\delta\left(\frac{b}{(b^2-\tilde{x}^2)^2}+\frac{1}{(b^2-\tilde{x}^2)^2}\right)\right]}{\left[1-\delta\left(\frac{b}{\left(b^2-\tilde{x}_m{}^2\right)^2}+\frac{1}{\left(b^2-\tilde{x}_m{}^2\right)^2}\right)\right]}\right\} \quad (3.18)$$

3.4.5 Parametric Analysis

A MATLAB™ code is written to observe the effects of certain variables on the stability and the nonlinearity of the device. The code can be obtained in Appendix A. For the load sensor stability and nonlinearity analysis, the variables d_1, b, V_e and $\tilde{x}_m$ is swept while other variables were kept constant. The total capacitance difference that is induced on the load sensor, the capacitance diversion from linearity, stability analysis and nonlinearity due to displacement and electrostatic force and number of needed finger set graphs are drawn for each sweep. Whereas, for the actuator the variables g_x and g_y are swept while keeping the other variables constant. Pull-in displacement and number of needed actuator finger graphs are obtained for each sweep.

3.4.5.1 Load Sensor Parametric Analysis

The analysis is conducted for a device with a SiNW of 75 nm and $d_1 = 3\ \mu m$, $b = 5$, $V_e = 2.5\ V$ and $\tilde{x}_m = 0.5$ when kept constant. Parametric analysis reveals that the total induced capacitance difference is not dependent to d_1 and V_e while increasing b decreases the induced capacitance difference slightly and increasing $\tilde{x}_m$ increases the induced capacitive difference as seen in Figure 3.6.

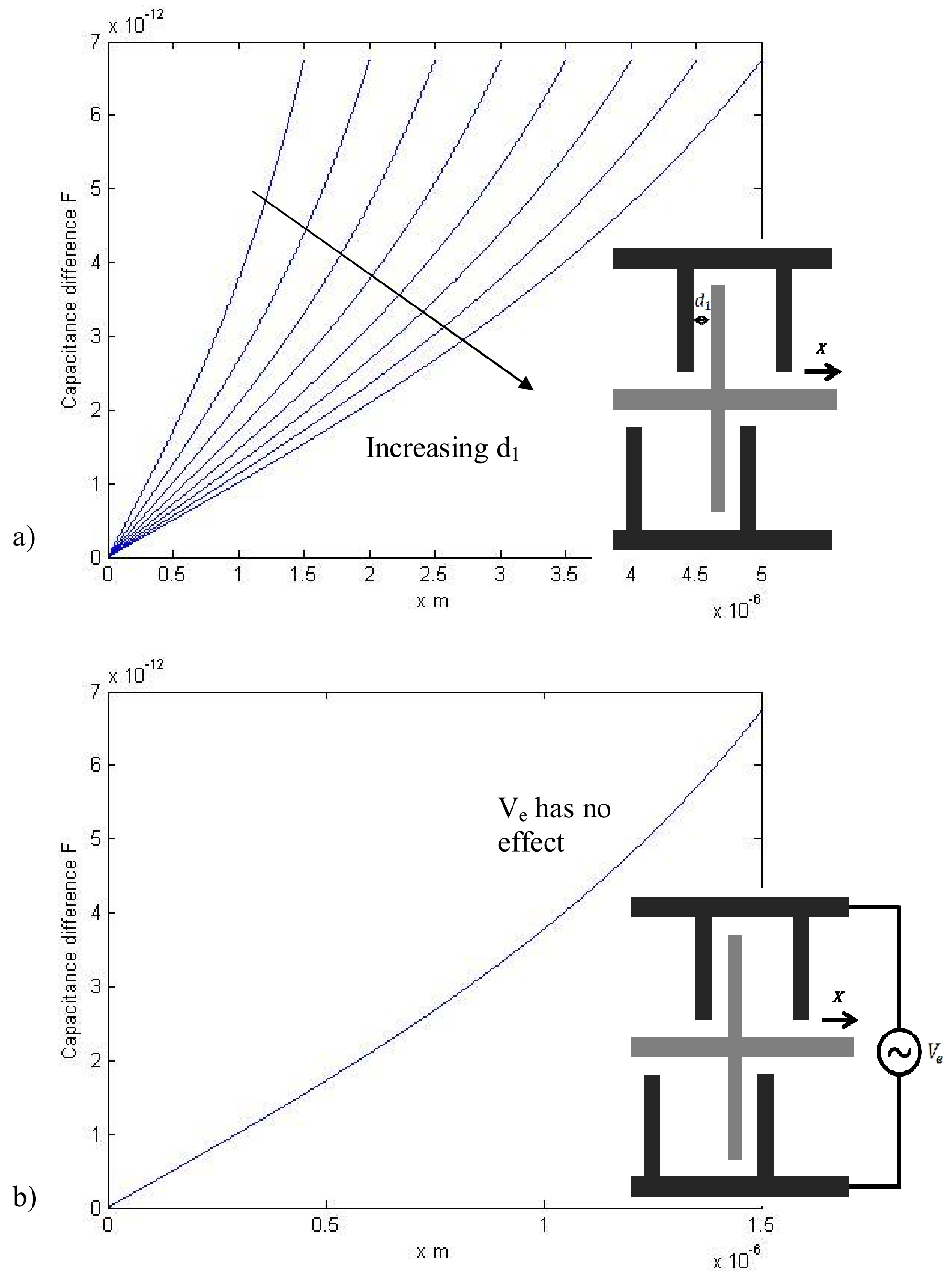
a)
x 10^-12
Capacitance difference F
x m
x 10^-6
Increasing d1
d1
x
b)
x 10^-12
Capacitance difference F
x m
x 10^-6
Ve has no effect
x
Ve

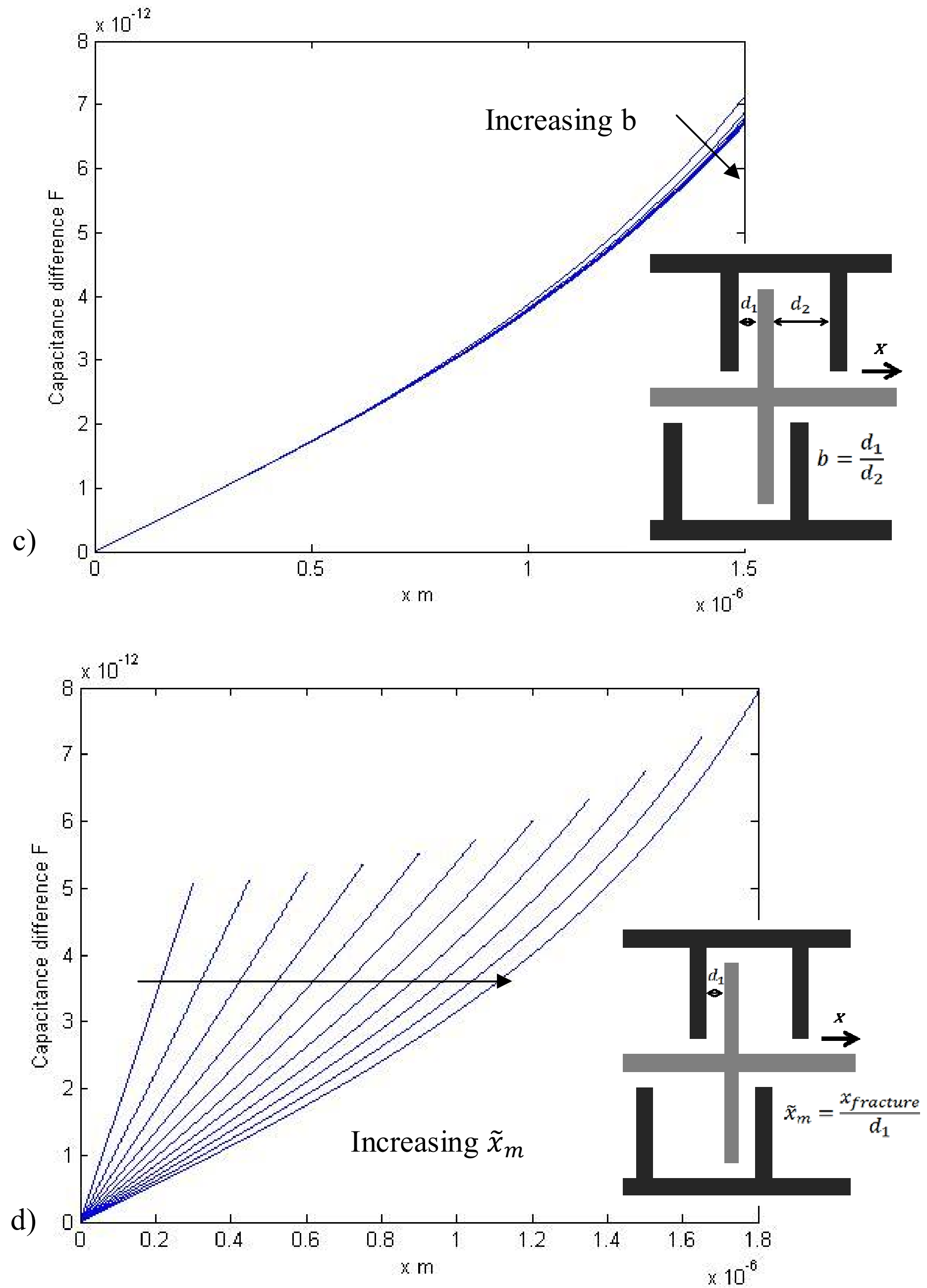

Figure 3.6: Effects of a) d_1, b) V_e, c) b and d) $\tilde{x}_m$ on the total induced capacitance difference of the load sensor.

Another parametric analysis reveals that the nonlinearity due to displacement is not dependent to d_1 and V_e. Whereas nonlinearity due to electrostatic force decreased as d_1 increased and increased greatly as V_e increased. It also reveals that increasing b decreases the nonlinearity due to displacement and electrostatic force greatly while $b < 5$ but has little effect while $b > 5$ and increasing $\tilde{x}_m$ increases the nonlinearity due to displacement and electrostatic force as seen in Figure 3.7.

a)
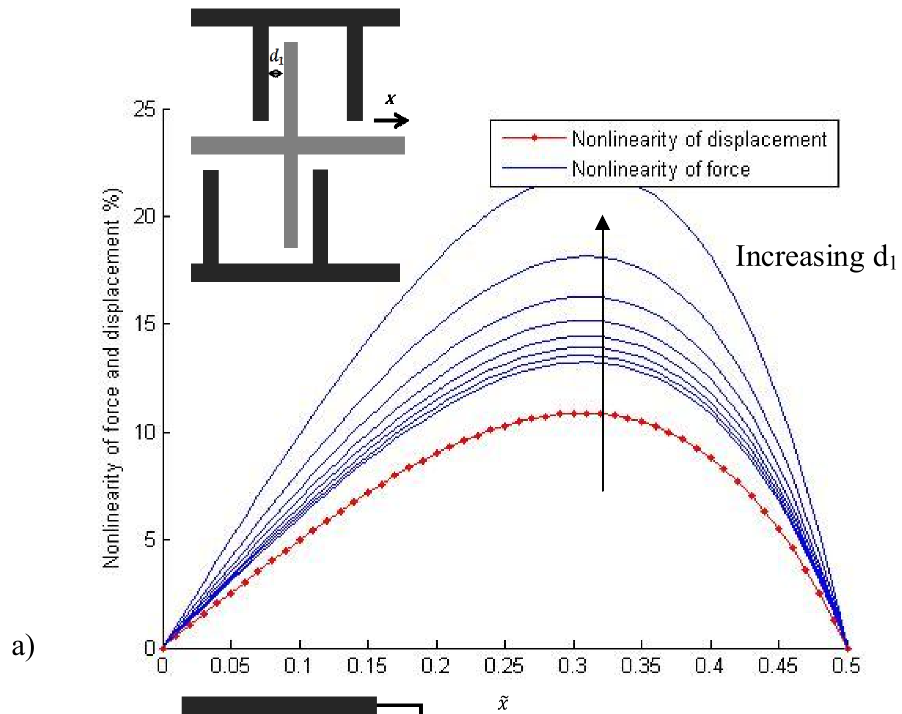

b)
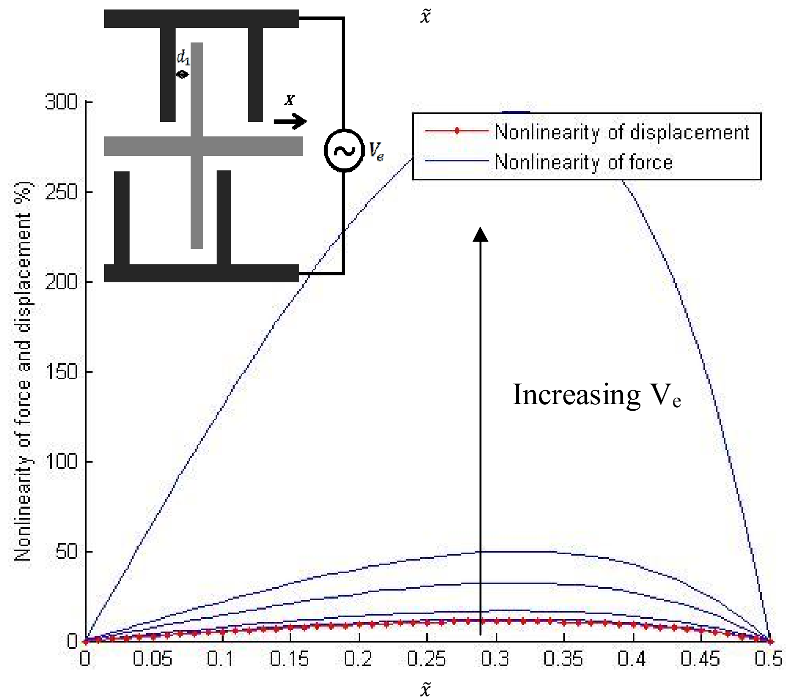

c)

d)

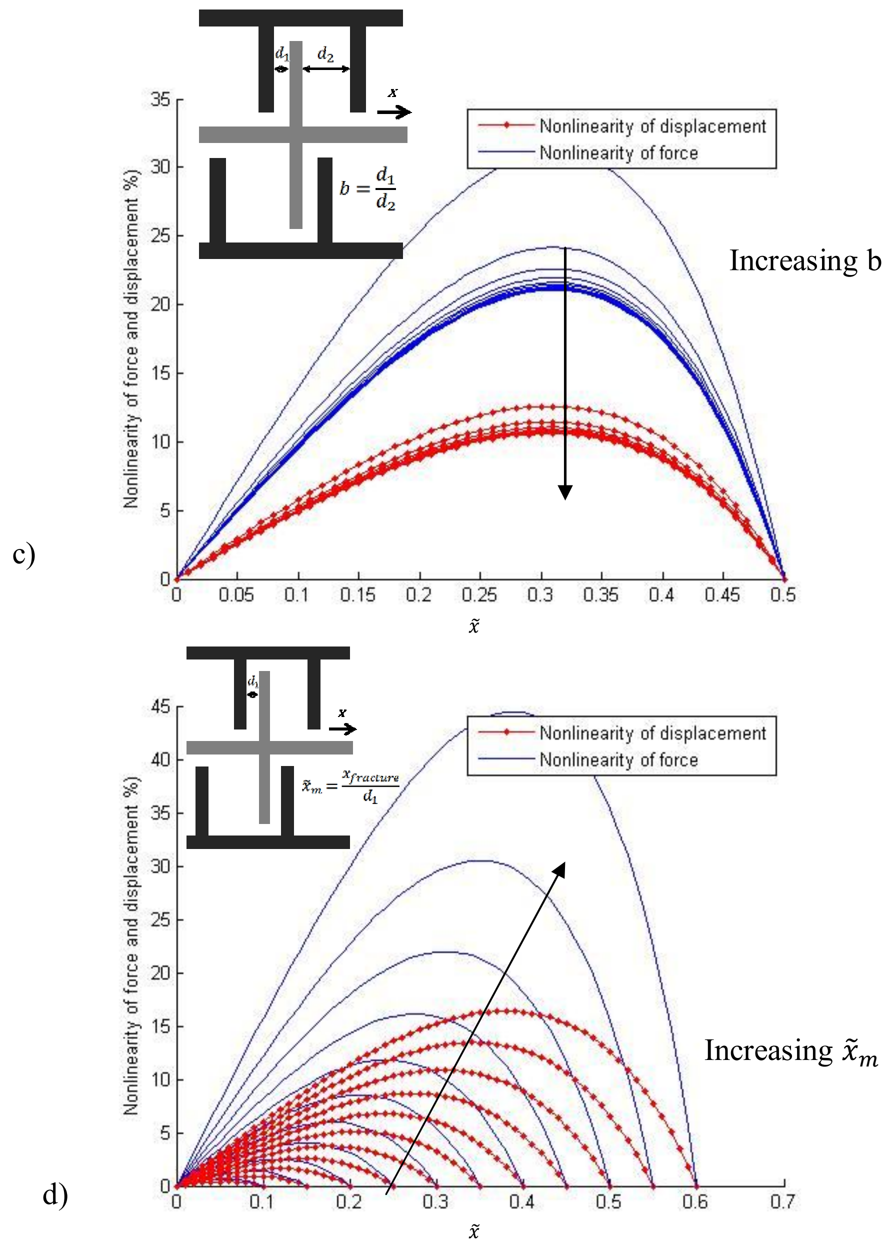

Figure 3.7: Effects of a) d_1,b) V_e,c) b and d) $\tilde{x}_m$ on the nonlinearity of the load sensor. Nonlinearity due to displacement is indicated in red whereas the nonlinearity due to electrostatic force is indicated in blue.

Parametric analysis also reveals that the stability increases as d_1 increases and decreases as V_e increases. Whereas increasing b increases stability greatly while $b < 5$ but has little effect while $b > 5$ and that $\tilde{x}_m$ has no effect on stability as seen in Figure 3.8.

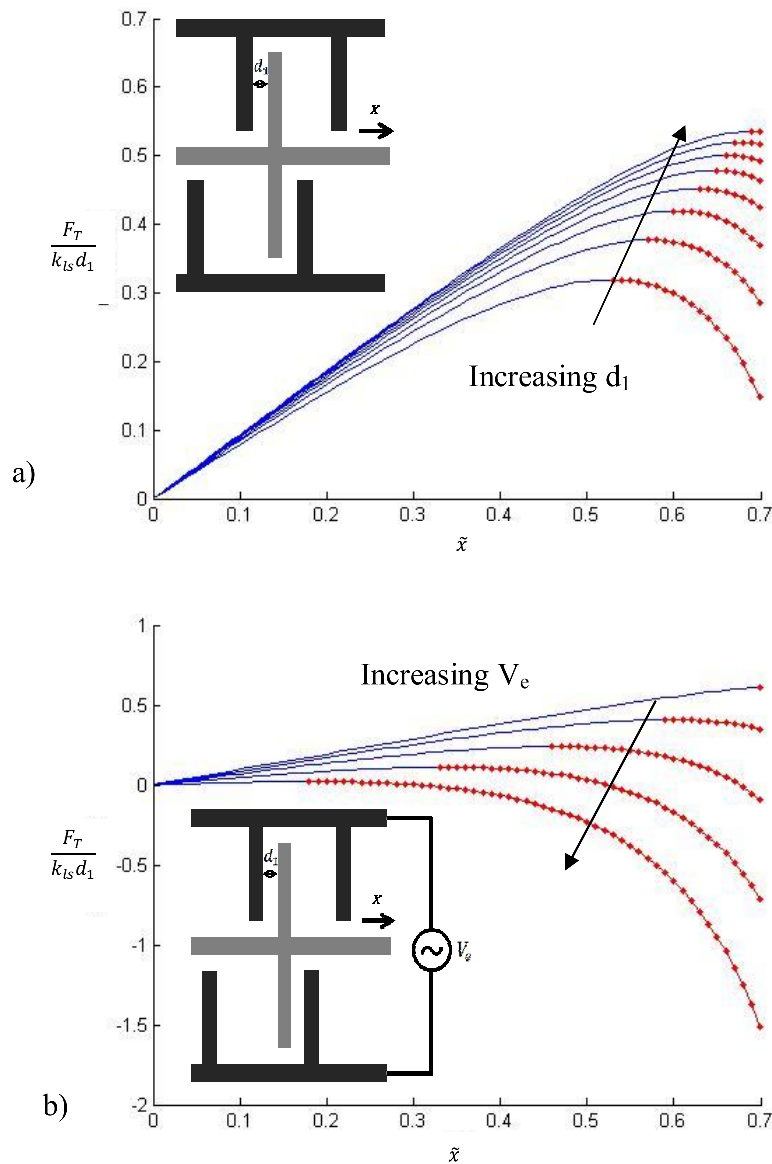

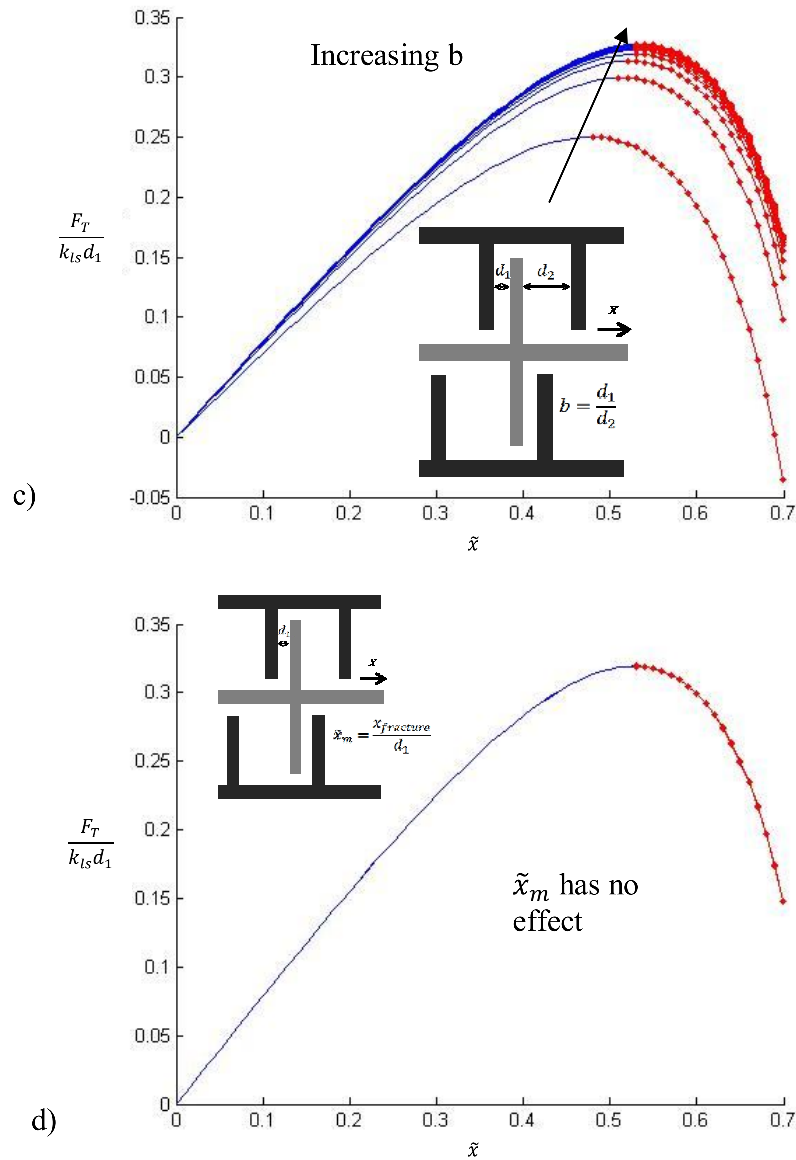

Figure 3.8: Effects of a) d_1, b) V_e, c) b and d) $\tilde{x}_m$ on the stability of the load sensor. The area in red denotes the area subsequent pull-in instability.

Parametric analysis also reveals that the number of finger sets needed increases as d_1 increases. Whereas increasing b decreases the number of finger sets needed greatly while $b < 5$ but has little effect while $b > 5$ and that increasing $\tilde{x}_m$ reduces the number of fingers needed as seen in Figure 3.9.

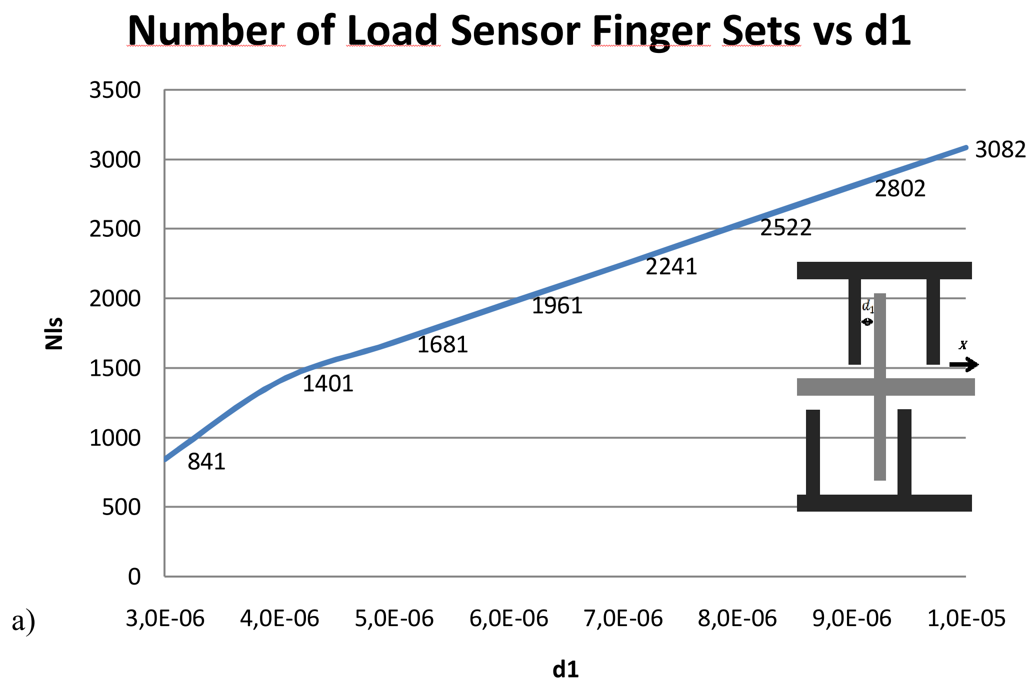

a)

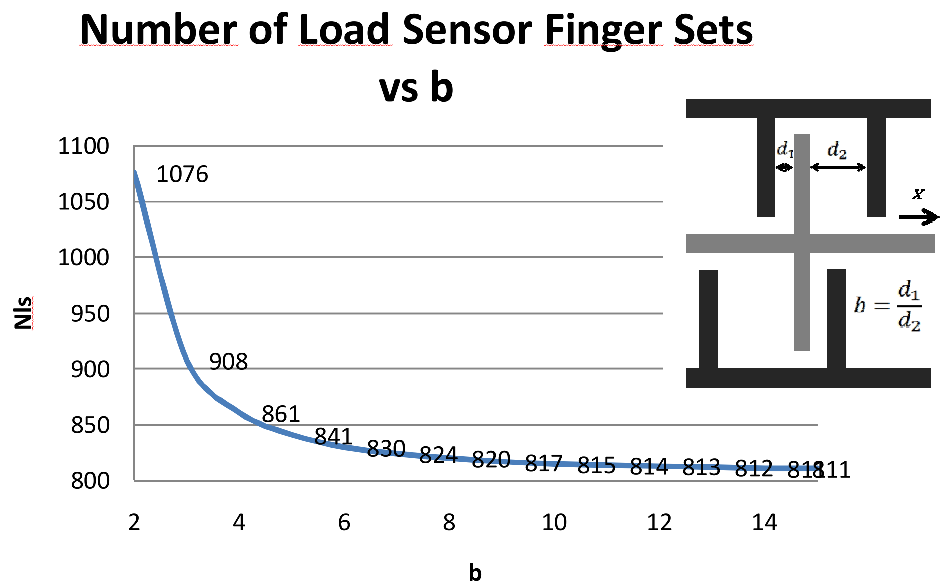

b)

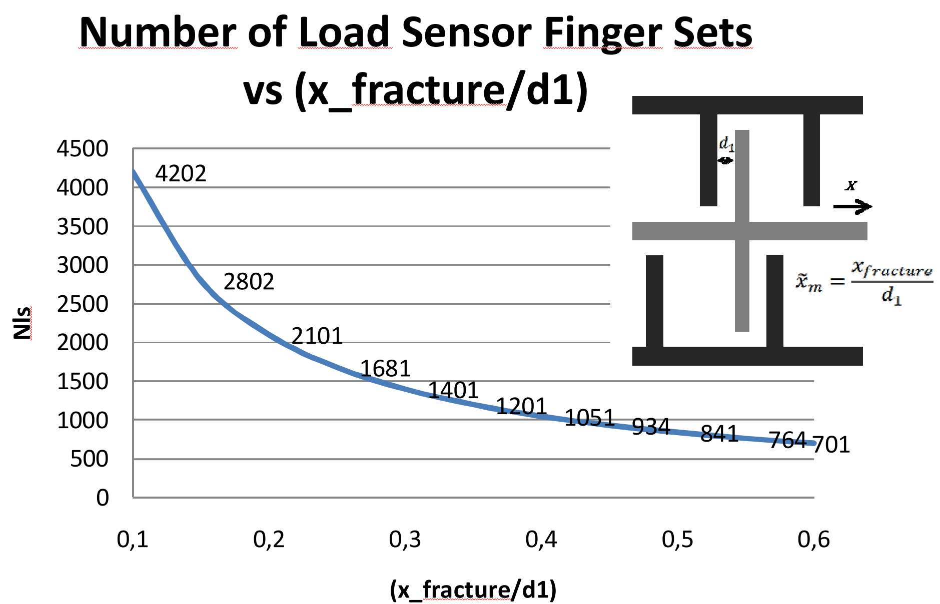

c)

Figure 3.9: Effects of a) d_1, b) b and c) $\tilde{x}_m$ (here denoted as x_fracture/d1) on the number of load sensor finger sets needed.

3.4.5.1 Actuator Parametric Analysis

The analysis is conducted for a device with a SiNW of 75 nm and $g_x = 15\ \mu m$, $t = 5\ \mu m$ and $g_y = 3\ \mu m$ when kept constant. Parametric analysis reveals that increasing g_x and g_y increases the number of actuator comb drive fingers needed as seen in Figure 3.10.

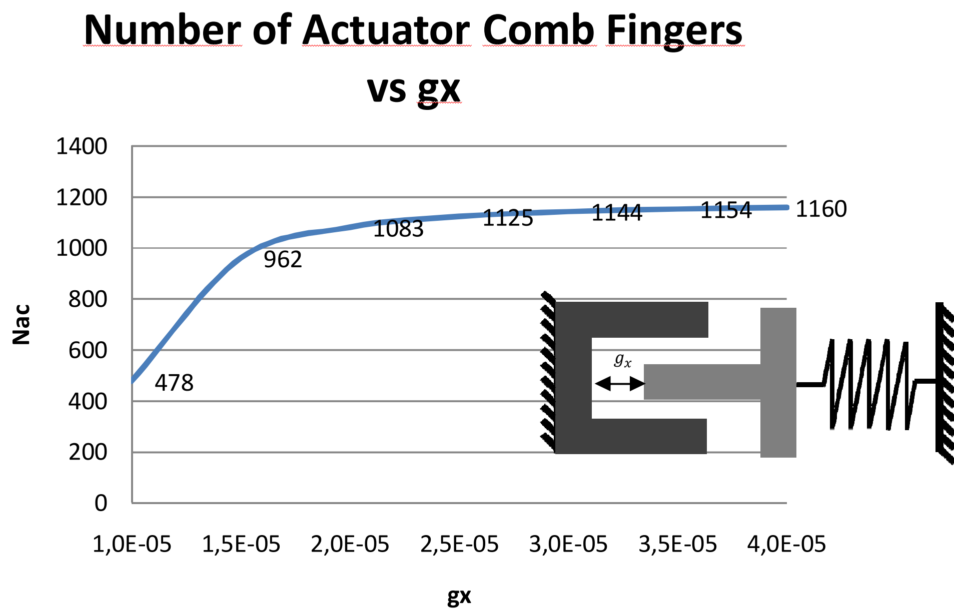

a)

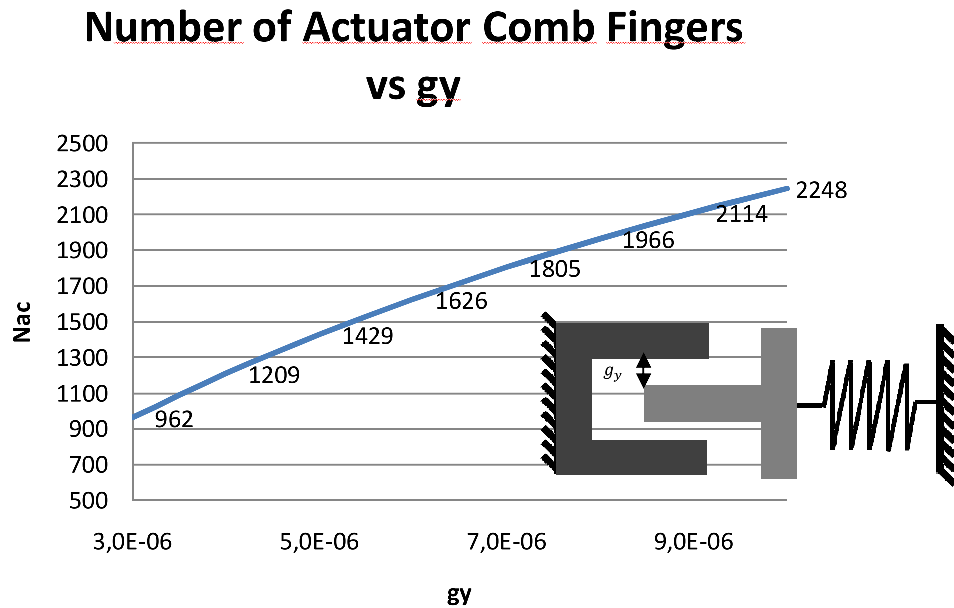

b)

Figure 3.10: Effects of a) g_x and b) g_y on the number of actuator comb fingers needed.

Parametric analysis also reveals that increasing g_x increases the displacement in which pull-in occurs while increasing g_y decreases the pull-in displacement as seen in Figure 3.11.

.

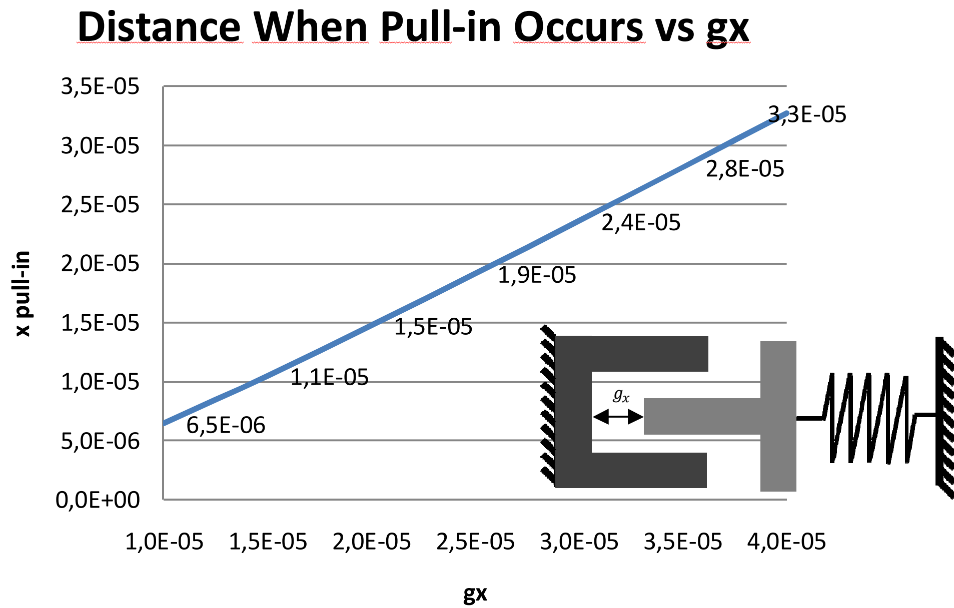

a)

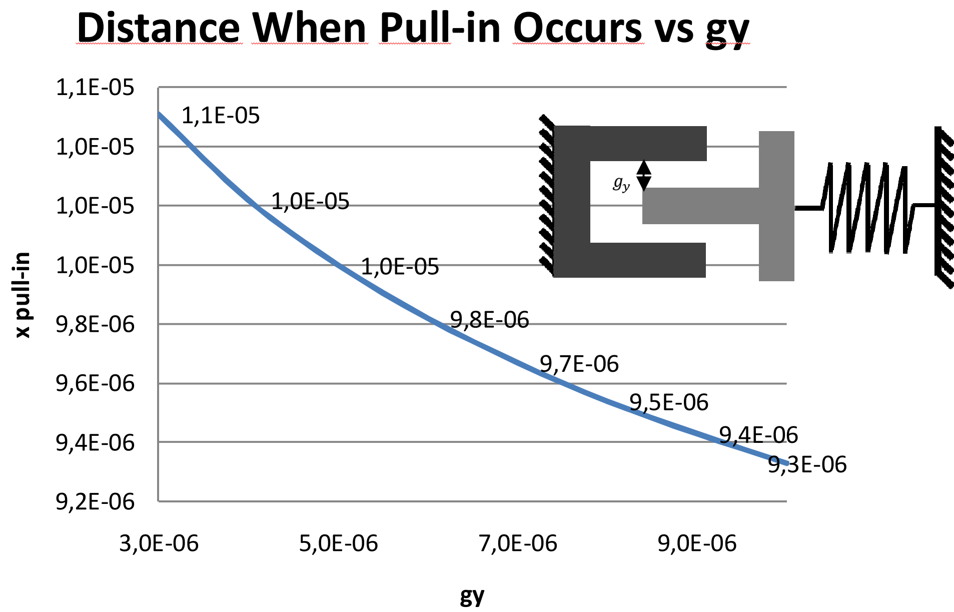

b)

Figure 3.11: Effects of a) g_x and b) g_y on the distance of pull-in instability.

Taking all these effects into account another MATLAB™ code is written to obtain the optimum device architecture. By determining certain limits to nonlinearity and complexity and eliminating instable models a final geometry is obtained.

3.4.6 Finite Element Analysis

To establish the operatability and validity of the geometry, simulation is needed. COMSOL™ software is used to carry out electrostatic, plane stress and AC analysis on the device. Due to the high complexity of the microtensile device, two-dimensional finite element analysis is decided to be conducted for the simulation. Moreover, the complexity of the device prevents full device analysis. Hence, simulation is carried out for the actuator and load sensor separately. The geometry variable values in which the simulations are conducted on can be seen in table 3.1.

Actuator Variables								
h_{ac}	w_{ac}	t	g_x	g_y	k_{ac}	V_{max}	N_{ac}	$V_{pull\text{-}in}$
7.5 µm	2.5 µm	5 µm	50 µm	1.5 µm	0.23 N/m	50 V	513	274 V

Load Sensor Variables									
h_{ls}	w_{ls}	l_{ls}	d_1	d_2	k_{ls}	V_e	N_{ls}	Nl_f	$\tilde{x}_{pull-in}$
7.5µm	5 µm	400 µm	1.5 µm	15 µm	110 N/m	2 V	89	4.69%	0.72

Table 3.1: Variable values of actuator and load sensor.

3.4.6.1 Actuator Finite Element Analysis

Analysis of the actuator is carried out using the two-dimensional electrostatic comb drive model available in the MEMS model library of Comsol 3.5 as a reference. Hence initial analyses are carried out with models similar to the reference and latter analyses are adjusted to our model. The pull-in distance is solely dependent on the geometry in electrostatic comb drive. Therefore for the initial models, the stiffness of the spring and the applied voltage is not of interest as long as pull-in does not occur in the maximum displacement needed from the actuator. Deformed form of the initial two models can be seen in Figure 3.12 and Figure 3.13. It is clearly seen that the displacement exceeds the actuator's predicted maximum displacement of 2.6 µm.

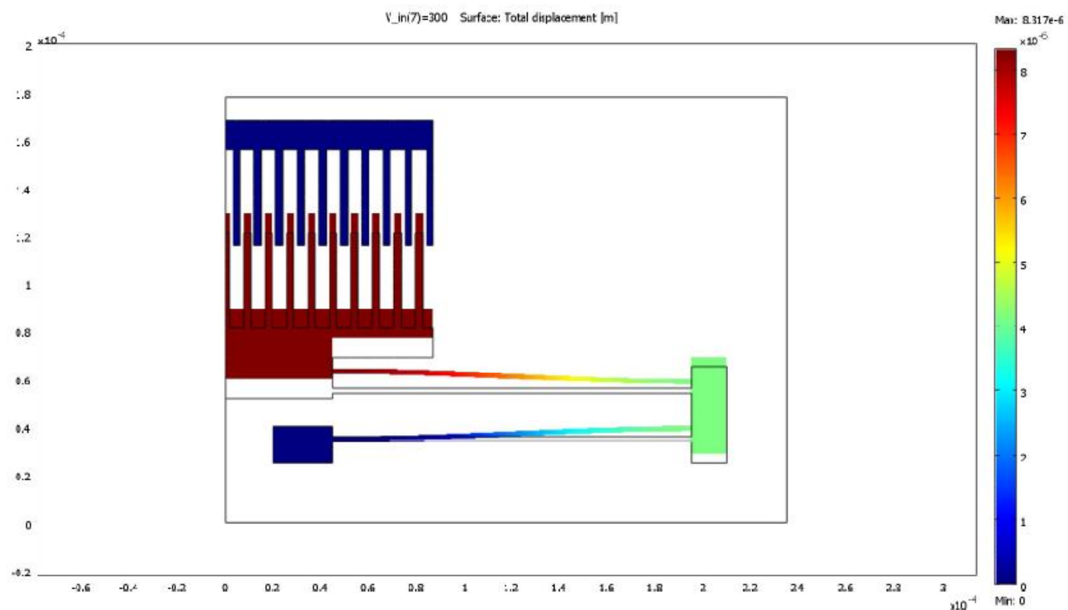

Figure 3.12: The deformed form of initial actuator analysis.

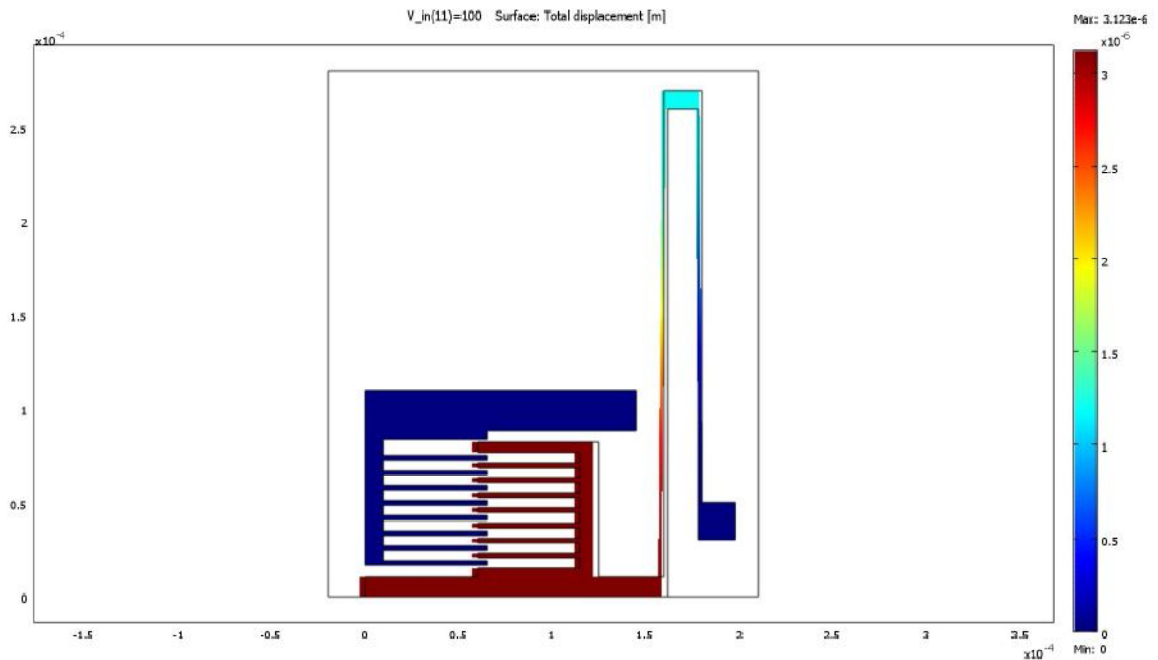

Figure 3.13: The deformed form of second actuator analysis.

Subsequent to these analyses more complex actuator analyses are conducted. The number of fingers is increased and the stiffness of the spring is adjusted such that the resultant displacement at a certain voltage difference is equivalent of those of the device. The deformed form the final actuator analysis can be seen in Figure 3.14. Although the maximum applied voltage difference to the actuator is predicted to be 50 V, the analysis is carried out until 100 V is applied.

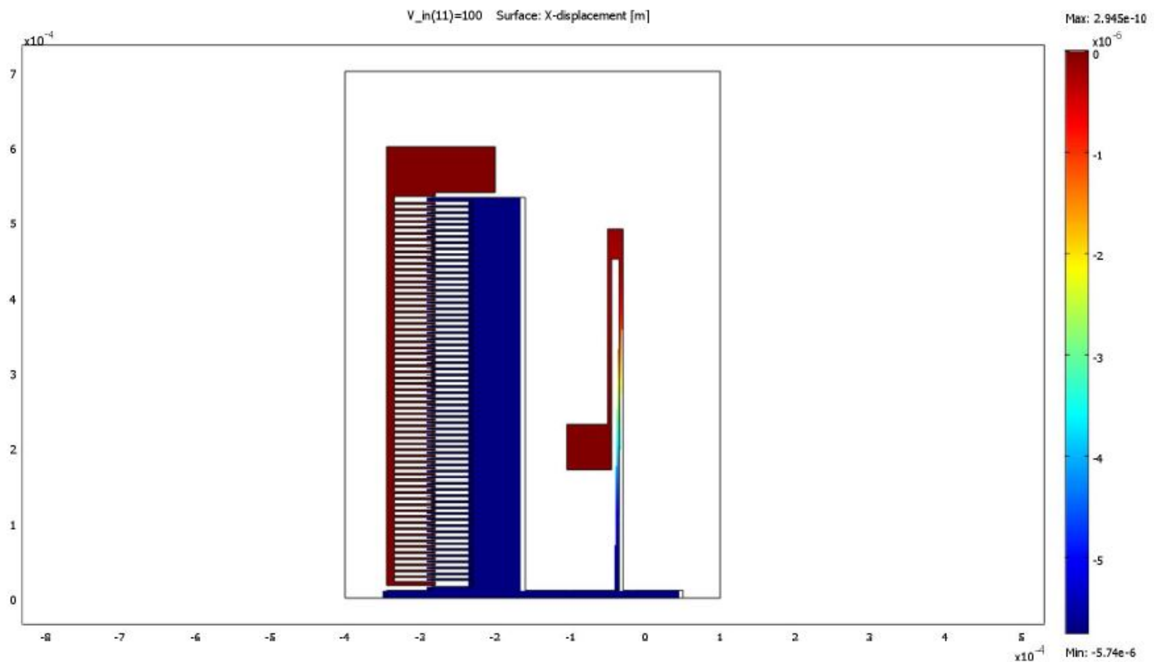

Figure 3.14: The deformed form of final actuator analysis.

The displacement versus applied voltage graph obtained by the finite element analysis is compared to the theoretical graph. It is seen that the results agree until 50 V resulting in a yield less than 1%, but as the voltage increases the results diverge from each other. The divergence is due to the stiffness hardening of the springs as the displacement is 2.5 μm and no longer can be considered small. However, the predicted maximum applied voltage is 50 V; hence the divergence has little effect on the analysis. The displacement versus applied voltage graph of both theoretical and finite element analysis and the difference graph can be seen in Figure 3.15.

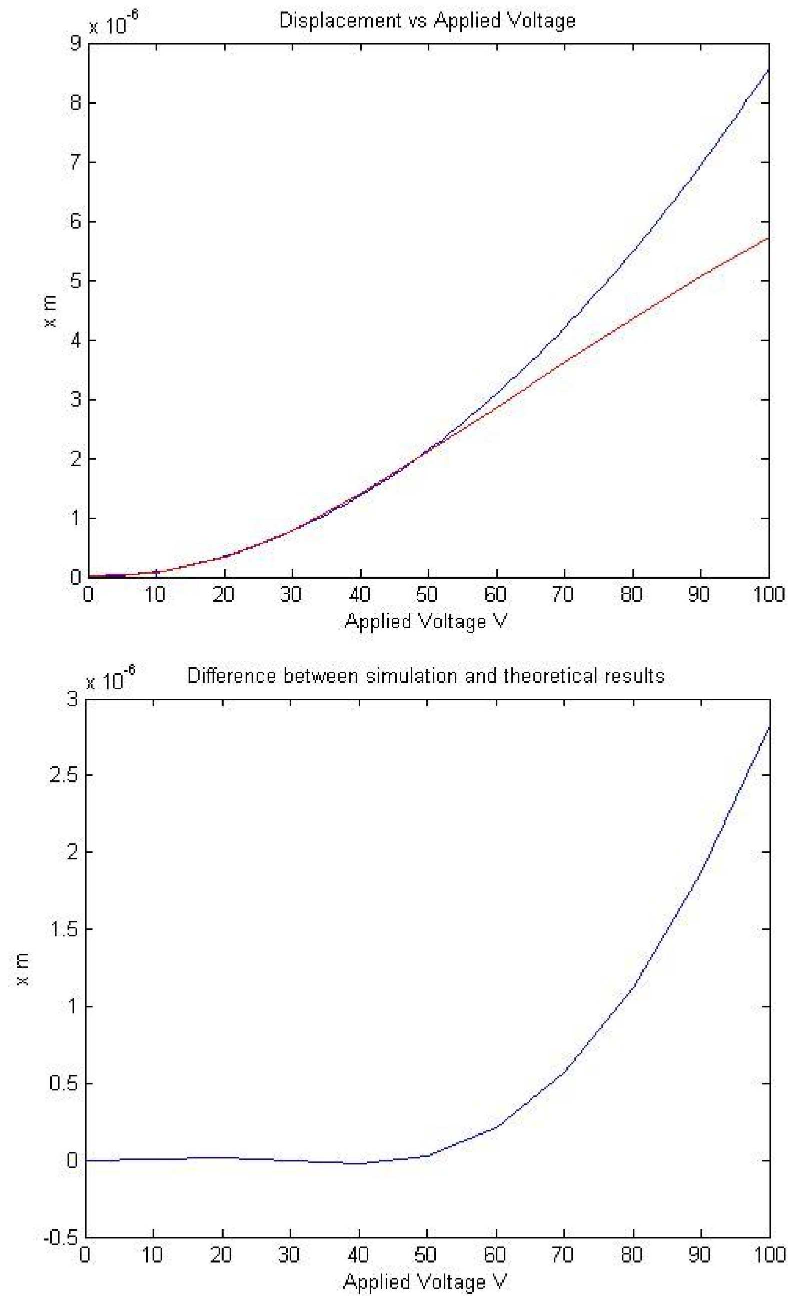

Figure 3.15: Displacement vs applied voltage graph and graph of the difference. The theoretical displacement is in blue and FEM simulation result is in red.

3.4.6.2 Load Sensor Finite Element Analysis

The load sensor of the device uses tri-plate configuration. The displacement of the movable plate induces a capacitance difference between the fixed plates. This capacitance difference is the core of its function. Hence analysis of the load sensor is focused on the induced capacitance difference. Initially half of a simplified load sensor is analyzed for the sake of simplicity. The maximum predicted displacement of the movable plate is 0.5 μm. Hence the half load sensor is displaced from -0.75 μm to 0.75 μm and the capacitance difference versus displacement graph is computed. The graph is compared with the theoretical result. The finite element results are slightly higher than the theoretical results as it can be seen in Figure 3.16. This increase is simply due to the area between the fixed and movable fingers neglected in the theoretical calculation of capacitance. The maximum displacement of the load sensor finger is 86nm which is negligible. The deformed form of the half load sensor can be seen in Figure 3.17.

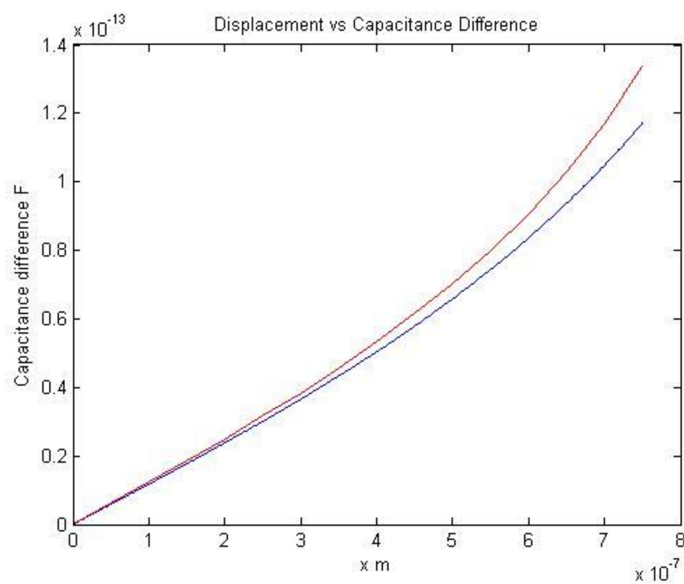

Figure 3.16: Capacitance difference vs displacement graph of FEM and theoretical results. Theoretical result is in blue and FEM result is in red.

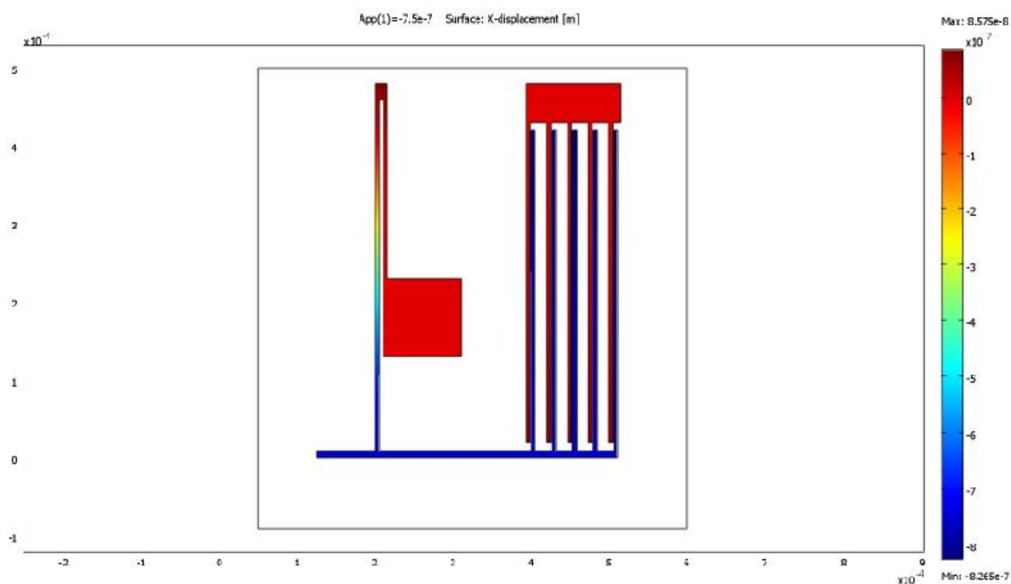

Figure 3.17: Deformed form of half load sensor

Subsequently the analysis of a full load sensor is conducted. The movable plate is displaced from 0 to 0.75 µm. The capacitance difference results are the same as the half load sensor. The deformed form of the full sensor can be seen in Figure 3.18.

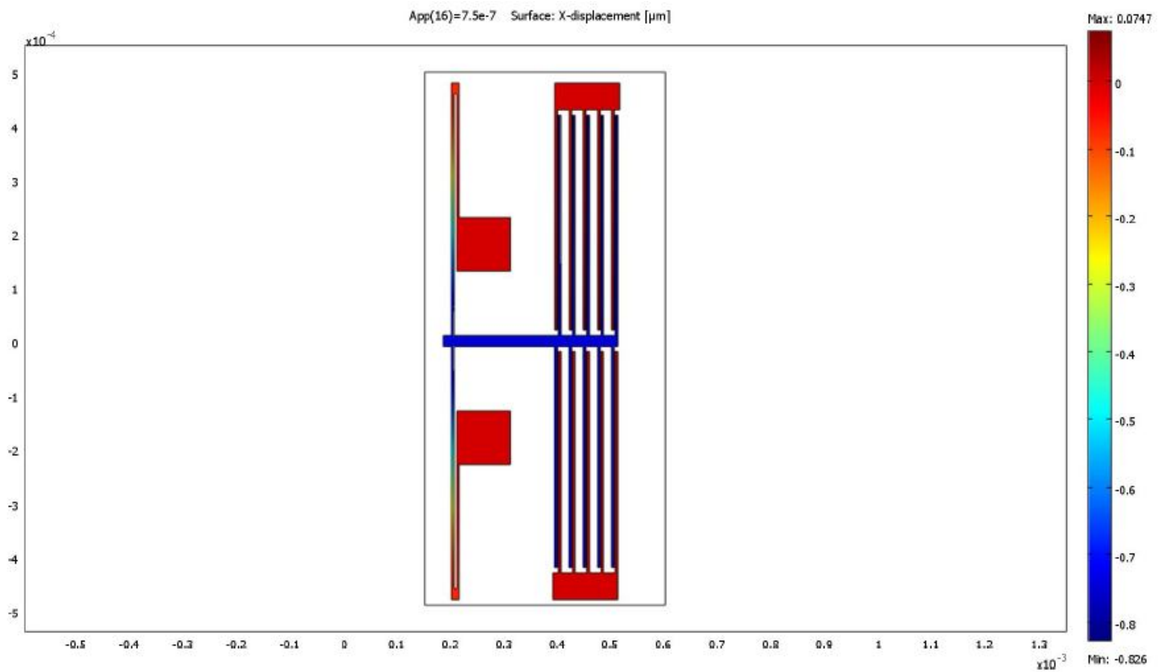

Figure 3.18: Deformed form of full load sensor

A final analysis of the functionality of the load sensor is conducted simulating AC voltage induced on the movable plate. The movable plate is displaced from 0 to 0.75 µm while AC voltages of 2 V are applied to the fixed electrodes with a 180º phase difference. The voltage induced on the movable plate due to the displacement at 0.75 µm can be seen in Figure 3.19.

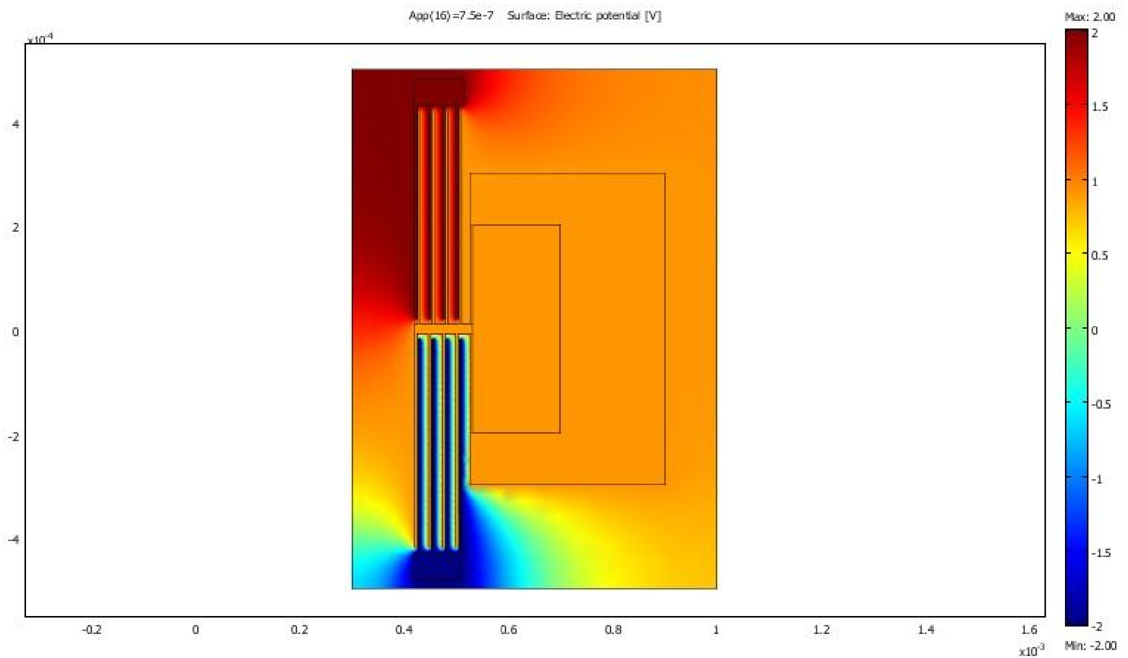

Figure 3.19: Voltage induced on the movable plate of the load sensor due to displacement.

The simulated output voltage from the movable plate is graphed and compared with the theoretical values. Theory suggests that if any losses are ignored the voltage induced on the movable plate can written as seen in equation 3.19.

$$V_{out} = V_e \frac{\Delta C}{C_{total}} \tag{3.19}$$

Where V_{out} denotes the output voltage, ΔC denotes the induced capacitance distance and C_{total} denotes the total capacitance between the movable plate and the fixed electrodes. The simulated output voltage results in a slight shift causing a deviation less than 1%. The

deviation is due to the position in which the voltage is measured as seen in Figure 3.20. Voltage is also slightly vulnerable to voltage induced from the fixed electrodes. Therefore the readout electrode has to be positioned far away from the load sensor itself.

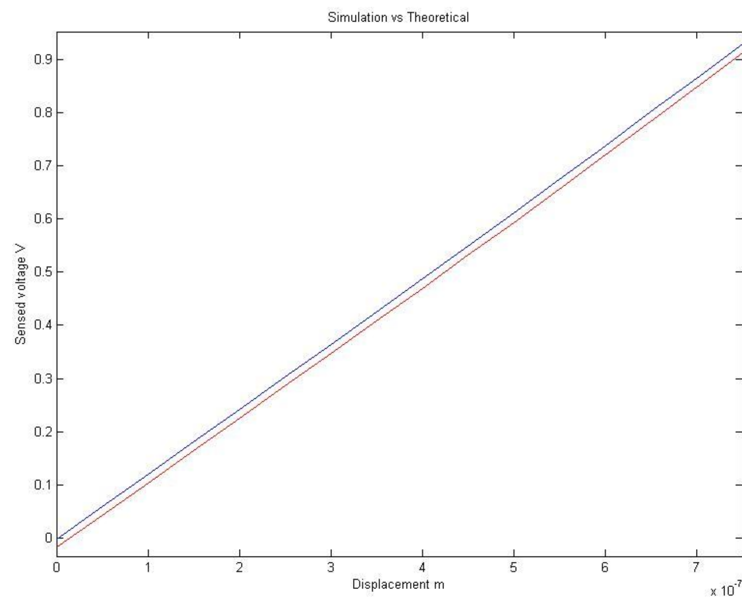

Figure 3.20: Voltage induced on the movable plate of the load sensor due to displacement. Theoretical result is in blue and FEM result is in red.

3.5. Proposed Fabrication Flow

The fabrication flow proposed is very similar to that of Zhang *et al* [12]. The main diffence that is introduced is that the SiNW sample is fabricated on the device eliminating the need for complex integration methods such as nanomanipulation and FIB Pt deposition.

Starting from a doped SOI wafer of 4 inch, SiO_2 is grown using low pressure chemical vapor deposition (LPCVD) (Figure 3.21.b) . The grown SiO_2 serves as a hard mask for the subsequent lithrography steps. SiNW line is defined by the mean of e-beam lithography (Figure 3.21.c) and half of the SiO_2 is etched (Figure 3.21.d). It is crucial that enough SiO_2 remains for a second mask. After the photoresist (PR) is etched (Figure 3.21.e) and the wafer is cleaned the second photolithography that defines the MEMS device is conducted (Figure 3.21.f). The device mask consists of the device and additional halo masks to eliminate microloading effect. Halo masks are dummy masks that decrease the area prone to the etchant reesulting an almost constant gap throughout the device. The remaining SiO_2 is etched (Figure 3.21.g) and following the PR strip (Figure 3.21.h), the full mask defining the device and the SiNW is obtained. Consecutively Bosch process is carried out to form scalloped walls (Figure 3.21.i). Either wet or dry oxidation is carried out to form the SiNW sample (Figure 3.21.j). Oxidation step allows the consumption of excess Si on the trench walls of the SiNW line. Careful oxidation can allow one to form an array of SiNW as well as a single SiNW on the uppermost edge of the SOI wafer. To form the SiNW sample oxidation is carried until nearly all the SiNW line is consumed while the uppermost Si is preserved by the SiO_2 hard mask.

Following the oxidation a third photolithography step is carried out to protect the SiNW from the subsequent fabrication steps (Figure 3.21.k). After the excess PR is etched the wafer is diced into chips. Then SiO_2 is etched and the halo masks are detached from the chips (Figure 3.21.l). Some remaining SiO_2 remain around the SiNW. Cr and Au is evaporated on the surface to ensure ohmic contact (Figure 3.21.m). The PR protects the SiNW from being covered with Cr and Au to eliminate any undesirable alterations on the SiNW sample to ensure the quailty of the test. The PR is etched revealing the SiO_2 covering the SiNW (Figure 3.21.n). As the final step the SiO_2 is etched and the SiNW is released (Figure 3.21.o).

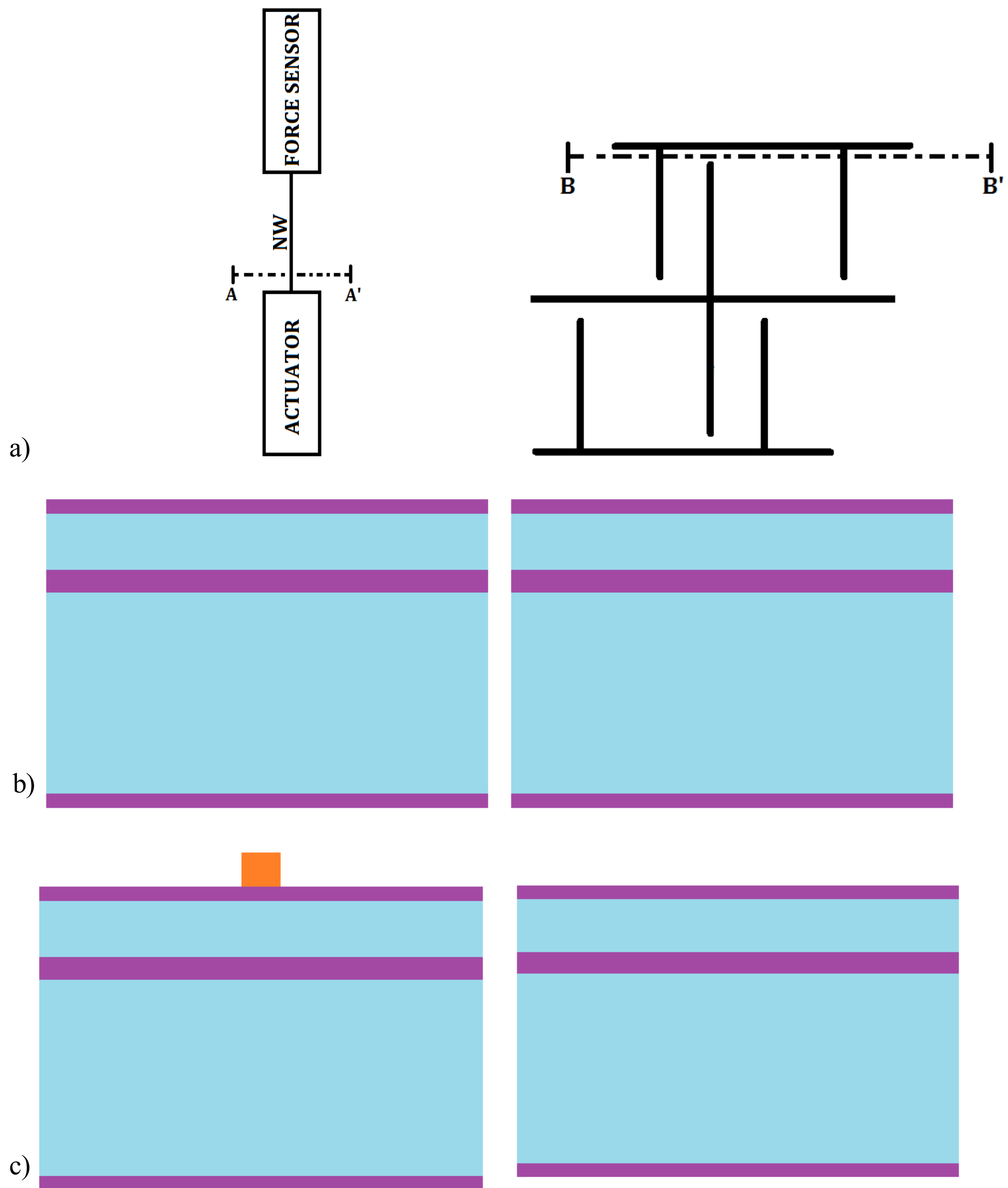
FORCE SENSOR
NW
A
A'
ACTUATOR
B
B'
a)
b)
c)

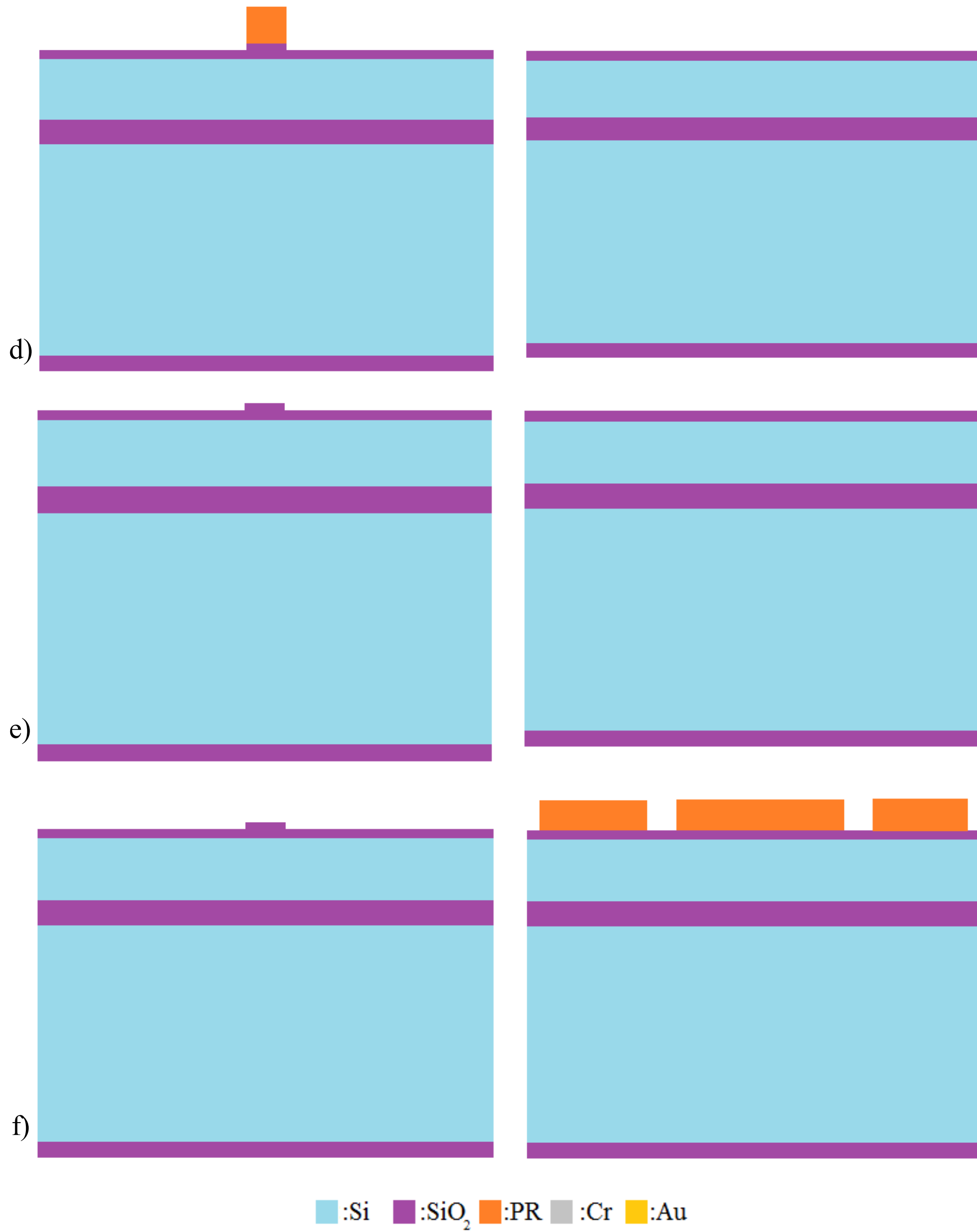
d)
e)
f)
:Si
:SiO2
:PR
:Cr
:Au

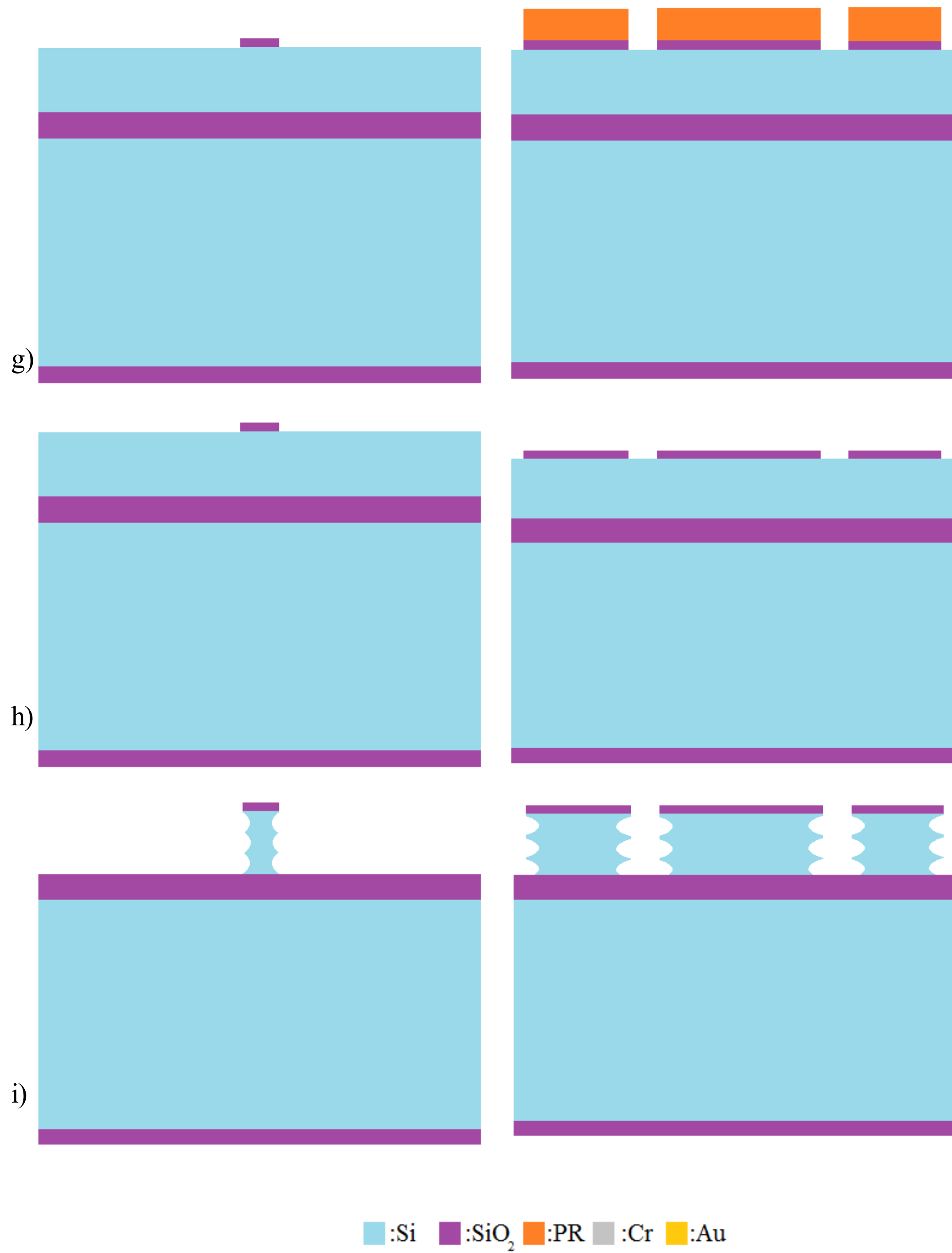
g)
h)
i)
:Si
:SiO2
:PR
:Cr
:Au

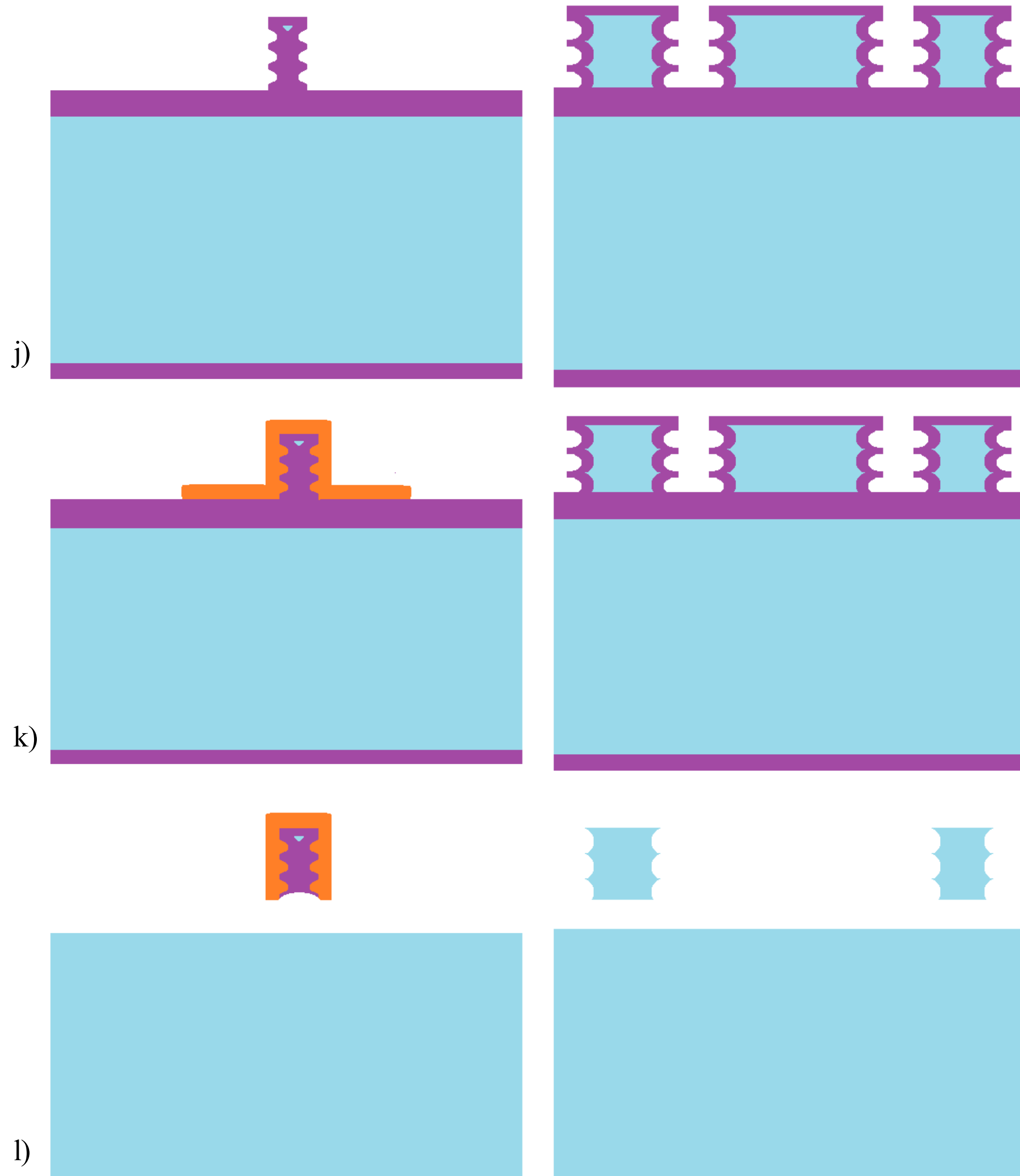
j)
k)
l)
:Si
:SiO2
:PR
:Cr
:Au

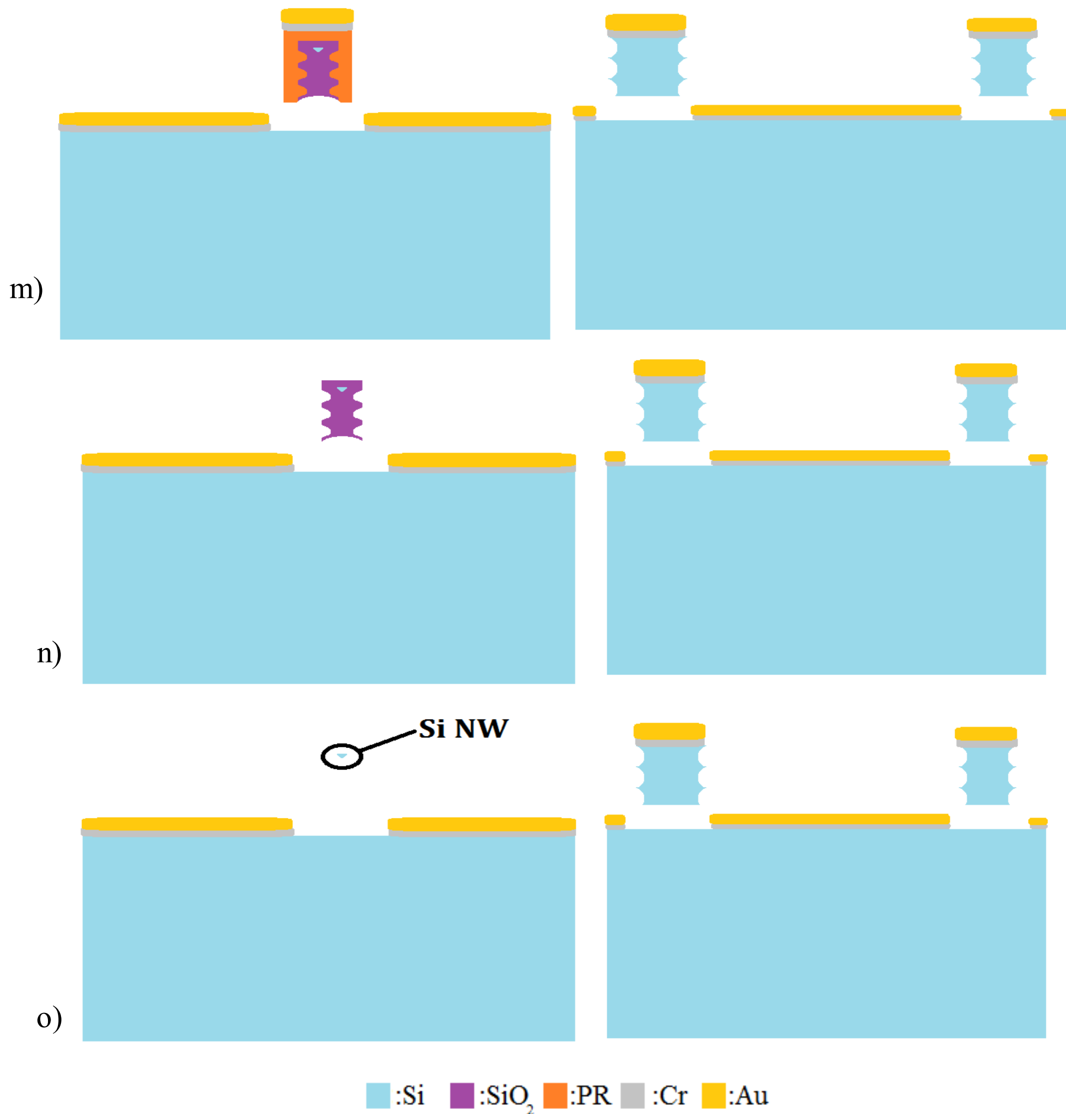

Figure 3.21: Fabrication flow of the microtensile testing device. a) The left side demonstrate the AA' cross-section and the right side demonstrate the BB' cross-section as shown. a) LPCVD SiO_2 growth c) e-beam lithography d) Oxide etch e) PR strip f) Photolithography g) Oxide etch h) PR strip i) Bosch process j) Oxidation k) Photolithography l) Oxide etch m) Cr-Au evaporation n) PR strip o) Oxide etch

Chapter 4

RESONANCE AND THREE POINT BENDING CHARACTERIZATION

4.1 Introduction

SiNWs were investigated as resonators beginning from the late nineties for gravimetric sensing applications [50]. With the advances in fabrication methods the size of SiNWs reached below 10 nm [25, 51, 52]. Using different measurement methods the resonance of SiNWs ranging from 400 kHz [53] to about 400 MHz [54] were measured. Quality factors up to 25000 [25] were achieved in vacuum, whereas, in air, quality factors ranged between 150 [55] to 400 [56]. SiNWs were brought to resonance either electrostatically [50, 53-55, 57, 58], magnetomotively [3, 59, 60], by thermal excitation [56] or by the use of base excitation via a piezoelectric stage [25, 61-64]. Optical interference [25, 50, 54-56, 62] or capacitive [57, 58], magnetomotive [3, 60] and piezoresistive [63, 65] readout techniques were employed for the detection of resonance.

Compared to resonator applications, the use of SiNWs as electromechanical switches was demonstrated more recently [66]. Although carbon nanotubes (CNTs) form the main class of nanostructures used in electromechanical switch application [67-69], their synthesis generates both metallic and semiconducting CNTs rendering CNT-based NEMS difficult to predict. On the contrary, with the possibility of tailoring both their electronic properties and critical dimensions during growth, SiNWs provide a reliable switch behavior

[70]. Such switches were originally fabricated by clamping SiNWs near a metal electrode and measuring the pull-in voltage [70-72]. Resultant devices had no power consumption at the off-state and exhibited an on/off current gain of 10^4.

In device applications - similar to those mentioned above - a deterministic assembly is highly preferable. Integration of SiNWs with higher-order structures constitutes the most critical step for the functionality of NEMS as many nanofabrication techniques are not compatible with photolithography. In VLS, one of the most widely used bottom-up techniques for SiNW fabrication, two major approaches for integration are available. VLS results in well-controlled diameter and crystallographic orientation, which is <111> for SiNWs with a diameter larger than 20 nm and <110> for SiNWs with a diameter lower than 10 nm [73]. The main integration approach for VLS products is to disperse synthesized NWs in a solvent, where they are subsequently directed into alignment. Alignment can be achieved by applying external electric or magnetic fields or inducing a microfluidic flow over the dispersed SiNWs. These methods require lengthy and complex procedures with limited yield. There are reported applications of such an approach to fabrication of SiNW resonators [64]. In the alternative method, SiNWs are synthesized on the spot of interest. This necessitates selective placement of catalytic Au particles through a nanolithographic technique. The yield is much better than that achieved through external alignment, and hence, most of the device demonstrations utilize this on-site growth technique [3, 25, 60, 62, 63]. In addition to proper patterning, subsequent fabrication of excitation and read-out components brings about its own set of challenges including material selectivity for various deposition and etching steps.

Integration can also take place through a top-down technique. The most direct approach is placement of NWs with a manipulator. Its complexity resembles direct-write techniques such as e-beam-induced deposition or focused ion beam milling. This method

was employed in the fabrication of SiNW resonators in [53] and SiNW switches in [66, 71, 72].

Alternatively, a nanolithographic technique can be used either as a positive process where anisotropic etching defines a SiNW beneath a mask or as a negative process where a trench is used as a mold for the subsequent deposition of a nanowire. The latter technique is more applicable in the case of polycrystalline metallic NWs deposited through electroplating, whereas the former technique requires a very thin device layer such as the single crystalline SiC film used in a resonator study [74]. Various reported work is also available on SiNW resonators using this approach [50, 54-59, 61, 65]. For single crystalline Si a similar approach is possible with SIMOX wafers with a very thin Si layer on buried oxide [75]. Further reduction in size can be achieved through oxidation [76]. Working with much thicker Si layers is also possible when one uses the scalloping effect of the Bosch process in inductively coupled plasma deep reactive ion etching (ICP-DRIE). In this technique one takes advantage of the undercuts created by the isotropic etch step [77]. This technique also raises the possibility of fabricating a vertical array of SiNWs. A comparison of these techniques is provided in Figure 4.1. As opposed to the bottom-up approach to SiNW integration, such top-down techniques inherently possess a higher potential for systems integration.

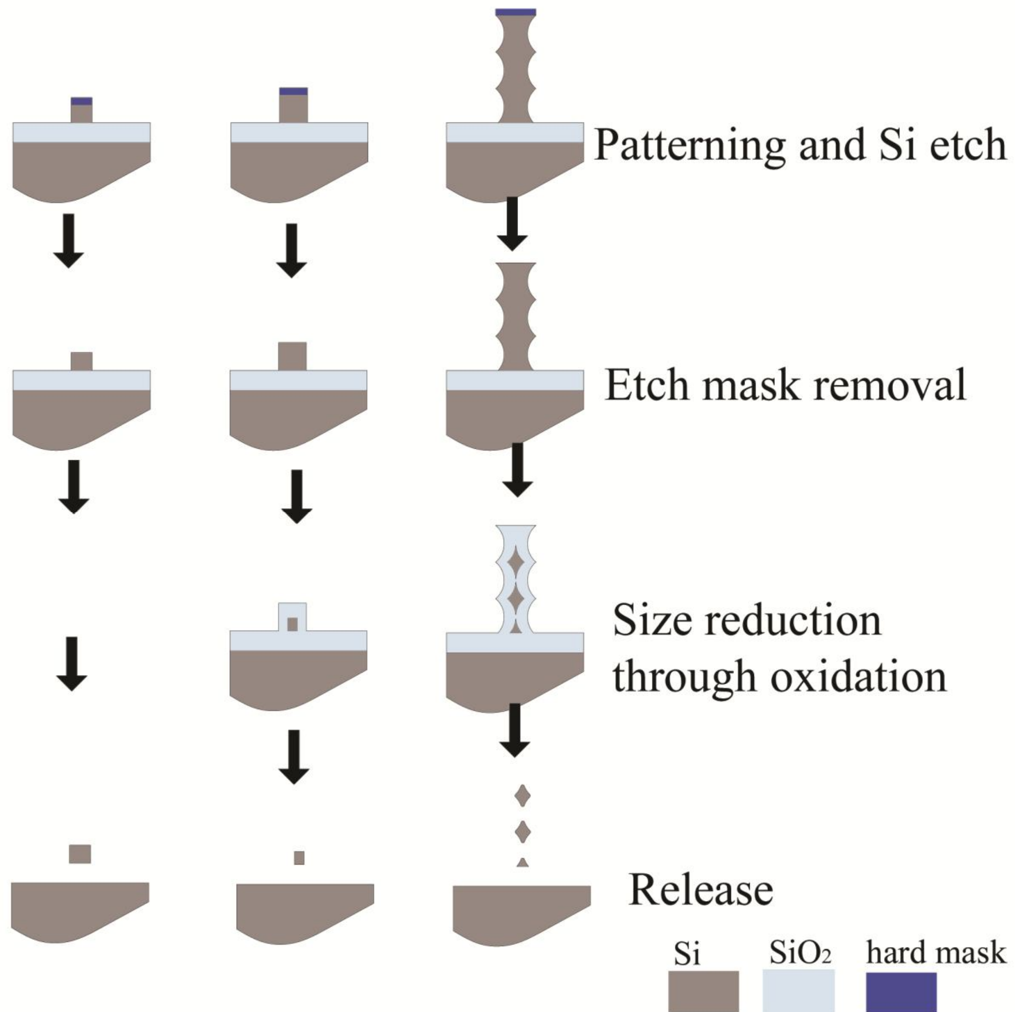

Figure 4.1: Different approaches to single-crystalline SiNW formation using top-down patterning and etching.

Scalloping, seen in the third column in Figure 4.1, is a well-known phenomenon encountered in Bosch process in ICP-DRIE, where the chemical etch step leads to small undercuts on side walls. The extent of this undercut is a direct indication of chemical etch parameters such as etch duration. Hence, by adjusting chemical etch parameters one can

change scallop geometry. If one etches a thin column (around 1 μm thickness) from both sides via Bosch process in ICP-DRIE, the scallop geometry can be adjusted to consume Si until the scallops meet and form a single SiNW whose diameter can be further decreased through oxidation [78-83]. In similar studies, oxidation is shown to act as a modifier of the SiNW and pentagonal [81-84], triangular [79, 80, 82] and circular cross-sections [78] can be obtained. Most of these studies are based on isotropic etching with pronounced undercut effect. In addition, a vertical array of Si strings can be achieved with Bosch process. By further oxidation and sacrificial etch, a stack of SiNWs can be obtained as a result. This technique is unparalleled in its ease of producing vertical SiNW stacks as well as a single SiNW in a thick Si device layer.

The technique based on the Bosch process was first introduced by Milanovic *et al.* [77] in an effort to fabricate lateral field emission devices. Doherty *et al.* investigated the relationship between the SiNW diameter and photoresist width and fabricated nanochannels utilizing ICP-DRIE [85]. Ng *et al.* further investigated the effect of oxidation on the eccentricity of the formed SiNWs and suggested that eccentricity decreases as oxidation time increases [86]. Following this research Ng *et al.* employed this method to form vertically stacked SiNW transistors [87]. Supplementary to these studies, Ozsun *et al.* investigated the aspect ratio and depth limits of this method and the mechanical integrity of fabricated SiNWs [88]. In addition, patterns other than straight SiNWs and integration of SiNWs with microsystems or MEMS such as microtweezers were demonstrated. Bopp *et al.* presented an additional process flow to fabricate separated vertical stacks of SiNWs [89].

In this work, the technique based on the Bosch process is used to produce a single SiNW within a thick Si device layer to demonstrate suitability for systems integration in nanomechanical resonator and switch applications. In such applications, if integration with electronics is targeted, electrostatic actuation and capacitive readout are necessary, as

optical or magnetic means are incompatible with the associated systems requirements. This raises the need for metallic components, as they reduce loss throughout the device due to their low resistance and serve as high performance electrodes both for actuation and readout, base grounding and shielding components. Hence, metal elements – aluminum in this case - should be incorporated into the design to ensure high quality performance and ease the integration to more complicated CMOS circuits.

For this purpose, the ICP-DRIE technique is extended in a unique way to incorporate metallic elements as actuation and readout electrodes. The major claim of the work is the enhancement of CMOS integration for future, NEMS-based, on-chip components. Surface micromachining with a combination of conventional photolithography and self-aligned masking through chemical-mechanical polishing (CMP) is utilized, reducing the overall complexity of the process. Instead of a single SiNW, the fabrication method is also adjustable for the fabrication of SiNW stacks between metallic electrodes. In the remainder of this paper the architecture of the device and instrumentation are introduced first followed by the fabrication of the devices. Nanoelectromechanical resonator and switch applications are demonstrated next. The mechanical behavior and structural reliability of the proposed system are also characterized using a three-point bending test.

4.2. System Architecture and Instrumentation

The chosen architecture for the device is a single SiNW suspended in a doubly-clamped fashion between two Al electrodes as seen in Figure 4.2. Al electrodes are of 1.5 μm thickness and reside on the buried oxide (BOX) layer of the SOI wafer on which the device is fabricated. Fabricated SiNWs are along <100> orientation and have a length of 50

μm and diameters of 50-200 nm. Al electrodes extend throughout the whole length of SiNWs with a gap of 900 nm on both sides.

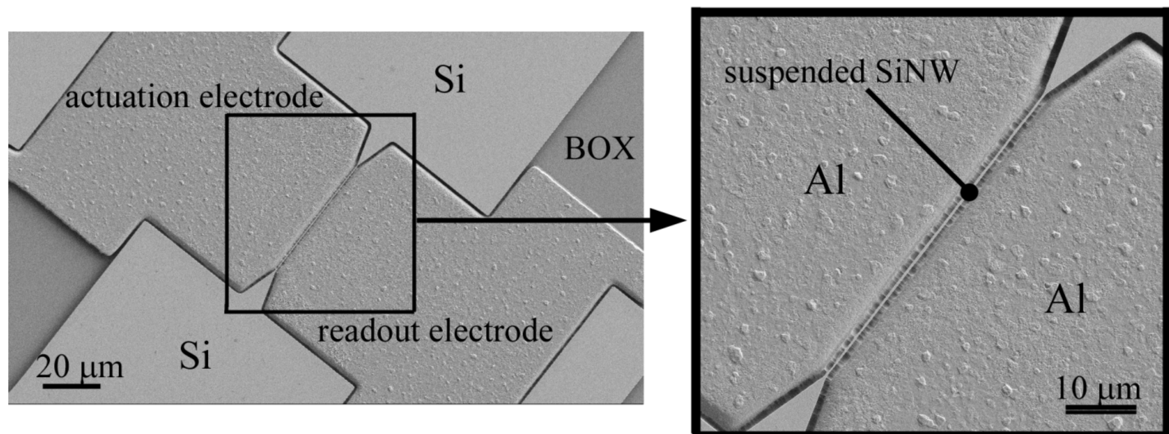

Figure 4.2: SEM image of the device.

4.2.1 Nanoelectromechanical Resonator Geometry and Instrumentation

Electrostatic actuation and capacitive readout are commonly employed in nanoelectromechanical resonators [3]. A similar approach is utilized here to characterize fabricated SiNW-electrode assembly as a resonator. A HP 8753 D network analyzer is used to actuate and carry out transmission measurement as depicted in Figure 4.3. An amplifier is placed between the network analyzer and the readout electrode. The amplifier was constructed on a breadboard utilizing a 1pF capacitor, 8kΩ resistor and a LM741 operational amplifier. The cut-off frequency was measured and observed to be at 3.3 MHz, far from the resonance zone. Measurements are carried out in a Cascade probe station. The Cascade probe station was positioned in room temperature and atmospheric median without a Faraday cage which introduced difficulties such as increased Brownian motion and

decreased quality factors. Experiments were carried out in two different devices with the same crystalline orientation.

The amplitude of the AC voltage, V_{ac}, applied to the actuation electrode is kept at 40 and 400 mV. Six sets of experiments are carried out by increasing the DC bias, V_{dc}, applied to the Si pads from 0 V to 70 V. In each set of experiments a frequency sweep is conducted to detect resonance.

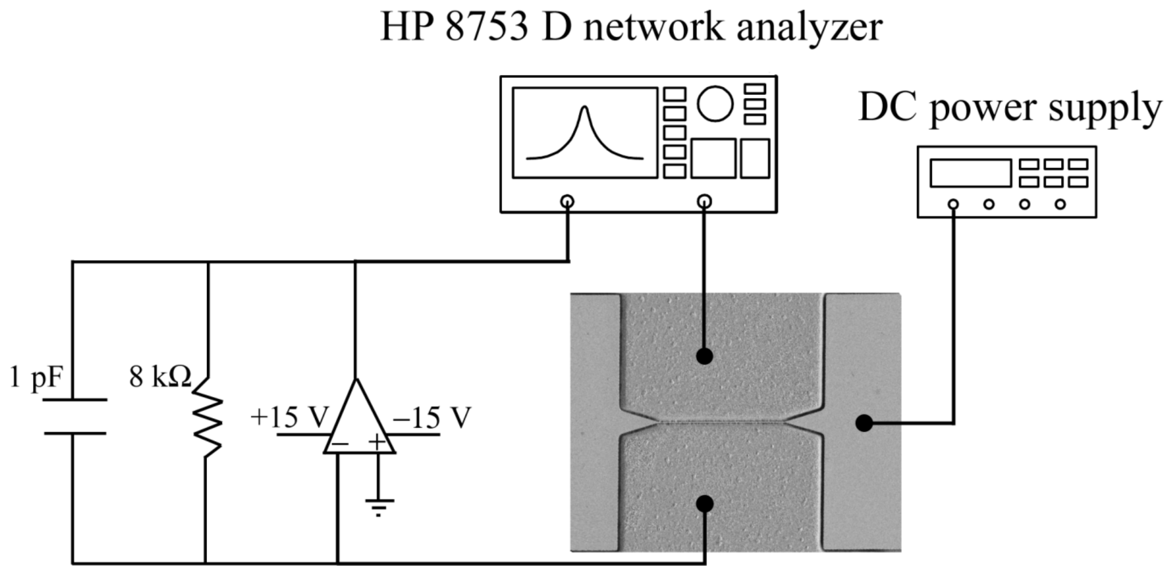

Figure 4.3: Schematic setup for resonator application.

This readout geometry tracks the motional current as a result of capacitive changes between the SiNW and the read-out electrode as the SiNW is at resonance. On the other hand, there exists a large parasitic capacitance between the electrodes that dominates the measurements. Finite-elements simulations of the device estimate a parasitic capacitance of 18 fF. It is due to this large parasitic effect that measurements obtained from the network

analyzer cannot directly demonstrate the resonance of SiNWs. To remove the parasitic current from measurements, the following formulation is needed:
Total current, I, obtained from the readout electrode can be written as:

$$I = I_p + I_m \cong C_p \frac{\partial V_{ac}}{\partial t} + (V_{dc} + V_{ac}) \frac{\partial \Delta C}{\partial t} \tag{4.1}$$

where, I_p is the parasitic current, I_m is the motional current, C_p is the parasitic capacitance and ΔC is the capacitance difference due to SiNW vibration. In the absence of V_{dc}, resultant current can be written as:

$$I = I_p + I_m \cong C_p \frac{\partial V_{ac}}{\partial t} + V_{ac} \frac{\partial \Delta C}{\partial t} \tag{4.2}$$

Since $\Delta C \ll C_p$, the term given in Equation 4.2 becomes equal to the parasitic current. As a result, the current measured when the SiNW is grounded can be taken as the parasitic current. Furthermore, when $V_{dc} \gg V_{ac}$, resultant current can be simplified as:

$$I = I_p + I_m \cong C_p \frac{\partial V_{ac}}{\partial t} + V_{dc} \frac{\partial \Delta C}{\partial t} \tag{4.3}$$

Therefore, to eliminate the parasitic current from measurements, the measurement taken at zero V_{dc} (Equation 4.2) should be subtracted from data obtained at a given V_{dc} (Equation 4.3).

Resonance frequency is a function of the stiffness of SiNWs, which derives both from the elasticity of silicon crystal and its internal stress. Previous studies suggest that a SiNW above 100-nm critical dimension should exhibit modulus of elasticity of bulk Si as summarized in [17]. Hence, any variation in our study from analytical predictions will be

taken to be a result of intrinsic stresses, which can be formulated as given in Equation 4.4 [90].

$$\omega = \frac{\beta^2}{2l^2}\left(\frac{EI}{\rho A}\right)^{1/2}\sqrt{1+\frac{2l^2}{7h^2}\varepsilon_s} \quad (4.4)$$

Here, ω is the resonance frequency, ε_s is the longitudinal strain due to intrinsic stress, $\beta = 4.73$ is the first mode shape parameter, l is the length, h is the thickness, I is the moment of inertia, A is the cross sectional area, ρ is the density and E is modulus of elasticity of the SiNW. Using this formulation the effect of internal stress can be quantified.

4.2.2 Nanoelectromechanical Switch Geometry and Instrumentation

As well as the resonator application, utilized geometry also provides a suitable platform for switch applications. As the voltage difference between SiNW and a nearby electrode is increased, SiNW deflects toward the electrode until pull-in occurs and SiNW attaches itself to the electrode. Pull-in manifests itself as a jump in the current between SiNW and the read-out electrode. The schematic of the setup can be seen in Figure 4.4. Here devices are placed in a Cascade probe station positioned in room temperature and atmospheric median without a Faraday cage with the probes connected to an HP 4156A semiconductor parameter analyzer (SPA). A DC voltage of -40 V is applied to the Si pads and one electrode, whereas a DC voltage varying from -40 V to 40 V is applied to the counter electrode. As the voltage difference is increased, the current between ports C and D is monitored.

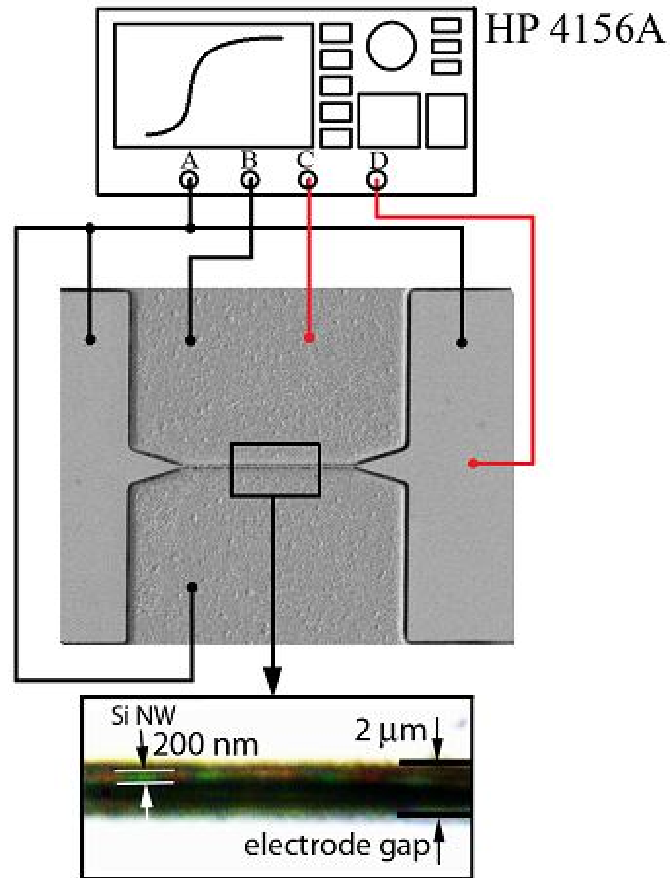

Figure 4.4: Schematic of the switch application setup. -40 V was applied from port A and the voltage applied by port B was swept from -40 to 40 V. The current between the ports C and D was measured. Inset is the micrograph of a SiNW after pull-in.

Pull-in voltage, V_{PI}, can be calculated analytically by the following formula [91]:

$$V_{PI} = \sqrt{\frac{8K_{eff}{d_o}^3}{20.9\varepsilon_0 l b_{eff}}} \tag{4.5}$$

where K_{eff} is the effective stiffness of the resonator, d_0 is the zero-voltage gap between SiNW and read-out electrode, ε_0 is the permittivity of free space and b_{eff} is the effective thickness. For the device geometry of interest, the effective stiffness formula of a string can be used as seen in Equation 4.6.

$$K_{eff} = \frac{32Ebh^3}{l^3} + \frac{8N}{l} \tag{4.6}$$

where, b is the width of the SiNW and N is the axial force on the SiNW. The axial force is composed of the intrinsic stress as indicated by ε_s in Equation 4.4 and axial stress due to large deformations.

4.3. Fabrication

A novel fabrication method was contrived for the SiNW resonator. The fabrication process is the first of its kind and challenging. Therefore optimization and development is still under study. A more detailed investigation on the fabrication was published by Yıldız [4].

Fabrication is carried out on a 4” SOI wafer with a <100>-oriented and 1.5-µm-thick device Si layer and 2-µm-thick BOX. First, using LPCVD SOI wafer is coated with a 100-nm-thick SiO_2 layer. This layer is then patterned by optical lithography. 2-µm-thick positive AZ92XX photoresist is used to define two-terminal devices with a NW line residing between them. SiNW is later to be formed underneath this mask. Hence, the width of the line (1.2 µm) is crucial for the success of the process. After the mask is defined, exposed SiO_2 is etched in RIE and the hard mask for the subsequent Bosh process is thus formed (Figure 4.5.a). Based on optical lithography this step is where batch compatibility of the whole integration process is introduced and scalability is secured.

Formation of oxide hard mask is followed by the Bosch process in ICP-DRIE to form scalloped walls on trenches underneath the NW line (Figure 4.5.b). 1.5-μm-thick device Si is etched all the way to the BOX layer. Scallop size can be controlled by relative timing of the isotropic etch phase with SF_6 gas. With the specific recipe, scallops are formed to have radii of approximately 200 nm. Under these conditions it takes four etch cycles to reach BOX.

Subsequent wet oxidation step allows consumption of Si on trench walls. As a result of a careful oxide growth, Si column can be separated into Si strings enveloped within SiO_2. The thickness of the grown oxide is crucial as under-oxidation may result in failure of the release of SiNWs, whereas over-oxidation may result in total consumption of the Si wall. To obtain a single SiNW, the hard mask is used as an inhibitor to SiO_2 growth (thus Si consumption) on the upper Si surface and oxidation is carried out until Si wall is consumed almost entirely throughout its width (Figure 4.5.c). The process can also be adjusted such that multiple SiNWs are fabricated along the scallops as shown by Ozsun *et al* [43]. In addition to shaping of SiNWs, grown oxide also serves as a protective layer in subsequent harsh treatments and defines the SiNW-electrode gap. It is this step, where a uniform and submicron SiNW-electrode gap is defined over a span of 50 μm.

Following oxidation, a 1.5-μm-thick Al film is blanket-deposited through sputtering to fill the trenches on both sides of the already oxidized NW line (Figure 4.5.d). Deposition is followed by spin-coating of a 2-μm-thick positive AZ_ECI-type resist (Figure 4.5.e). This process will lead to a self-aligned mask needed for the formation of read-out and actuation electrodes. To form a self-aligned mask, chemical-mechanical polishing (CMP) method is employed. Planarization of the surface is achieved through removing PR from the upper parts until Al layer is exposed (Figure 4.5.f). Direct CMP of Al proves to be a difficult task. Aside from being a relatively hard material, scale differences among Al

portions to be removed play a detrimental role. Hence, the current process based on photoresist removal instead of Al is developed.

Subsequently, Al is wet etched until SiO_2 layer is exposed (Figure 4.5.g). Finally, both SiO_2 coating surrounding the buried Si string cores and BOX layer are etched until SiNWs are released (Figure 4.5.h). Etching is carried out in Al-selective Silox. As a direct result of the oxide protective layer, no short between electrodes and SiNW is of concern. Furthermore, submicron SiNW-electrode gaps can be preserved over large distances.

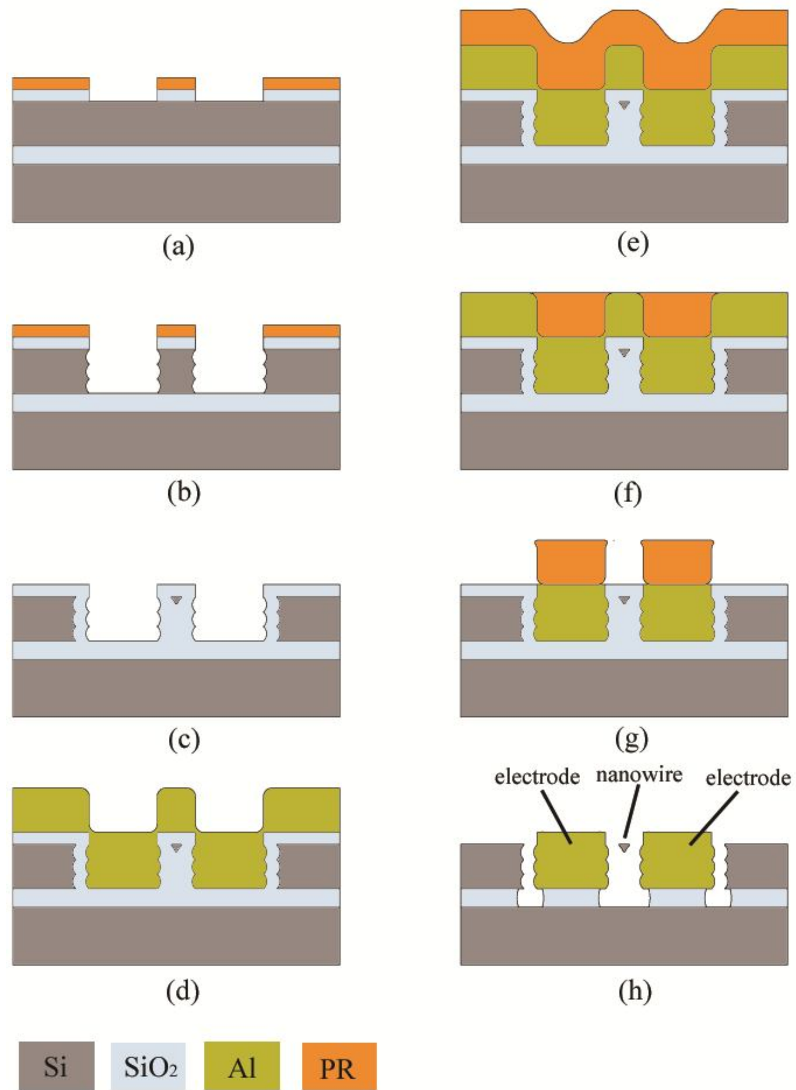

Figure 4.5: Fabrication flow of the device

a) Hard mask definition b) ICP-DRIE c) Oxidation

d) Metal coating e) PR coating f) CMP g) Al etch h) Oxide etch

4.4. Results and Discussion

It is to be noted that in this work relatively long SiNWs (50 μm) are fabricated to achieve resonance frequencies on the order of 1 MHz. Keeping the resonance frequency at that level facilitates addressing of rather complicated issues in actuation and readout. Due to the same reason, the behavior of a single SiNW will be studied instead of an array of SiNWs as previously demonstrated [43]. To achieve higher frequencies and to inquire into SiNW array behavior one can easily adjust layout and process parameters.

This section starts with the characterization of the device as a resonator followed by the demonstration of the switch behavior. Pull-in and pull-off conditions are discussed and the suitability of the device as a high-voltage switch is investigated. Intrinsic stress in Si is computed in both cases. Finally, the results of a three-point bending test are discussed in relation to the clamping quality and the fracture strength of SiNWs.

4.4.1 Resonator Characterization

Subsequent to several experiments which can be seen in Appendix C, several qualified data are obtained. Figure 4.6.a provides frequency sweep data from transmission measurements taken with the setup depicted in Figure 4.3. These direct results do not yield any meaningful peaks as they indicate various interference sources irrespective of the motion of SiNW. However, when the differential signal, *i.e.* the difference from the results obtained with grounded SiNW, is plotted, a clear trend for the motional current is obtained.

Experiments where V_{ac} was kept at 400 mV resulted in excessive noise therefore obstructing observation of any resonance as seen in Appendix C. THRU calibration was carried out but did not improve the quality of measurements. However, when V_{ac} was kept at 40 mV the resonance was visible with a clear trend. Due to the indirect nature of the

measurements the frequency sweep range could not be narrowed during the experiments resulting in fewer data points. The phase difference due to the induced resonance can also be observed as seen in Appendix C. The phase difference agreed with the peaks obtained supporting the idea that the observed peak is a result of resonance. Smaller peaks and pits observed around the main resonance peak are believed to be different resonance modes with smaller induced capacitive differences. The signal is observed to strongly depend on the applied DC bias on SiNW as seen in Figure 4.6.b. The inset shows more clearly the increasing signal, and also a close look reveals the onset of nonlinearity with increasing bias.

The resonance peak is observed at 1.97 MHz. Using Equation 4.4, intrinsic strain and stress can be computed. As a result, a tensile intrinsic stress of 2.8 MPa is found within the SiNW. By fitting Lorenztian curves to the measured data, the quality factor can also be calculated. Excluding the data series in which nonlinear resonance due to the hardening is observed, an average quality factor of 75 is obtained. This rather low quality factor can be attributed to the relatively low intrinsic stress present in SOI device layer.

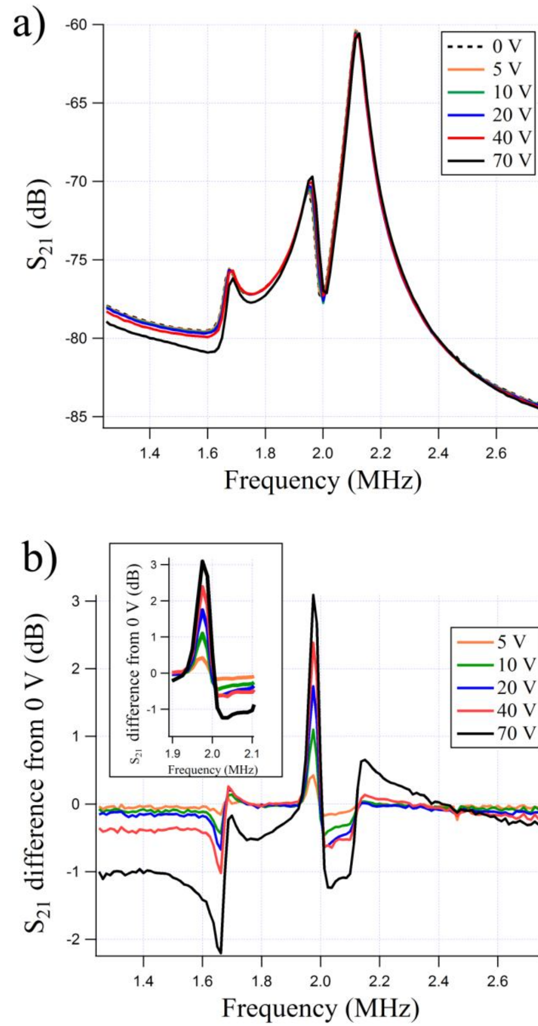

Figure 4.6: a) Direct results obtained from the network analyzer. b) Differential signal readout indicating net motional/dynamic current. Inset provides a close-up view of the obtained peak indicating strong dependence of the obtained signal on SiNW bias.

4.4.2. Switch Characterization

When the current is measured over the ports C and D in Figure 4.4, a clear indication of pull-in of SiNWs is obtained. Graphs of current versus the voltage difference between the electrode and the SiNW are provided in Figure 4.7 and Appendix D. Measurements in the dark indicate a change in current from a few hundred fA to 1 pA resulting in an on/off current gain of 10 (lower curve in Figure 4.7.a). The measured few hundred fA is the minimum measurable current by the SPA. The increase in the current before pull-in is due to the tunneling of electrons. After pull-in occurs, a contact between SiNW and Al electrode is established in the form of a Schottky barrier. Hence, in the presence of incident white light, the magnitude of the current jump at pull-in increases to three orders of magnitude (from 0.1 to 100 pA) (upper curve in Figure4.7.a). The current change was abrupt regardless of the step size as seen in Appendix D. The pull-in was observed optically through a microscope and a specific color change was observed as seen in Figure 4.4 Pull-in is observed at relatively high voltage differences that can be decreased by decreasing the SiNW radius or SiNW-to-electrode gap. Pull-in voltage and magnitude of the current jump remain independent of the voltage sweep parameters such as the utilized step size as seen in Appendix D.

Using Equations 4.5 and 4.6, intrinsic stress within SiNW can be computed once again. For pull-in samples a voltage of 35 V corresponds to an intrinsic stress of 29 MPa. Although this value is ten times higher than the intrinsic stress of 2.8 MPa computed on resonance samples, it is still too low for any practical reason. This deviation is thought to be a result of minor cross-sectional changes encountered over the large span of 50 μm, which is considered in none of the analytical formulations of Equations 4.4, 4.5 and 4.6.
As the voltage difference is decreased after pull-in, SiNW stays attached to the Al electrode until its release takes place at a lower voltage level leading to a hysteretic behavior as

shown in Figure 4.7.b. Prior to the release, the contact area between the SiNW and the Al electrode decreases gradually. Therefore measured current is a few tens of pA when the release occurs. Since the maximum current attained remains below 1 nA, no damage to SiNW or Al electrodes is observed. Hence, the measured pull-in voltage exhibits consistency in consecutive experiment sets.

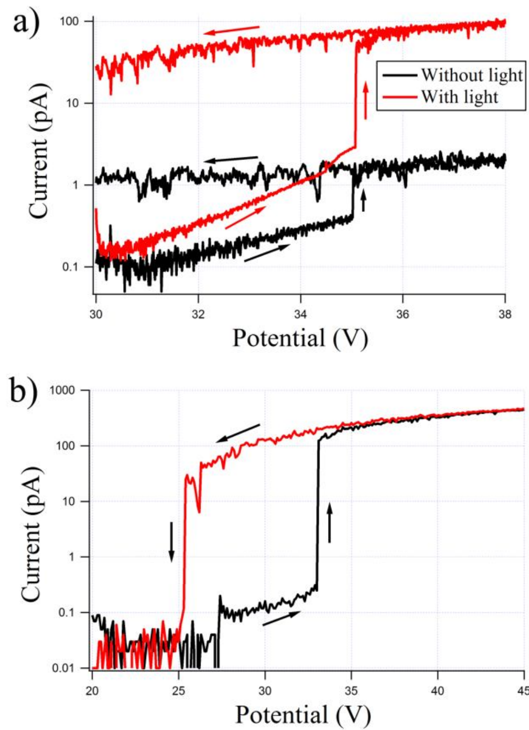

Figure 4.7: a) Effect of incident white light on the magnitude of current jump upon pull-in. b) Hysteretic behavior of the switch.

Although the general process was straightforward without any discrepancies, several experiments resulted in detachments as seen in Appendix D. It is believed that the reason for these discrepancies is the contamination and impurities disturbing the contact between the Al electrode and the SiNW. Overall the pull-in and pull-out phenomena were consistent with a voltage difference less than 500 mV. The difference decreased as the step

size decreased as seen in Appendix D. Device B251 exhibited a 10 V difference in the measured pull-in voltage of different days. The reason for such a difference is believed to be permanent deformation introduced in the first set of experiments.

4.4.3. Three-Point Bending Results

To evaluate the strength of clamping, which plays an important role in both resonance and pull-in behavior, a three-point bending test is conducted within a scanning electron microscope. The experiment provides information on the fracture strength of SiNW in case the failure does not take place at the clamps. A sharp tungsten probe driven by a micro-manipulator (miBot by Imina Technologies) is used for this purpose. Al electrodes are removed by etching to provide space for bending test. With the tungsten tip SiNWs are loaded at their mid-span until fracture. The deformation of SiNWs is observed and measured through scanning electron micrographs. Fracture strength is extracted from these data by large-deformation modeling.

Steps from a sample test are provided in Figure 4.8. Fracture takes place in all tests in the mid-point denoting the high quality of the clamping. An average deflection of 5.9 μm is recorded at fracture. The last micrograph in Figure 4.8 is very close to the onset of fracture. Large-displacement finite element analysis using bulk Si modulus of elasticity and intrinsic stress calculated from the resonator characterization is used to obtain a fracture strength of 14 GPa. The measured fracture strength is close to one tenth of the modulus of elasticity of Si, a good approximation of the theoretical strength [2].

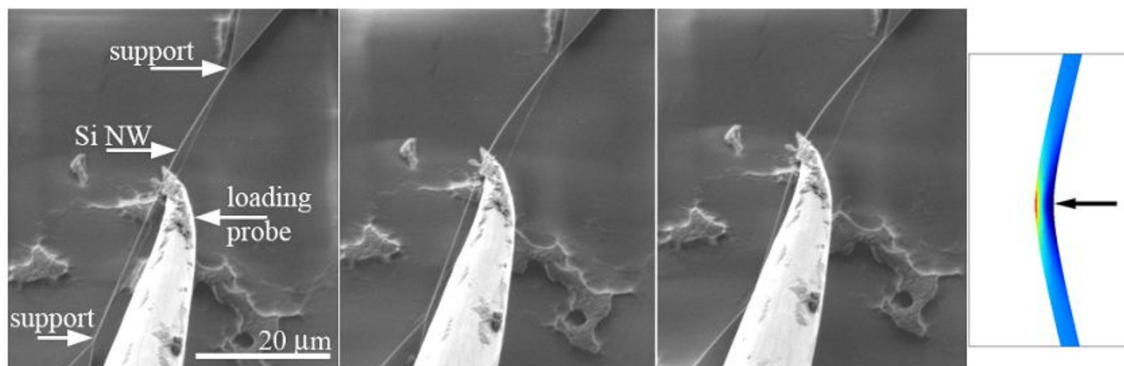

Figure 4.8: Scanning electron micrographs of a loading sequence in three-point bending configuration. In three-point bending samples, Al electrodes are etched deliberately to provide space for probe motion and SiNW bending deflection.

Chapter 5

CONCLUSION

A comprehensive design of a microtensile testing device is demonstrated. Analyzing previous examples in the literature a device, consisting of an electrostatic comb-drive actuator and a differential capacitive load sensor of tri-plate geometry is chosen. The device operates by introducing a uniaxial tensile force to the SiNW sample by the actuator and measuring the sample elongation and force from the load sensor. Failure mechanisms and linearity of the operations for both the actuator and the load sensor is investigated. By defining design limits and considering the failure mechanisms, a MATLAB code is formed to obtain the optimum design geometry of the device. FEA is carried out to simulate the operation of the microtensile testing device. Simulation results suggest that the assumptions taken throughout the design process are adequate and the operation of the device is should be prosperous. A fabrication flow for the device is proposed. Fabrication is devised for each microtensile testing device to be easily individually tested on a probe station. Microloading effect is eliminated by the use of dummy halo masks and ohmic contact is obtained by Cr-Au evaporation.

Alongside the design of microtensile testing device, a fabrication process is proposed for the integration of a single SiNW or an array of SiNWs with microscale metallic electrodes/contacts. The use of optical lithography along with the Bosh process on simple SOI wafers ensures batch compatibility. For the definition of metal electrodes a

unique CMP procedure is developed leading to the formation of self-aligned masking. All processes are CMOS-compatible.

The demonstration of the resulting SiNW-Al electrode pairs as resonators and switches is carried out. All actuation and read-out steps are conducted electrically to highlight the suitability of the proposed device for fully electronic, on-chip solutions. Resonance frequency of 1.97 MHz with a quality factor 75 is measured. Repeatable and hysteretic pull-in and pull-out behavior is found in a range of 30-40 V, which can be further decreased by decreasing SiNW-electrode gap or SiNW radius. Structural integrity of SiNWS is also tested through three-point bending test, where fracture strengths approaching the theoretical strength of the material are observed. No failure at clamping points is encountered.

The length of all SiNW samples is kept at 50 μm leading to slenderness ratios (SiNW length-to-diameter ratio) on the order of 500 and relatively low resonance frequencies. Besides demonstrating the capability of the proposed fabrication technique to yield SiNWs of very high slenderness ratios, another reason behind this choice is the intention to limit resonance frequencies to around 1 MHz. Avoiding higher frequencies help address already complicated issues related to electrostatic actuation and capacitive readout. There is much more room for miniaturization to achieve higher frequencies, which can be realized through SiNW length reduction through optical lithography. Increasing intrinsic stress through doping or oxidation is also found to be a viable option to improve relatively low quality factors. Similarly, an electrode-to-SiNW gap of 900 nm is preserved. Pull-in voltages can further be reduced by reducing either this gap size through the amount of sacrificial oxidation prior to the release step or SiNW diameter. The extension of the work to an array operation instead of a single SiNW is currently under study.

Appendix A

MATLAB CODE OF PARAMETRIC ANALYSIS

```
clc
close all
clear all
%% THESIS CALCULATION
%%SAMPLE VARIABLES
%% d = NW diameter (meter)
%% sigma_fracture = fracture stress (Pa)
%% aspect_ratio = aspect ratio
%% A = NW cross-section area (m^2)
%% E = Elastic modulus  (Pa)
%% k_s = sample stiffness (N/m)
%% F_s = Force on sample (N)
%% F_smax = maximum Force on sample (N)
%% delta_x = length difference of sample (m)
%% epsi = strain of NW

d=75*1e-9;
aspect_ratio=1000;
sigma_fracture=12*1e9;
A=pi*d^2/4;
E=170*1e9;
k_s=A*E/(aspect_ratio*d);
F_smax=sigma_fracture*A;
epsi=0.1;
delta_x= F_smax/k_s;



%%LOAD SENSOR VARIABLES
%% epsi0=permittivity of air
%% h_ls= height of sensor finger (m)
%% w_ls= width of sensor finger (m)
%% l_ls= length of sensor finger (m)
%% N_data= number of data points
%% xls_step= travel length of load sensor in one step (m)
%% xls_max= maximum travel length of load sensor (m)
```

```
%% d1 = first initial gap between sensor
%% d2 = second initial gap between sensor
%% b = ratio between first and second initial gap between sensor
%% N_ls= number of comb fingers/3
%% del_C= generated capacitive difference
%% del_Cmin= minimum capacitive difference
%% A_ls = area of load sensor (m^2)
%% k_ls = load sensor stiffness (N/m)
%% F_lsmax= maximum force on load sensor (N)
%% F_ls= force on load sensor (N)
%% Ve= applied voltage on the load sensor (V)
%% del= ratio between electrostatic force to the restoring force
%% x_star= x/d1
%% x_starmax= xls_max/d1
%% NLD_ls = displacement nonlinearity (%)
%% NLF_ls = force nonlinearity (%)
%% NLD_lsmax = maximum displacement nonlinearity (%)
%% NLF_lsmax = maximum force nonlinearity (%)

epsi0=8.854*1e-12;
h_ls = 7.5*1e-6;
w_ls = 5*1e-6;
l_ls = 400*1e-6;
N_data = 1000;
F_lsmax = F_smax;
d1=3.5*1e-6;
b=5;
x_starmax=0.5;
Ve= 2;
it=1;
N_ls = [0];
k_ls = [0];
A_ls = [0];
NLD_lsmax =[0];
NLF_lsmax =[0];

% for d1=3*1e-6:1e-6:15*1e-6
%     for b=2:1:15
%          for x_starmax=0.1:0.05:0.6
%            for Ve = 1:1:5
d2=b*d1;
xls_max = d1*x_starmax;
k_ls(it) = F_lsmax/xls_max;
xls_step = xls_max/N_data;
del_Cmin = 1*1e-15;
a=2*epsi0*(h_ls*l_ls)*xls_step;
```

```
N_ls(it) = ceil( del_Cmin/(1/(d1^2-xls_step^2)-1/(d2^2-xls_step^2))/a );
A_ls(it) = N_ls(it)*(d1+d2+3*w_ls)*l_ls;



x=0:xls_step:xls_max;
del_C = ceil( del_Cmin./(1./(d1.^2-xls_step^2)-1./(d2.^2-xls_step^2))/a
)*2*epsi0*(h_ls*l_ls)*x.*(1./(d1.^2-x.^2)-1./(d2.^2-x.^2));
figure(1)
plot(x,del_C),xlabel('x m'),ylabel('Capacitance difference F'); hold on;
pause(0.5)
%%LOAD SENSOR LINEARITY ANALYSIS
figure(2)
plot(x,abs(del_C-(ceil( del_Cmin./(1./(d1.^2-xls_step^2)-1./(d2.^2-
xls_step^2))/a )*2*epsi0*(h_ls*l_ls)*xls_max.*(1./(d1.^2-xls_max.^2)-
1./(d2.^2-xls_max.^2))/xls_max*x))/del_Cmin),xlabel('x
m'),ylabel('Capacitance difference from linearity fF'); hold on;
pause(0.5)
%%LOAD SENSOR STABILITY ANALYSIS


del = 2*N_ls(it)*epsi0*(h_ls*l_ls)*Ve^2/(k_ls(it)*d1^3);


figure(3),xlabel('x/d1'),ylabel('ma/(kls*d1)');hold on;

    x_star=0:1e-2:0.7; %%x/d1
    ind=length(x_star);
    f = x_star.*(1-del*(1./(b^3*(1-x_star.^2/b^2).^2)+(1./(1-
x_star.^2).^2)));
    peak=max(f);
    for i=1:ind
        if f(i)==peak
        peakx=i
        end
    end

    x_starp1=zeros(1,peakx)
    fp1=zeros(1,peakx)

    for j=1:peakx
    x_starp1(j)=  x_star(j);
    fp1(j)=f(j)
    end
    plot(x_starp1,fp1); hold on;
```

```
    x_starp2=zeros(1,ind-peakx)
    fp2=zeros(1,ind-peakx)
    g=1;
    for k=peakx:ind
    x_starp2(g)=  x_star(k);
    fp2(g)=f(k)

    g=g+1;

    end
     plot(x_starp2,fp2,'r.-')
      pause(0.5)
     %%LOAD SENSOR LINEARITY ANALYSIS
    figure (4),xlabel('x/d1'),ylabel('Nonlinearity of force and
displacement %)'),legend('Nonlinearity of displacement','Nonlinearity of
force');hold on;
    x_star=0:1e-2:x_starmax;
    NLD_ls = (x_star/x_starmax).*((1./(1-x_star.^2)-1./(b^2-
x_star.^2))/(1/(1-(x_starmax)^2)-1/(b^2-(x_starmax)^2))-1);
    NLF_ls = (x_star/x_starmax).*((1./(1-x_star.^2)-1./(b^2-
x_star.^2))/(1/(1-(x_starmax)^2)-1/(b^2-(x_starmax)^2))-(1-del*(b./(b^2-
x_star.^2).^2+1./(1^2-x_star.^2).^2))*1./(1-del*((b./(b^2-
x_starmax.^2).^2+1./(1^2-x_starmax.^2)^2))));
    plot(x_star,abs(NLD_ls*100),'r.-');hold on;
    NLD_lsmax(it)=max(abs(NLD_ls));
    plot(x_star,abs(NLF_ls*100));hold on;
    NLF_lsmax(it)=max(abs(NLF_ls));
     it=it+1;
     pause(0.5)
%      end
%      end
%      end
% end
clc




%%LOAD SENSOR SPRING VARIABLES
%%  k_ls = load sensor stiffness
%% h_kls= height of spring finger (m)
%% w_kls= width of spring finger (m)
%% l_kls= length of spring finger (m)
%% N_kls= number of springs
%% k_kls= stiffness of spring
%% k_kls_z= stiffness of spring along z
%% k_kls_y= stiffness of spring along y
```

```
h_kls= 7*1e-6;
w_kls=4*1e-6;
l_kls=205*1e-6;
k_kls = E*h_kls*w_kls^3/l_kls^3;
k_kls_z= E*w_kls*h_kls^3/l_kls^3;

N_kls=ceil(k_ls/k_kls);


%%Final spring constant

k_ls=N_kls*k_kls;

%%%%%%%%%%%%%%%%%%%%%%%


%%ACTUATOR SPRING VARIABLES
%%  k_ac = actuator stiffness
%% h_kac= height of spring finger (m)
%% w_kac= width of spring finger (m)
%% l_kac= length of spring finger (m)
%% N_kac= number of springs
%% k_kac= stiffness of spring
%% k_kac_z= stiffness of spring along z
%% k_kac_y= stiffness of spring along y

h_kac= 7*1e-6;
w_kac=4*1e-6;
l_kac=600*1e-6;
k_kac = E*h_kac*w_kac^3/l_kac^3;
k_kac_z= E*w_kac*h_kac^3/l_kac^3;
N_kac=4;
k_ac=N_kac*k_kac;
k_ac_y=N_kac*4*E*w_kac*h_kac/l_kac;
k_ac_z=N_kac*k_kac_z;


%%ACTUATOR VARIABLES
%% epsi0=permittivity of air
%% h= height of actuator finger (m)
%% w= width of actuator finger (m)
%% t= zero voltage overlap of actuator finger (m)
%% gx= gap distances of actuator fingers in x-direction (m)
%% gy= gap distances of actuator fingers in y-direction (m)
%% V= applied voltage (V)
```

```
%% Vmax= maximum applied voltage (V)
%% xac_max= maximum displacement of actuator finger (m)
%% xac= displacement of actuator finger (m)
%% F_es= generated electrostatic force (N)
%% F_esmax= generated maximum electrostatic force (N)
%% F_ac= force at the tip of actuator (N)
%% N_ac= number of comb fingers
%% A_ac= area of actuator
%% k_ac = actuator stiffness (N/m)

h = 7*1e-6;
w = 5*1e-6;
t = 5*1e-6;
gx = 1.5*1e-5;
gy = 3*1e-6;
Vmax = 50;
N_ac=[0];
A_ac=[0];
fin_sol=[0];
ir=1;

% for gx=1*1e-5:5e-6:4*1e-5
%     for gy=3*1e-6:1e-6:10*1e-6
%         for t=3*1e-6:1e-6:10*1e-6
    xac_max = delta_x + xls_max;
 while gx < xac_max
     gx=gx+1e-5;
 end

F_esmax = F_smax*(k_ls*k_s+k_ac*(k_ls+1))/k_ls/k_s;
N_ac(ir) = ceil(F_esmax/(epsi0*h*(w/(gx-xac_max)^2+1/gy)*Vmax^2));
A_ac(ir) = (gx+t+xac_max)*(gy+t)*N_ac(ir);

%%ACTUATOR STABILITY ANALYSIS


sol_1=  1/6*(-108*w*gy*gx+12*(96*w^3*gy^3+81*w^2*gy^2*gx^2)^(1/2))^(1/3)-
4*w*gy/(-108*w*gy*gx+12*(96*w^3*gy^3+81*w^2*gy^2*gx^2)^(1/2))^(1/3)+gx;
sol_2= -1/12*(-
108*w*gy*gx+12*(96*w^3*gy^3+81*w^2*gy^2*gx^2)^(1/2))^(1/3)+2*w*gy/(-
108*w*gy*gx+12*(96*w^3*gy^3+81*w^2*gy^2*gx^2)^(1/2))^(1/3)+gx+1/2*i*3^(1/
2)*(1/6*(-
108*w*gy*gx+12*(96*w^3*gy^3+81*w^2*gy^2*gx^2)^(1/2))^(1/3)+4*w*gy/(-
108*w*gy*gx+12*(96*w^3*gy^3+81*w^2*gy^2*gx^2)^(1/2))^(1/3));
sol_3= -1/12*(-
108*w*gy*gx+12*(96*w^3*gy^3+81*w^2*gy^2*gx^2)^(1/2))^(1/3)+2*w*gy/(-
108*w*gy*gx+12*(96*w^3*gy^3+81*w^2*gy^2*gx^2)^(1/2))^(1/3)+gx-
```

```
1/2*i*3^(1/2)*(1/6*(-
108*w*gy*gx+12*(96*w^3*gy^3+81*w^2*gy^2*gx^2)^(1/2))^(1/3)+4*w*gy/(-
108*w*gy*gx+12*(96*w^3*gy^3+81*w^2*gy^2*gx^2)^(1/2))^(1/3));

Soln=[sol_1,sol_2,sol_3];
Soln=sort(Soln);

if min(Soln)>0
   fin_sol(ir)=min(Soln);
end

if min(Soln)<0
if Soln(1)<0
     fin_sol(ir)=Soln(2);
elseif Soln(2)<0
    fin_sol(ir)=Soln(3);
end
end

if xac_max>fin_sol(ir)
    pull_in=fin_sol(ir)
end

%%ACTUATOR LATERAL STABILITY ANALYSIS

Cy_to_Cx=((t+xac_max)/gy)/(w/(gx-xac_max));
V_pullin_y = (k_ac_y*gy^3/(2*epsi0*h_kac*(xac_max+t)))^.5;
if Vmax>V_pullin_y
    lateral_pull_in=V_pullin_y
end

%%ACTUATOR IN-PLANE STABILITY ANALYSIS


% V_pullin = (8*k_ac_z*(3*1e-6)^3/(27*epsi0*A_ac/2))
 ir=ir+1;
%          end
%      end
% end
```

Appendix B

MATLAB DESIGN CODE

```
clc
close all
clear all
%% THESIS CALCULATION
%%SAMPLE VARIABLES
%% d = NW diameter (meter)
%% sigma_fracture = fracture stress (Pa)
%% aspect_ratio = aspect ratio
%% A = NW cross-section area (m^2)
%% E = Elastic modulus  (Pa)
%% k_s = sample stiffness (N/m)
%% F_s = Force on sample (N)
%% F_smax = maximum Force on sample (N)
%% delta_x = length difference of sample (m)
%% epsi = strain of NW

d=75*1e-9;
aspect_ratio=400;
sigma_fracture=12*1e9;
A=pi*d^2/4;
E=170*1e9;
k_s=A*E/(aspect_ratio*d);
F_smax=sigma_fracture*A;
epsi=0.1;
delta_x= F_smax/k_s;



%%LOAD SENSOR VARIABLES
%% epsi0=permittivity of air
%% h_ls= height of sensor finger (m)
%% w_ls= width of sensor finger (m)
%% l_ls= length of sensor finger (m)
%% N_data= number of data points
%% xls_step= travel length of load sensor in one step (m)
%% xls_max= maximum travel length of load sensor (m)
%% d1 = first initial gap between sensor
%% d2 = second initial gap between sensor
```

```
%% b = ratio between first and second initial gap between sensor
%% N_ls= number of comb fingers/3
%% del_C= generated capacitive difference
%% del_Cmin= minimum capacitive difference
%% tot_C= total capacitive
%% A_ls = area of load sensor (m^2)
%% k_ls = load sensor stiffness (N/m)
%% F_lsmax= maximum force on load sensor (N)
%% F_ls= force on load sensor (N)
%% Ve= applied voltage on the load sensor (V)
%% del= ratio between electrostatic force to the restoring force
%% x_star= x/d1
%% x_starmax= xls_max/d1
%% NLD_ls = displacement nonlinearity (%)
%% NLF_ls = force nonlinearity (%)
%% NLD_lsmax = maximum displacement nonlinearity (%)
%% NLF_lsmax = maximum force nonlinearity (%)

epsi0=8.854*1e-12;
h_ls = 50*1e-6;
w_ls = 5*1e-6;
l_ls = 400*1e-6;
N_data = 1000;
F_lsmax = F_smax;
d1=1.5*1e-6;
b=10;
k_ls = 107;
Ve= 2;
it=1;
N_ls = [0];
A_ls = [0];
NLD_lsmax =[0];
NLF_lsmax =[0];

%fid = fopen('load sensor result.html', 'wt');
%fprintf(fid, 'Applicable parameter values for load sensor\n\n' );
%fprintf(fid, 'h_ls\t  w_ls\t    l_ls\tN_data\td1\t  d2\t
k_ls\tVe\tN_ls\t  A_ls\t    NLF_lsmax \n' );

d1val = [0];
d2val = [0];
h_lsval = [0];
w_lsval = [0];
l_lsval = [0];
N_dataval = [0];
k_lsval = [0];
Veval = [0];
```

```
Vout = [0];


% for h_ls = 10*1e-6:10e-6:50*1e-6
    for w_ls = 5*1e-6:1e-6:10*1e-6
%         for l_ls = 200*1e-6:50*1e-6:400*1e-6
%             for N_data = 1000:1000:5000
for d1=1.5*1e-6:0.25*1e-6:4.5*1e-6
    for b=5:1:10
        for k_ls = 100: 1 : 200
%             for Ve = 2:1:5

                d2=b*d1;
                xls_max = F_lsmax/k_ls;
                x_starmax = xls_max/d1;
                xls_step = xls_max/N_data;
                del_Cmin = 1*1e-15;
                a=2*epsi0*(h_ls*l_ls)*xls_step;

                N_ls(it) = ceil( del_Cmin/(1/(d1^2-xls_step^2)-1/(d2^2-
xls_step^2))/a );
                A_ls(it) = N_ls(it)*(d1+d2+3*w_ls)*l_ls;


                x=0:xls_step:xls_max;
                del_C = ceil( del_Cmin./(1./(d1.^2-xls_step^2)-1./(d2.^2-
xls_step^2))/a )*2*epsi0*(h_ls*l_ls)*x.*(1./(d1.^2-x.^2)-1./(d2.^2-
x.^2));

                %%LOAD SENSOR FRINGING EFFECT ANALYSIS
                if x_starmax > 0.5
                    break
                end

                %%LOAD SENSOR SIMPLICITY ANALYSIS
                if N_ls(it) > 20
                    break
                end


                %%LOAD SENSOR STABILITY ANALYSIS


                del = 2*N_ls(it)*epsi0*(h_ls*l_ls)*Ve^2/(k_ls*d1^3);
```

```
                x_star=0:1e-2:1; %%x/d1
                ind=length(x_star);
                f = x_star.*(1-del*(1./(b^3*(1-x_star.^2/b^2).^2)+(1./(1-
x_star.^2).^2)));
                peak=max(f);
                for i=1:ind
                    if f(i)==peak
                        peakx=i
                    end
                end


                if peakx/100 < x_starmax
                    break
                end

                %%LOAD SENSOR LINEARITY ANALYSIS
                x_star=0:1e-2:x_starmax;

                NLD_ls = (x_star/x_starmax).*((1./(1-x_star.^2)-1./(b^2-
x_star.^2))/(1/(1-(x_starmax)^2)-1/(b^2-(x_starmax)^2))-1);
                NLF_ls = (x_star/x_starmax).*((1./(1-x_star.^2)-1./(b^2-
x_star.^2))/(1/(1-(x_starmax)^2)-1/(b^2-(x_starmax)^2))-(1-del*(b./(b^2-
x_star.^2).^2+1./(1^2-x_star.^2).^2))*1./(1-del*((b./(b^2-
x_starmax.^2).^2+1./(1^2-x_starmax.^2)^2))));
                NLD_lsmax(it)=max(abs(NLD_ls));
                NLF_lsmax(it)=max(abs(NLF_ls));

                if NLF_lsmax(it) > 0.05
                    break
                end

                %%LOAD SENSOR FINGER STABILITY ANALYSIS
                safety = 3;
                fingerdisp=safety*3*l_ls^5*epsi0*Ve^2*(d2/(d2^2-
xls_max^2)^2+d1/(d1^2-xls_max^2)^2)*xls_max/(E*w_ls*h_ls^2);

                if fingerdisp >(d1-xls_max)
                    break
                end

                %%OUTPUT VOLTAGE ANALYSIS

                tot_C(it) =ceil( del_Cmin./(1./(d1.^2-xls_step^2)-
1./(d2.^2-xls_step^2))/a )*epsi0*l_ls*h_ls*(1/d1+1/d2)*2 ;
```

```
                Vout(it)= max(del_C)/tot_C(it)*Ve;

                if Vout(it) <0.01
                    break
                end

                %fprintf(fid, '%6.2e %6.2e %6.2e %6.2e %6.2e %6.2e %6.2e
%6.2e %6.2e %6.2e %6.2e\n',h_ls, w_ls, l_ls, N_data, d1, d2, k_ls,
Vout(it), N_ls(it), A_ls(it)*1e6, NLF_lsmax(it)*100);

                d1val(it) = d1;
                d2val(it) = d2;
                h_lsval(it) = h_ls;
                w_lsval(it) = w_ls;
                l_lsval(it) = l_ls;
                N_dataval(it) = N_data;
                k_lsval(it) = k_ls;
                Veval(it) = Ve;


                it=it+1;

            end
        end
    end
end
%             end
%         end
%     end
% end

printTable(d,h_lsval,w_lsval,l_lsval,N_dataval,d1val,d2val,k_lsval,Veval,
N_ls,A_ls,NLF_lsmax);
%fclose(fid)
clc




%%LOAD SENSOR SPRING VARIABLES
%%  k_ls = load sensor stiffness
%% h_kls= height of spring finger (m)
%% w_kls= width of spring finger (m)
%% l_kls= length of spring finger (m)
%% N_kls= number of springs
%% k_kls= stiffness of spring
```

```
%% k_kls_z= stiffness of spring along z
%% k_kls_y= stiffness of spring along y

% h_kls= 7.5*1e-6;
% w_kls=4*1e-6;
% l_kls=200*1e-6;
% k_kls = E*h_kls*w_kls^3/l_kls^3;
% k_kls_z= E*w_kls*h_kls^3/l_kls^3;

% N_kls=ceil(k_ls/k_kls)


%%Final spring constant

% k_ls=N_kls*k_kls

%%%%%%%%%%%%%%%%%%%%%%%


%%ACTUATOR SPRING VARIABLES
%%  k_ac = actuator stiffness
%% h_kac= height of spring finger (m)
%% w_kac= width of spring finger (m)
%% l_kac= length of spring finger (m)
%% N_kac= number of springs
%% k_kac= stiffness of spring
%% k_kac_z= stiffness of spring along z
%% k_kac_y= stiffness of spring along y

h_kac= 50*1e-6;
w_kac=3*1e-6;
l_kac1=600*1e-6;
l_kac2=475*1e-6;
k_kac = 2*E*h_kac*w_kac^3/(l_kac1^3+l_kac2^3);
k_kac_z= 2*E*w_kac*h_kac^3/(l_kac1^3+l_kac2^3);
N_kac=2;
k_ac=N_kac*k_kac;
k_ac_y=N_kac*4*E*w_kac*h_kac/(l_kac1+l_kac2);
k_ac_z=N_kac*k_kac_z;


%%ACTUATOR VARIABLES
%% epsi0=permittivity of air
%% h= height of actuator finger (m)
%% w= width of actuator finger (m)
%% t= zero voltage overlap of actuator finger (m)
```

```
%% gx= gap distances of actuator fingers in x-direction (m)
%% gy= gap distances of actuator fingers in y-direction (m)
%% V= applied voltage (V)
%% Vmax= maximum applied voltage (V)
%% xac_max= maximum displacement of actuator finger (m)
%% xac= displacement of actuator finger (m)
%% F_es= generated electrostatic force (N)
%% F_esmax= generated maximum electrostatic force (N)
%% F_ac= force at the tip of actuator (N)
%% N_ac= number of comb fingers
%% A_ac= area of actuator
%% k_ac = actuator stiffness (N/m)

h = 50*1e-6;
w = 2.5*1e-6;
t = 5*1e-6;
gx = 50*1e-6;
gy = 1.5*1e-6;
Vmax = 50;
N_ac=[0];
A_ac=[0];
fin_sol=[0];
ir=1;
wval = [0];
gxval = [0];
gyval = [0];
tval = [0];
Vpull_in = [0];

for w=2.5*1e-6:0.5e-6:15*1e-5
    for gx=8*1e-6:0.5e-6:7*1e-5
        for gy=1.5*1e-6:0.5e-6:10*1e-6
            for t=1*1e-6:1e-6:10*1e-6


                xac_max = delta_x + xls_max;

                if t+xac_max>gx
                    break
                end

                while gx < xac_max
                    gx=gx+1e-6;
                end

                k_eq= (k_ls*k_s+k_ac*k_ls+k_ac)/(k_ls+1);
```

```
                F_esmax = F_smax*(k_ls*k_s+k_ac*(k_ls+1))/k_ls/k_s;
                N_ac(ir) = ceil(F_esmax/(epsi0*h*(w/(gx-
xac_max)^2+1/gy)*Vmax^2));
                A_ac(ir) = (2*gx-t)*(gy+2*w)*N_ac(ir);

                %%ACTUATOR SIMPLICITY ANALYSIS
                if N_ac(ir) > 1000
                    break
                end


                %%ACTUATOR STABILITY ANALYSIS


                sol_1=
1/3*(27*w*gy+3*(3*w^3*gy^3+81*w^2*gy^2)^(1/2))^(1/3)-
w*gy/(27*w*gy+3*(3*w^3*gy^3+81*w^2*gy^2)^(1/2))^(1/3)+gx;
                sol_2=  -
1/6*(27*w*gy+3*(3*w^3*gy^3+81*w^2*gy^2)^(1/2))^(1/3)+1/2*w*gy/(27*w*gy+3*
(3*w^3*gy^3+81*w^2*gy^2)^(1/2))^(1/3)+gx+1/2*i*3^(1/2)*(1/3*(27*w*gy+3*(3
*w^3*gy^3+81*w^2*gy^2)^(1/2))^(1/3)+w*gy/(27*w*gy+3*(3*w^3*gy^3+81*w^2*gy
^2)^(1/2))^(1/3));
                sol_3=  -
1/6*(27*w*gy+3*(3*w^3*gy^3+81*w^2*gy^2)^(1/2))^(1/3)+1/2*w*gy/(27*w*gy+3*
(3*w^3*gy^3+81*w^2*gy^2)^(1/2))^(1/3)+gx-
1/2*i*3^(1/2)*(1/3*(27*w*gy+3*(3*w^3*gy^3+81*w^2*gy^2)^(1/2))^(1/3)+w*gy/
(27*w*gy+3*(3*w^3*gy^3+81*w^2*gy^2)^(1/2))^(1/3));

                Soln=[sol_1,sol_2,sol_3];
                Soln=sort(Soln);

                if min(Soln)>=0
                    fin_sol(ir)=min(Soln);
                end

                if min(Soln)<0
                    if Soln(1)<0
                        fin_sol(ir)=Soln(2);
                    elseif Soln(2)<0
                        fin_sol(ir)=Soln(3);
                    end
                end

                Vpull_in(ir) = (fin_sol(ir)*k_eq/(epsi0*h*(w/(gx-
fin_sol(ir))^2+1/gy)*N_ac(ir))).^0.5;
```

```
                if Vpull_in(ir) - Vmax < 1

                    break
                end

                if xac_max>fin_sol(ir)
                    pull_in=fin_sol(ir)
                    break
                end

                %%ACTUATOR LATERAL STABILITY ANALYSIS

                safety = 4;
                V_pullin_y =
safety*(k_ac_y*gy^3/(2*epsi0*h_kac*(xac_max+t)))^.5;
                if Vmax>V_pullin_y
                    lateral_pull_in=V_pullin_y
                    break
                end

                %%ACTUATOR LINEARITY ANALYSIS

                if  (t+xac_max)/gy*(gx-xac_max)/w<40
                    break
                end

                %%ACTUATOR IN-PLANE STABILITY ANALYSIS


                % V_pullin = (8*k_ac_z*(3*1e-6)^3/(27*epsi0*A_ac/2))

                gxval(ir) = gx;
                gyval(ir) = gy;
                tval(ir) = t;
                wval(ir) = w;

                ir=ir+1;
            end
        end
    end
end
printTable_ac(d,h,wval,tval,gxval,gyval,k_ac,Vmax,N_ac,A_ac);
```

Appendix C

RESONANCE CHARACTERIZATION EXPERIMENTS

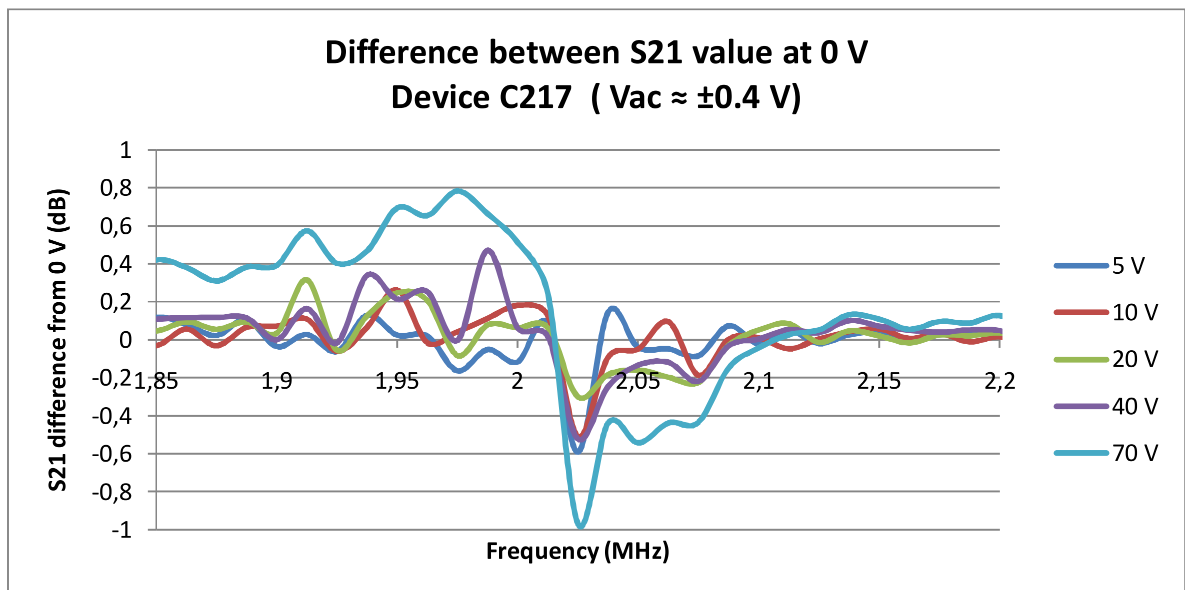

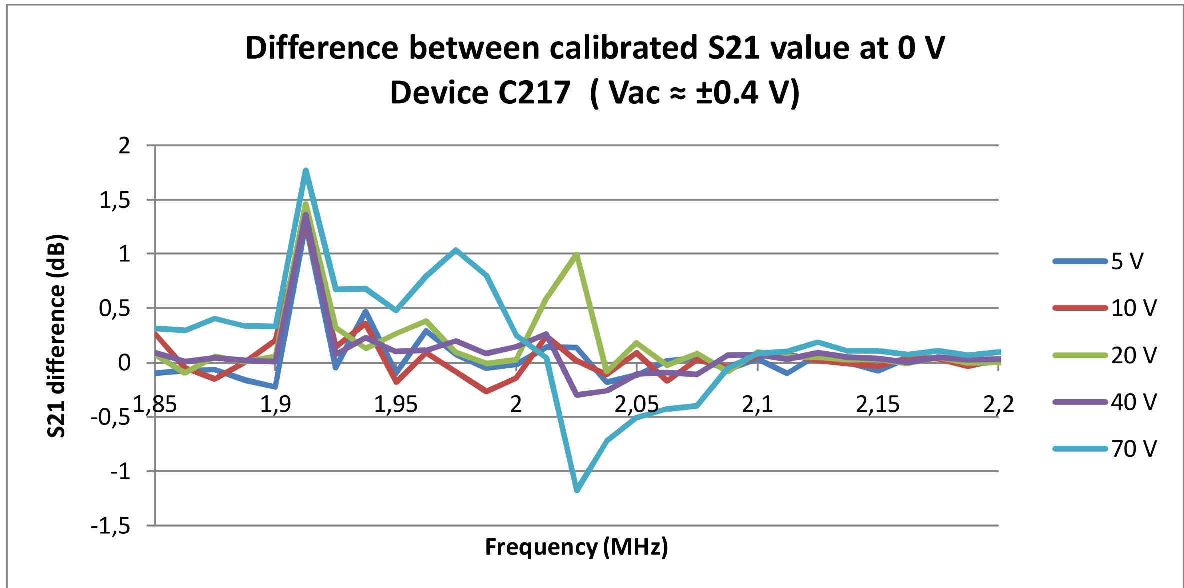
Difference between calibrated S21 value at 0 V
Device C217 (Vac ≈ ±0.4 V)
S21 difference (dB)
2
1,5
1
0,5
0
-0,5
-1
-1,5
1,85
1,9
1,95
2
2,05
2,1
2,15
2,2
Frequency (MHz)
5 V
10 V
20 V
40 V
70 V

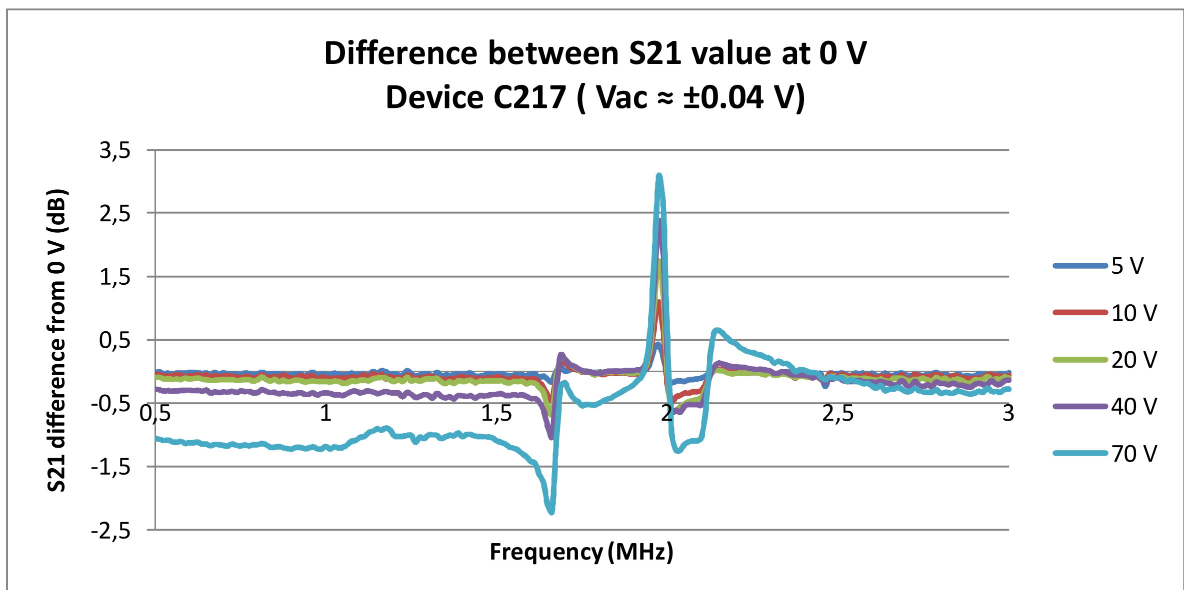
Difference between S21 value at 0 V
Device C217 (Vac ≈ ±0.04 V)
S21 difference from 0 V (dB)
3,5
2,5
1,5
0,5
-0,5
-1,5
-2,5
0,5
1
1,5
2
2,5
3
Frequency (MHz)
5 V
10 V
20 V
40 V
70 V

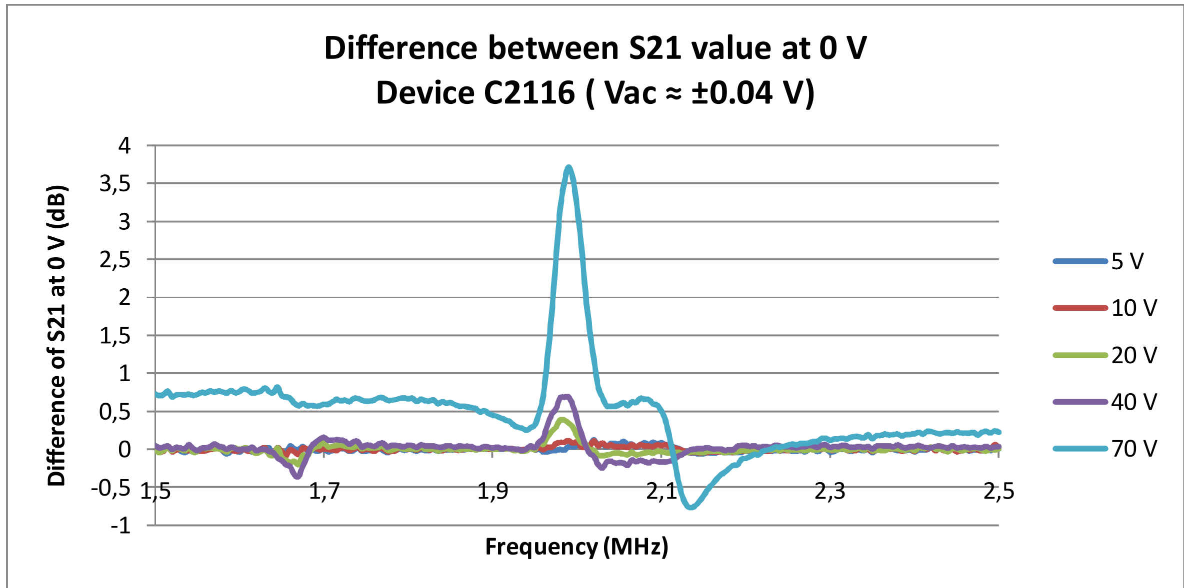
Difference between S21 value at 0 V
Device C2116 (Vac ≈ ±0.04 V)
Difference of S21 at 0 V (dB)
4
3,5
3
2,5
2
1,5
1
0,5
0
-0,5
-1
1,5
1,7
1,9
2,1
2,3
2,5
Frequency (MHz)
5 V
10 V
20 V
40 V
70 V

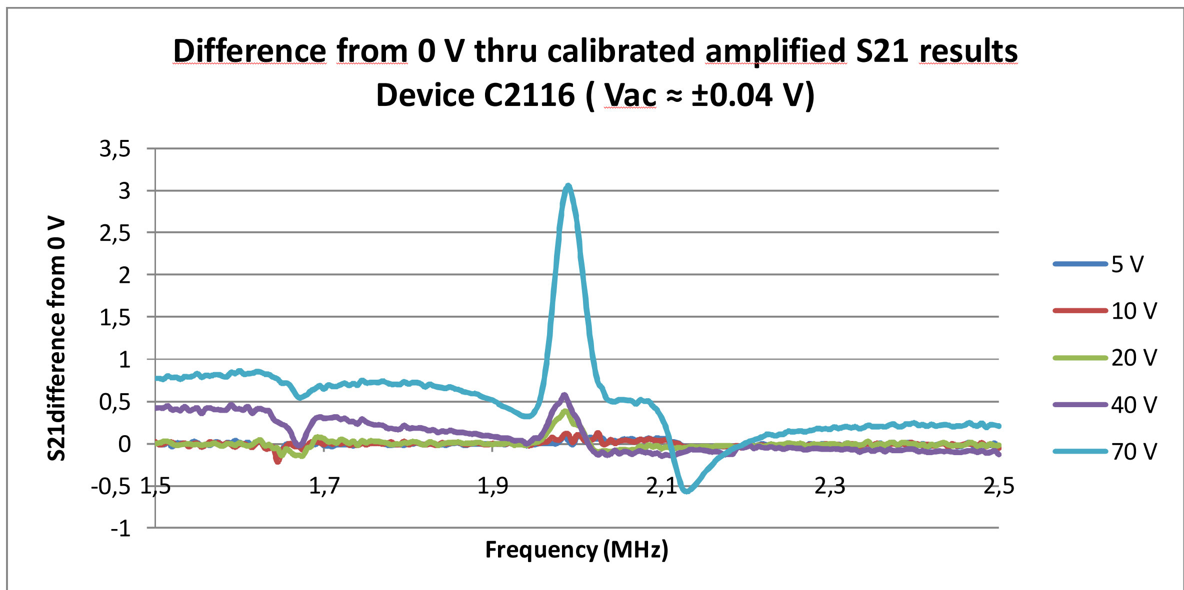
Difference from 0 V thru calibrated amplified S21 results
Device C2116 (Vac ≈ ±0.04 V)
S21difference from 0 V
3,5
3
2,5
2
1,5
1
0,5
0
-0,5
-1
1,5
1,7
1,9
2,1
2,3
2,5
Frequency (MHz)
5 V
10 V
20 V
40 V
70 V

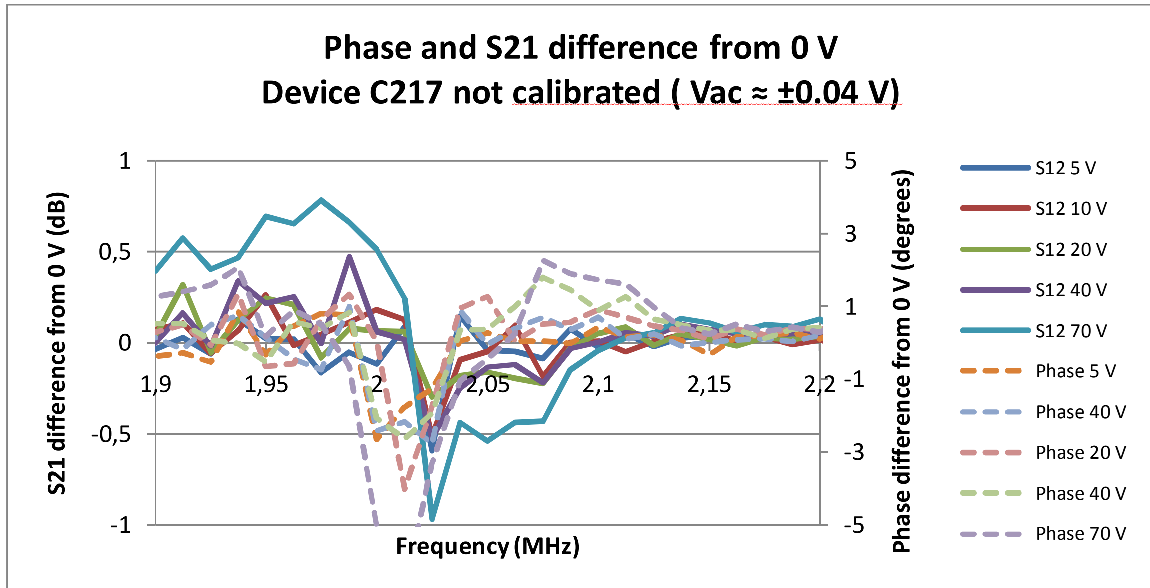
Phase and S21 difference from 0 V
Device C217 not calibrated (Vac ≈ ±0.04 V)
S21 difference from 0 V (dB)
Phase difference from 0 V (degrees)
Frequency (MHz)
1
0,5
0
-0,5
-1
5
3
1
-1
-3
-5
1,9
1,95
2
2,05
2,1
2,15
2,2
S12 5 V
S12 10 V
S12 20 V
S12 40 V
S12 70 V
Phase 5 V
Phase 40 V
Phase 20 V
Phase 40 V
Phase 70 V

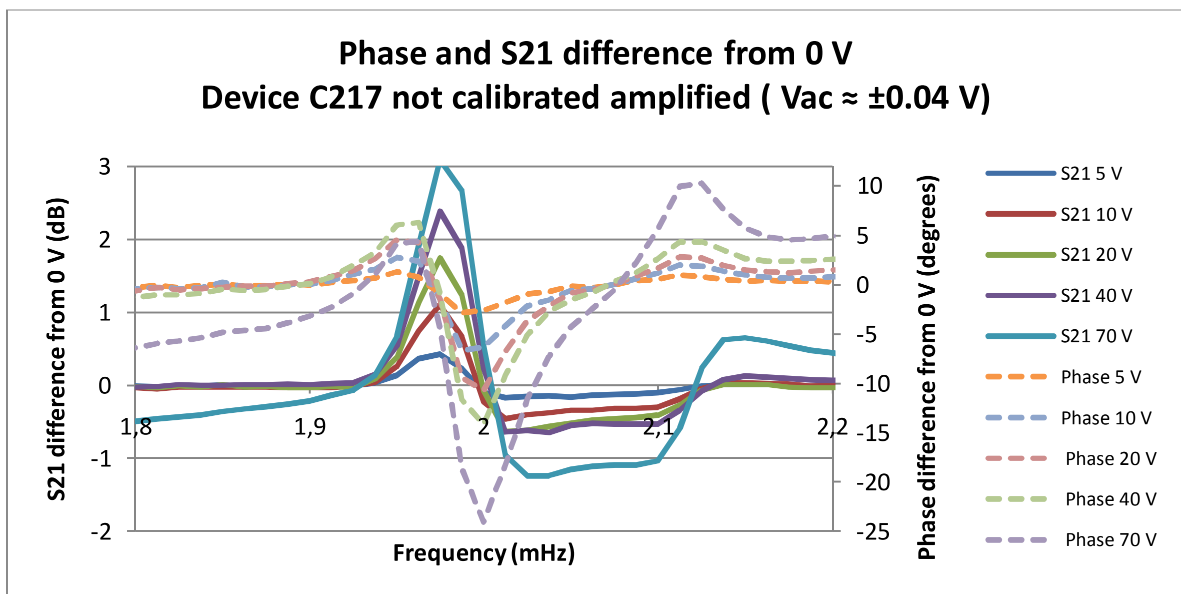
Phase and S21 difference from 0 V
Device C217 not calibrated amplified (Vac ≈ ±0.04 V)
S21 difference from 0 V (dB)
Phase difference from 0 V (degrees)
Frequency (mHz)
3
2
1
0
-1
-2
10
5
0
-5
-10
-15
-20
-25
1,8
1,9
2
2,1
2,2
S21 5 V
S21 10 V
S21 20 V
S21 40 V
S21 70 V
Phase 5 V
Phase 10 V
Phase 20 V
Phase 40 V
Phase 70 V

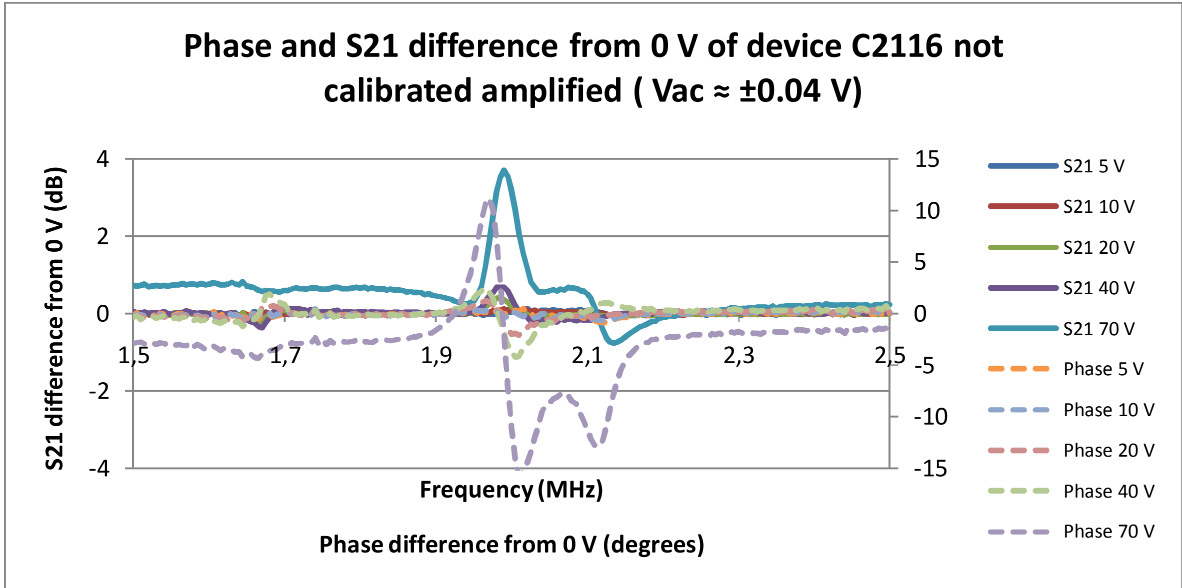
Phase and S21 difference from 0 V of device C2116 not calibrated amplified (Vac ≈ ±0.04 V)
S21 difference from 0 V (dB)
4
2
0
-2
-4
15
10
5
0
-5
-10
-15
1,5
1,7
1,9
2,1
2,3
2,5
Frequency (MHz)
Phase difference from 0 V (degrees)
S21 5 V
S21 10 V
S21 20 V
S21 40 V
S21 70 V
Phase 5 V
Phase 10 V
Phase 20 V
Phase 40 V
Phase 70 V

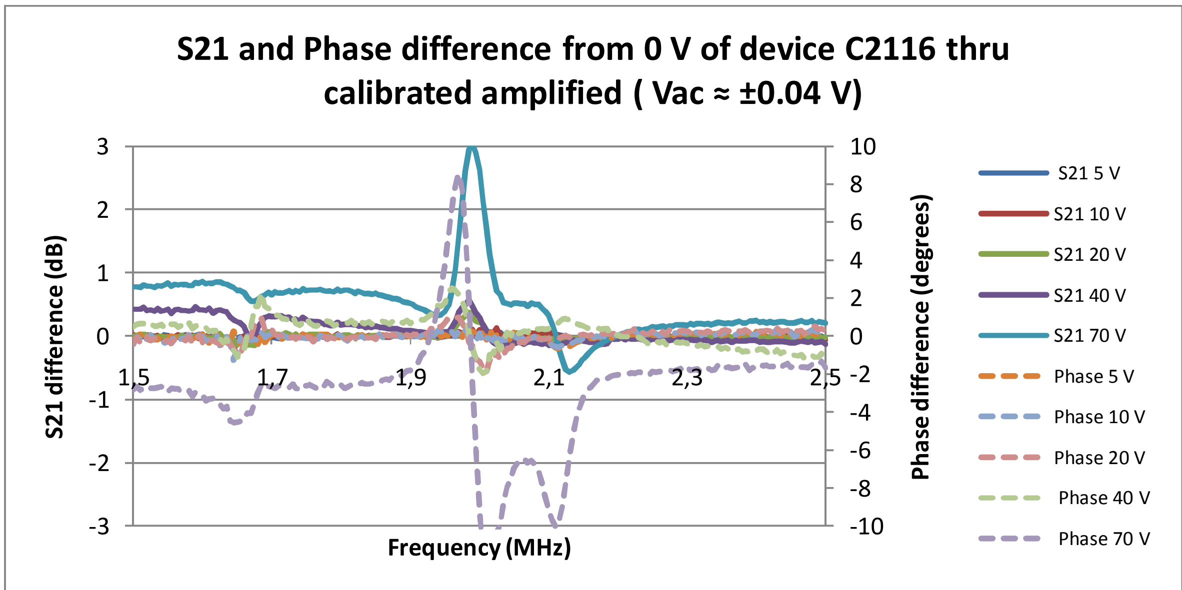
S21 and Phase difference from 0 V of device C2116 thru calibrated amplified (Vac ≈ ±0.04 V)
S21 difference (dB)
3
2
1
0
-1
-2
-3
10
8
6
4
2
0
-2
-4
-6
-8
-10
1,5
1,7
1,9
2,1
2,3
2,5
Frequency (MHz)
Phase difference (degrees)
S21 5 V
S21 10 V
S21 20 V
S21 40 V
S21 70 V
Phase 5 V
Phase 10 V
Phase 20 V
Phase 40 V
Phase 70 V

Appendix D

SWITCH CHARACTERIZATION EXPERIMENTS

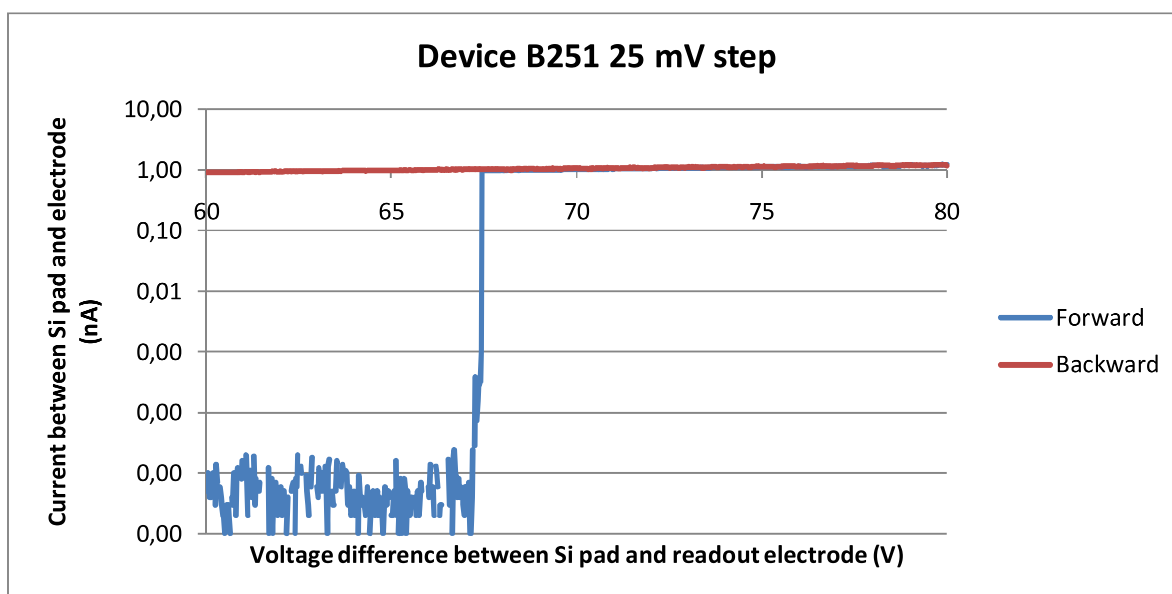

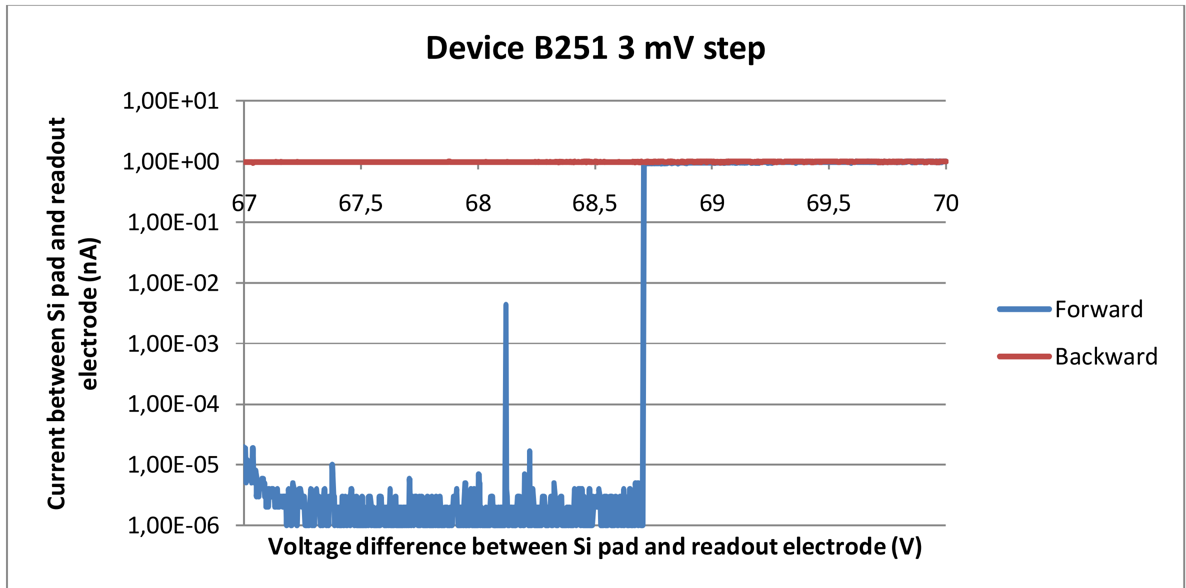
Device B251 3 mV step
Current between Si pad and readout electrode (nA)
1,00E+01
1,00E+00
1,00E-01
1,00E-02
1,00E-03
1,00E-04
1,00E-05
1,00E-06
67
67,5
68
68,5
69
69,5
70
Voltage difference between Si pad and readout electrode (V)
Forward
Backward

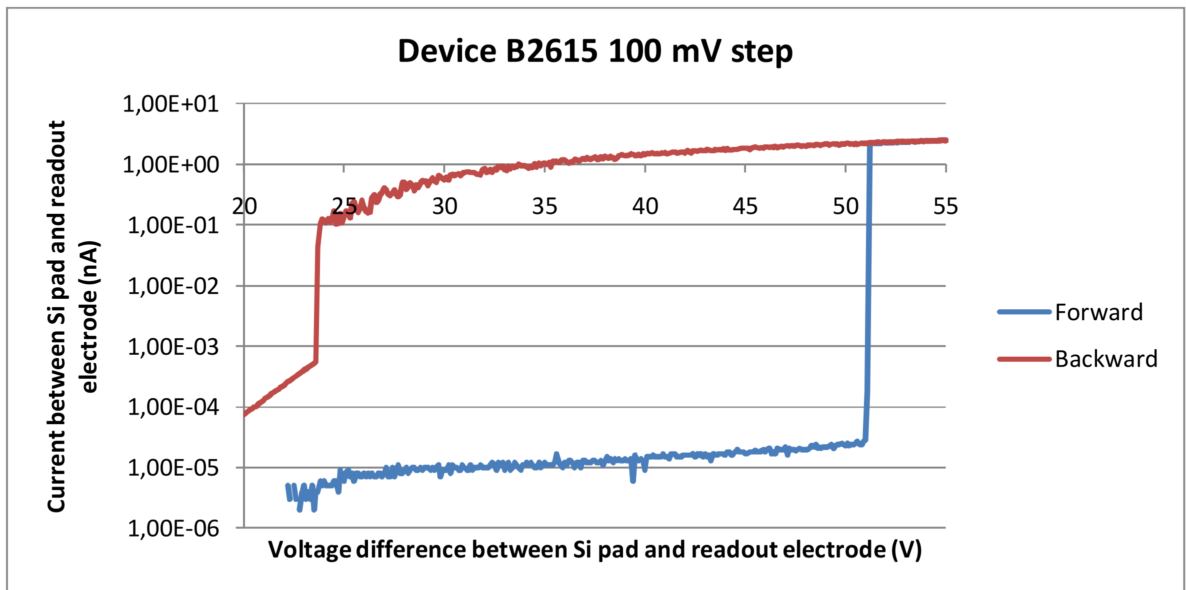
Device B2615 100 mV step
Current between Si pad and readout electrode (nA)
1,00E+01
1,00E+00
1,00E-01
1,00E-02
1,00E-03
1,00E-04
1,00E-05
1,00E-06
20
25
30
35
40
45
50
55
Voltage difference between Si pad and readout electrode (V)
Forward
Backward

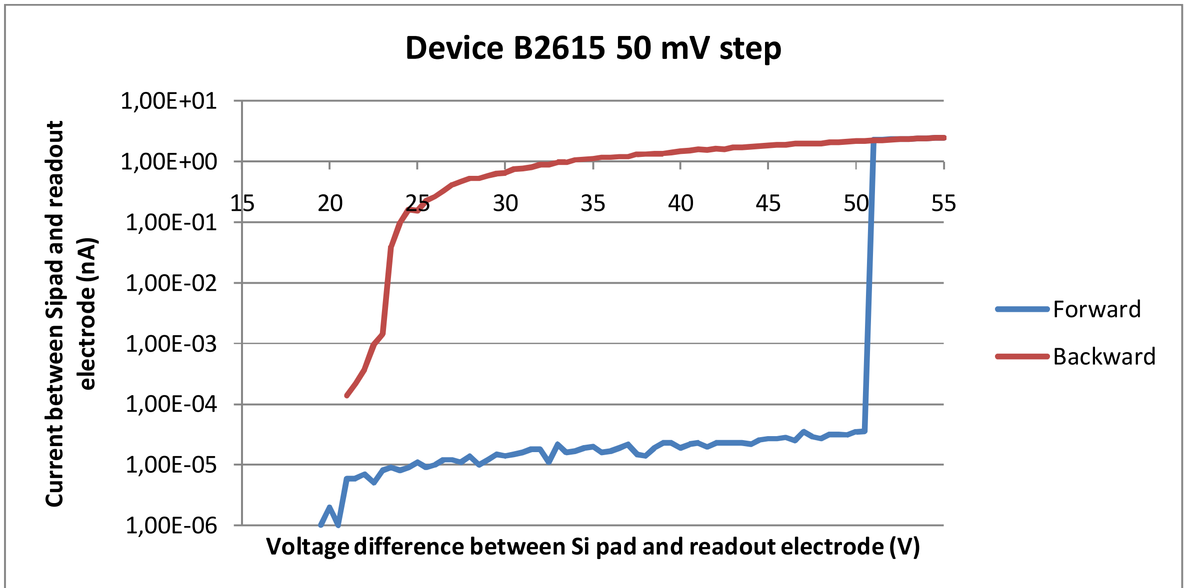
Device B2615 50 mV step
Current between Sipad and readout electrode (nA)
1,00E+01
1,00E+00
1,00E-01
1,00E-02
1,00E-03
1,00E-04
1,00E-05
1,00E-06
15
20
25
30
35
40
45
50
55
Voltage difference between Si pad and readout electrode (V)
Forward
Backward

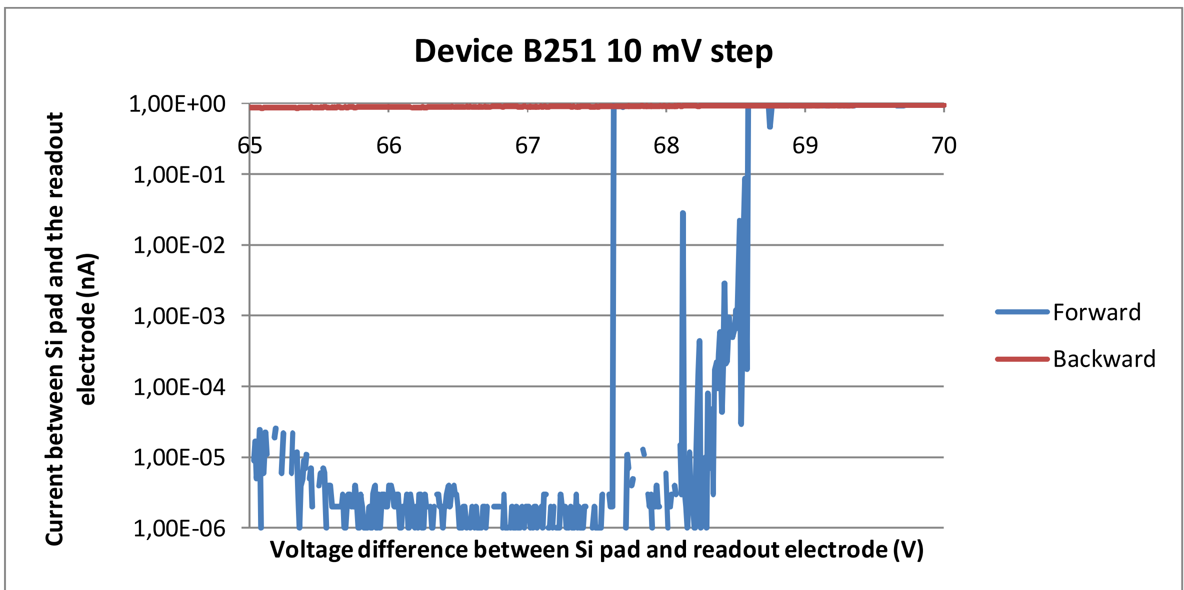
Device B251 10 mV step
Current between Si pad and the readout electrode (nA)
1,00E+00
1,00E-01
1,00E-02
1,00E-03
1,00E-04
1,00E-05
1,00E-06
65
66
67
68
69
70
Voltage difference between Si pad and readout electrode (V)
Forward
Backward

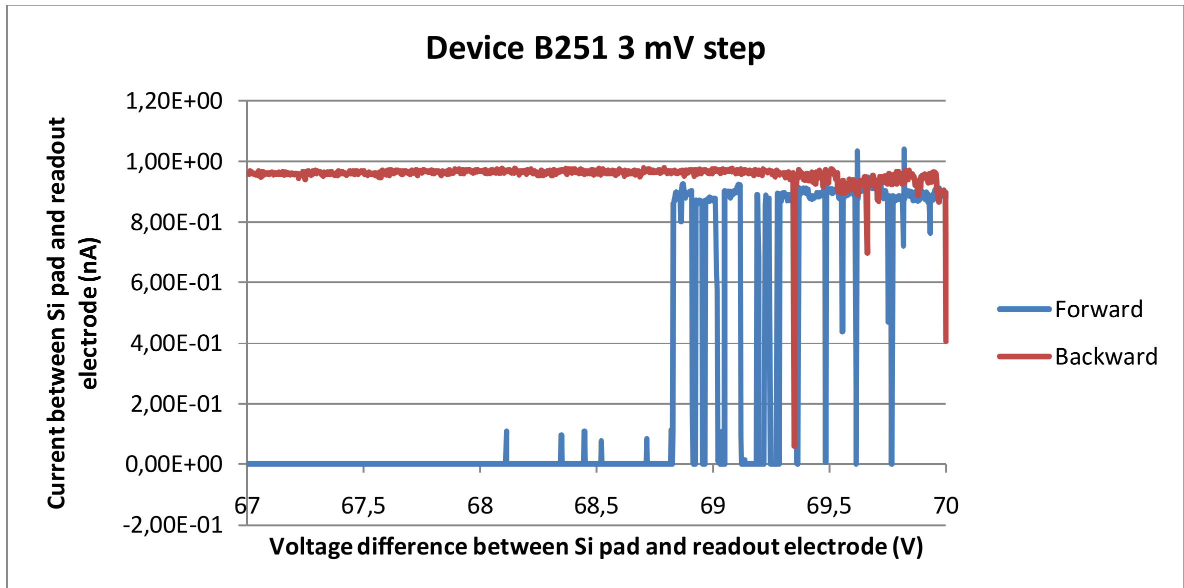
Device B251 3 mV step
1,20E+00
1,00E+00
8,00E-01
6,00E-01
4,00E-01
2,00E-01
0,00E+00
-2,00E-01
67
67,5
68
68,5
69
69,5
70
Current between Si pad and readout electrode (nA)
Voltage difference between Si pad and readout electrode (V)
Forward
Backward

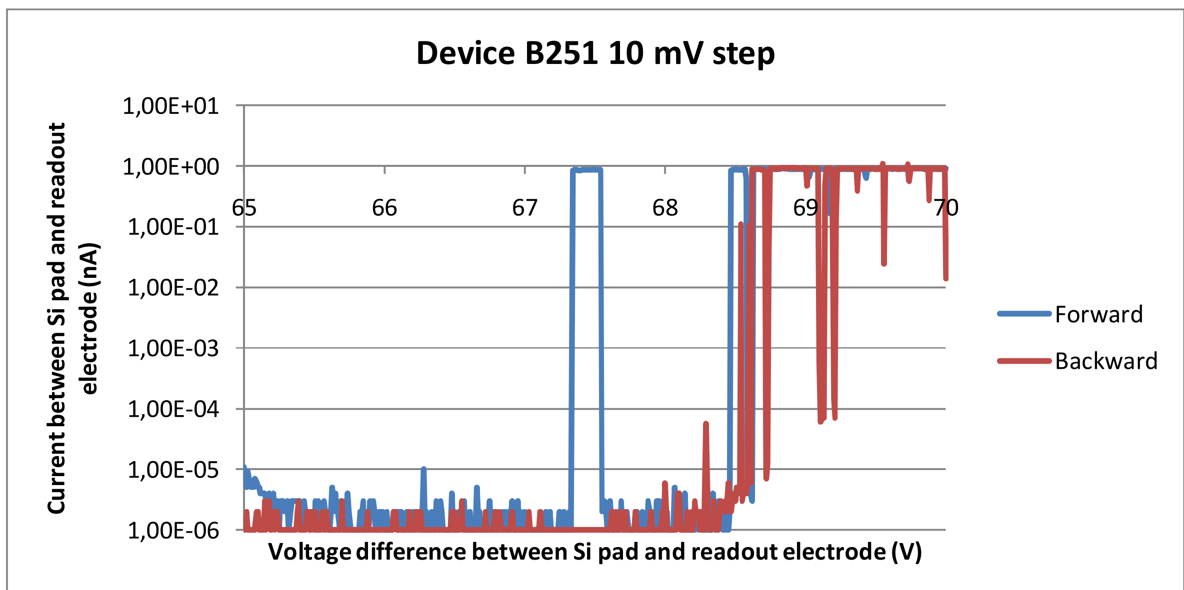
Device B251 10 mV step
1,00E+01
1,00E+00
1,00E-01
1,00E-02
1,00E-03
1,00E-04
1,00E-05
1,00E-06
65
66
67
68
69
70
Current between Si pad and readout electrode (nA)
Voltage difference between Si pad and readout electrode (V)
Forward
Backward

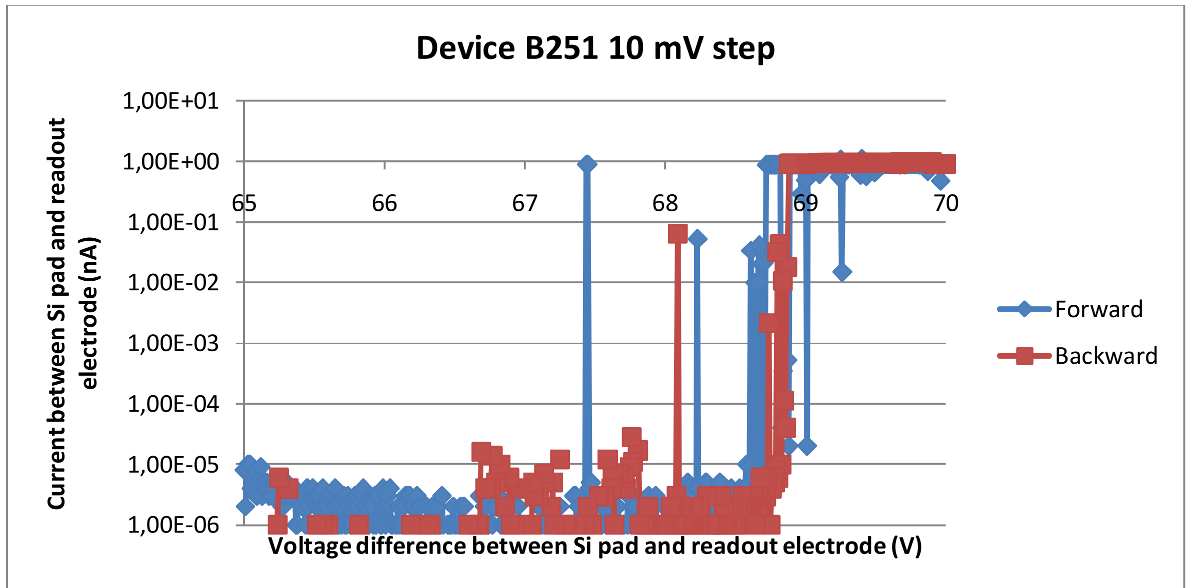
Device B251 10 mV step
Current between Si pad and readout electrode (nA)
1,00E+01
1,00E+00
1,00E-01
1,00E-02
1,00E-03
1,00E-04
1,00E-05
1,00E-06
65
66
67
68
69
70
Voltage difference between Si pad and readout electrode (V)
Forward
Backward

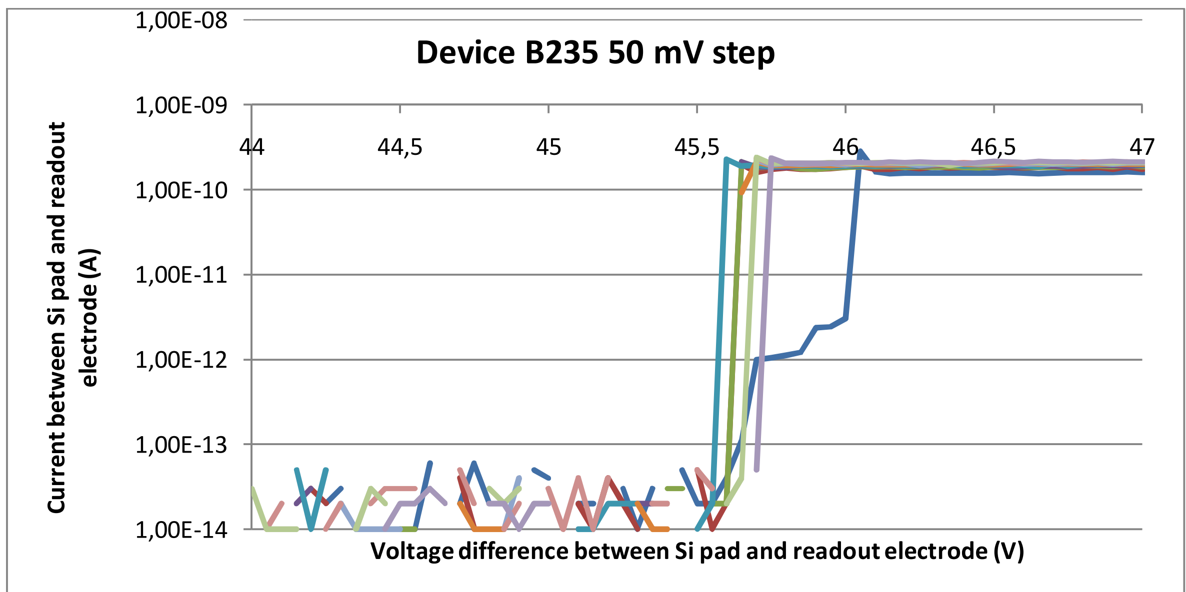
Device B235 50 mV step
Current between Si pad and readout electrode (A)
1,00E-08
1,00E-09
1,00E-10
1,00E-11
1,00E-12
1,00E-13
1,00E-14
44
44,5
45
45,5
46
46,5
47
Voltage difference between Si pad and readout electrode (V)

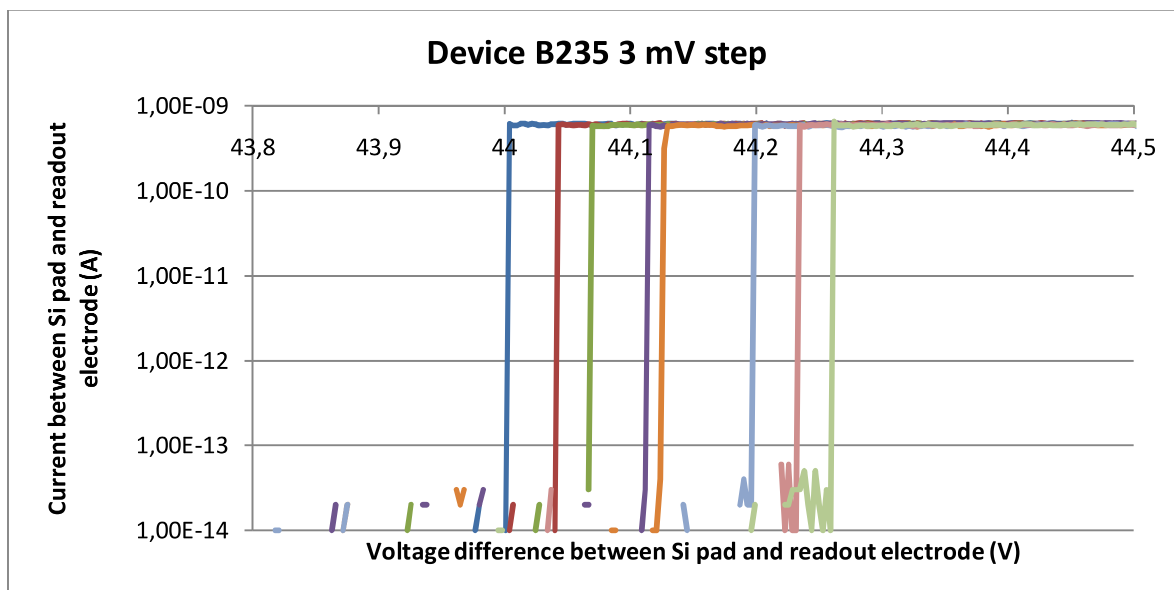
Device B235 3 mV step
1,00E-09
1,00E-10
1,00E-11
1,00E-12
1,00E-13
1,00E-14
43,8
43,9
44
44,1
44,2
44,3
44,4
44,5
Current between Si pad and readout electrode (A)
Voltage difference between Si pad and readout electrode (V)

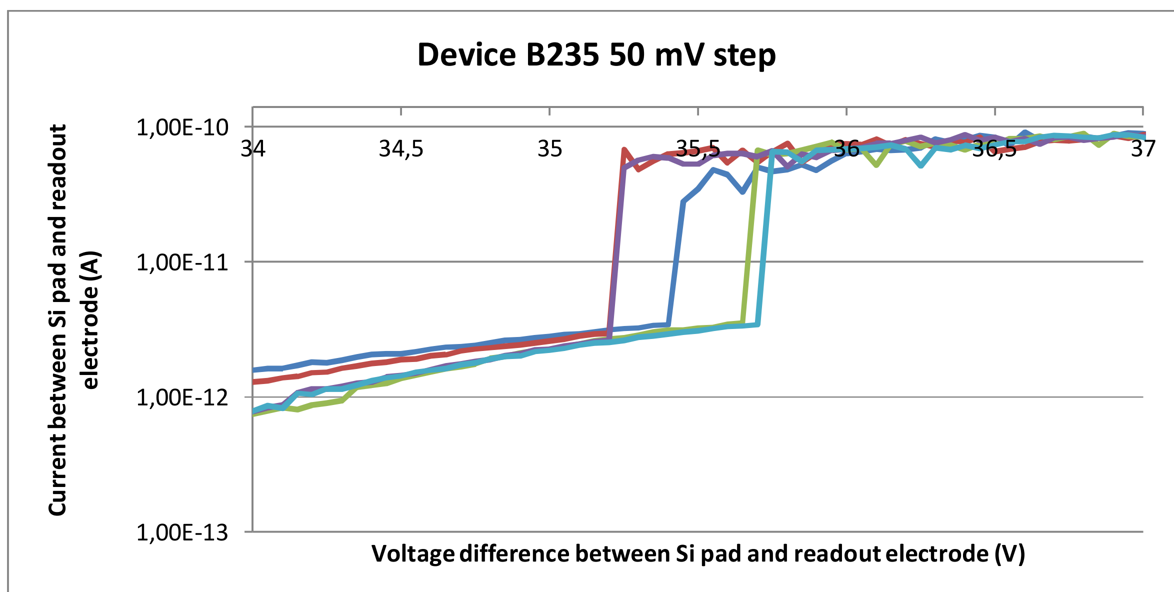
Device B235 50 mV step
1,00E-10
1,00E-11
1,00E-12
1,00E-13
34
34,5
35
35,5
36
36,5
37
Current between Si pad and readout electrode (A)
Voltage difference between Si pad and readout electrode (V)

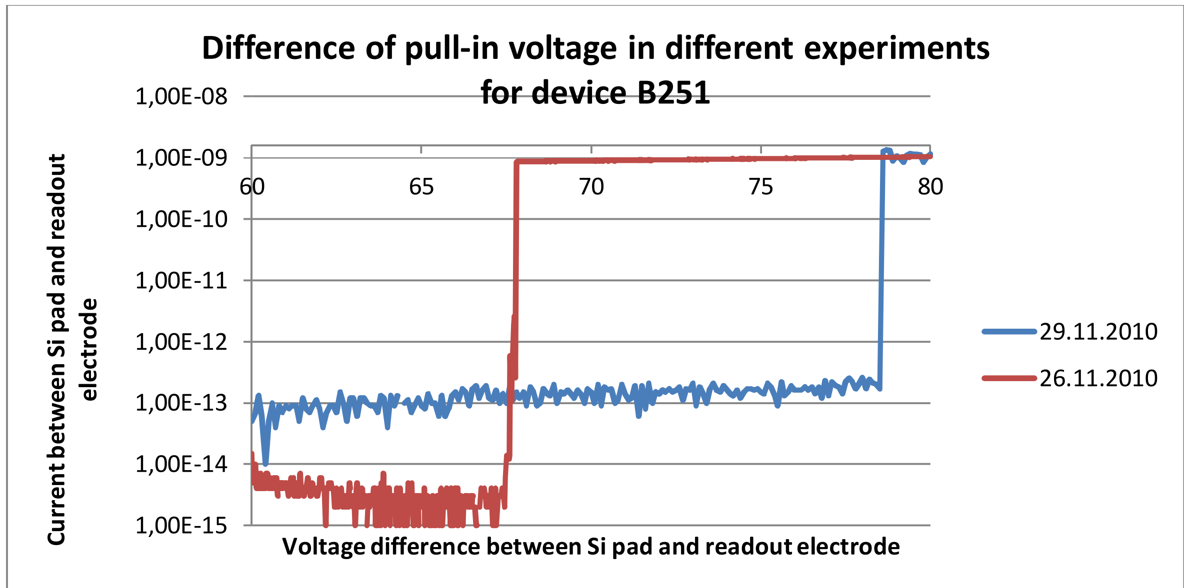
Difference of pull-in voltage in different experiments for device B251
1,00E-08
1,00E-09
1,00E-10
1,00E-11
1,00E-12
1,00E-13
1,00E-14
1,00E-15
60
65
70
75
80
Current between Si pad and readout electrode
Voltage difference between Si pad and readout electrode
29.11.2010
26.11.2010

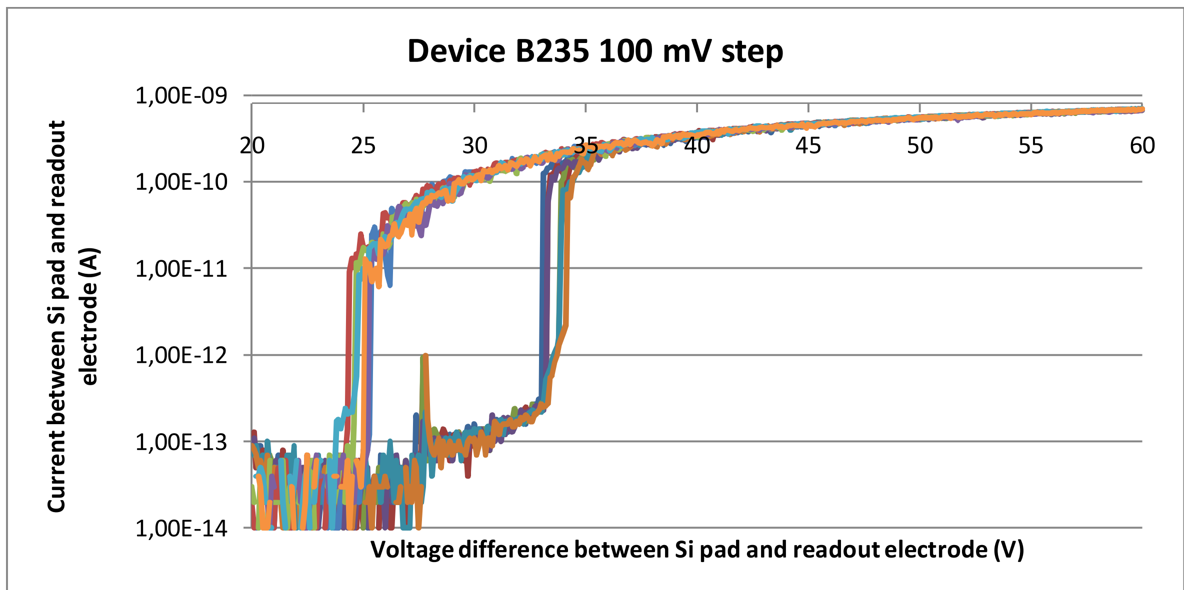
Device B235 100 mV step
1,00E-09
1,00E-10
1,00E-11
1,00E-12
1,00E-13
1,00E-14
20
25
30
35
40
45
50
55
60
Current between Si pad and readout electrode (A)
Voltage difference between Si pad and readout electrode (V)

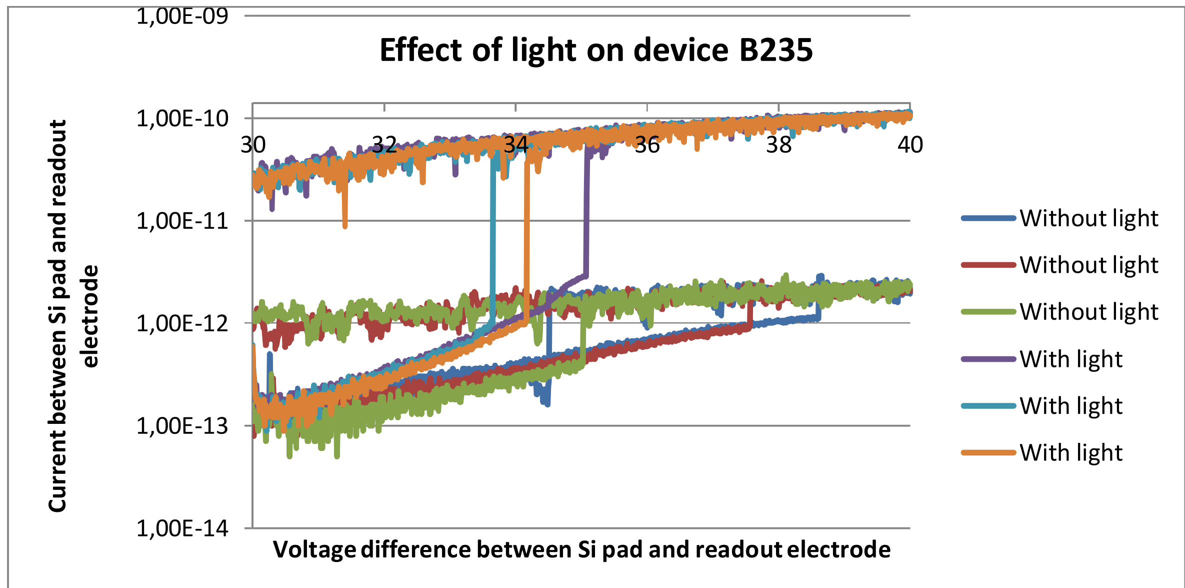
Effect of light on device B235
Current between Si pad and readout electrode
1,00E-09
1,00E-10
1,00E-11
1,00E-12
1,00E-13
1,00E-14
30
32
34
36
38
40
Voltage difference between Si pad and readout electrode
Without light
Without light
Without light
With light
With light
With light

BIBLIOGRAPHY

[1] J. S. Milne, A. C. H. Rowe, S. Arscott, and C. Renner, "Giant Piezoresistance Effects in Silicon Nanowires and Microwires," *Physical Review Letters,* vol. 105, p. 4, Nov 2010.

[2] S. Hoffmann, I. Utke, B. Moser, J. Michler, S. H. Christiansen, V. Schmidt, S. Senz, P. Werner, U. Gosele, and C. Ballif, "Measurement of the bending strength of vapor-liquid-solid grown silicon nanowires," *Nano Letters,* vol. 6, pp. 622-625, Apr 2006.

[3] X. L. Feng, R. R. He, P. D. Yang, and M. L. Roukes, "Very high frequency silicon nanowire electromechanical resonators," *Nano Letters,* vol. 7, pp. 1953-1959, Jul 2007.

[4] I. Yildiz, "Fabrication and Characterization of Silicon Nanowire Resonators," Master of Science, Graduate School of Engineering, Koc University, 2010.

[5] M. F. Yu, O. Lourie, M. J. Dyer, K. Moloni, T. F. Kelly, and R. S. Ruoff, "Strength and breaking mechanism of multiwalled carbon nanotubes under tensile load," *Science,* vol. 287, pp. 637-640, Jan 2000.

[6] T. Kizuka, Y. Takatani, K. Asaka, and R. Yoshizaki, "Measurements of the atomistic mechanics of single crystalline silicon wires of nanometer width," *Physical Review B,* vol. 72, p. 6, Jul 2005.

[7] A. V. Desai and M. A. Haque, "Mechanical properties of ZnO nanowires," *Sensors and Actuators a-Physical,* vol. 134, pp. 169-176, Feb 2007.

[8] A. V. Desai, M. A. Haque, P. C. Eklund, and Asme, "MEMS testbed for mechanical testing of nanowires," in *Micro-Electro-Mechanical Systems - 2005*. vol. 7, ed New York: Amer Soc Mechanical Engineers, 2005, pp. 365-368.

[9] Y. Zhu, N. Moldovan, and H. D. Espinosa, "A microelectromechanical load sensor for in situ electron and x-ray microscopy tensile testing of nanostructures," *Applied Physics Letters,* vol. 86, p. 3, Jan 2005.

[10] H. D. Espinosa, Y. Zhu, and N. Moldovan, "Design and operation of a MEMS-based material testing system for nanomechanical characterization," *Journal of Microelectromechanical Systems,* vol. 16, pp. 1219-1231, Oct 2007.

[11] R. Agrawal, B. Peng, E. E. Gdoutos, and H. D. Espinosa, "Elasticity Size Effects in ZnO Nanowires-A Combined Experimental-Computational Approach," *Nano Letters,* vol. 8, pp. 3668-3674, Nov 2008.

[12] D. F. Zhang, W. Drissen, J. M. Breguet, R. Clavel, and J. Michler, "A high-sensitivity and quasi-linear capacitive sensor for nanomechanical testing applications," *Journal of Micromechanics and Microengineering,* vol. 19, Jul 2009.

[13] H. Hosokawa, A. V. Desai, and M. A. Haque, "Plane stress fracture toughness of freestanding nanoscale thin films," *Thin Solid Films,* vol. 516, pp. 6444-6447, Jul 2008.

[14] M. A. Haque and M. T. A. Saif, "Microscale materials testing using MEMS actuators," *Journal of Microelectromechanical Systems,* vol. 10, pp. 146-152, Mar 2001.

[15] M. A. Haque and M. T. A. Saif, "In-situ tensile testing of nano-scale specimens in SEM and TEM," *Experimental Mechanics,* vol. 42, pp. 123-128, Mar 2002.

[16] J. Gaspar, M. E. Schmidt, J. Held, and O. Paul, "Wafer-Scale Microtensile Testing of Thin Films," *Journal of Microelectromechanical Systems,* vol. 18, pp. 1062-1076, Oct 2009.

[17] Q. H. Jin, T. Li, P. Zhou, and Y. L. Wang, "Mechanical Researches on Young's Modulus of SCS Nanostructures," *Journal of Nanomaterials,* 2009.

[18] D. A. Smith, V. C. Holmberg, D. C. Lee, and B. A. Korgel, "Young's modulus and size-dependent mechanical quality factor of nanoelectromechanical germanium nanowire resonators," *Journal of Physical Chemistry C,* vol. 112, pp. 10725-10729, Jul 2008.

[19] P. Poncharal, Z. L. Wang, D. Ugarte, and W. A. de Heer, "Electrostatic deflections and electromechanical resonances of carbon nanotubes," *Science,* vol. 283, pp. 1513-1516, Mar 1999.

[20] S. Frank, P. Poncharal, Z. L. Wang, and W. A. de Heer, "Carbon nanotube quantum resistors," *Science,* vol. 280, pp. 1744-1746, Jun 1998.

[21] Z. L. Wang, R. P. Gao, Z. W. Pan, and Z. R. Dai, "Nano-scale mechanics of nanotubes, nanowires, and nanobelts," *Advanced Engineering Materials,* vol. 3, pp. 657-661, Sep 2001.

[22] P. Jaroenapibal, D. E. Luzzi, S. Evoy, and S. Arepalli, "Transmission-electron-microscopic studies of mechanical properties of single-walled carbon nanotube bundles," *Applied Physics Letters,* vol. 85, pp. 4328-4330, Nov 2004.

[23] C. Y. Nam, P. Jaroenapibal, D. Tham, D. E. Luzzi, S. Evoy, and J. E. Fischer, "Diameter-dependent electromechanical properties of GaN nanowires," *Nano Letters,* vol. 6, pp. 153-158, Feb 2006.

[24] K. H. Liu, W. L. Wang, Z. Xu, L. Liao, X. D. Bai, and E. G. Wang, "In situ probing mechanical properties of individual tungsten oxide nanowires directly grown on tungsten tips inside transmission electron microscope," *Applied Physics Letters,* vol. 89, p. 3, Nov 2006.

[25] M. Belov, N. J. Quitoriano, S. Sharma, W. K. Hiebert, T. I. Kamins, and S. Evoy, "Mechanical resonance of clamped silicon nanowires measured by optical interferometry," *Journal of Applied Physics,* vol. 103, p. 7, Apr 2008.

[26] M. M. J. Treacy, T. W. Ebbesen, and J. M. Gibson, "Exceptionally high Young's modulus observed for individual carbon nanotubes," *Nature,* vol. 381, pp. 678-680, Jun 1996.

[27] C. Q. Chen, Y. Shi, Y. S. Zhang, J. Zhu, and Y. J. Yan, "Size dependence of Young's modulus in ZnO nanowires," *Physical Review Letters,* vol. 96, p. 4, Feb 2006.

[28] J. P. Salvetat, G. A. D. Briggs, J. M. Bonard, R. R. Bacsa, A. J. Kulik, T. Stockli, N. A. Burnham, and L. Forro, "Elastic and shear moduli of single-walled carbon nanotube ropes," *Physical Review Letters,* vol. 82, pp. 944-947, Feb 1999.

[29] J. P. Salvetat, A. J. Kulik, J. M. Bonard, G. A. D. Briggs, T. Stockli, K. Metenier, S. Bonnamy, F. Beguin, N. A. Burnham, and L. Forro, "Elastic modulus of ordered and disordered multiwalled carbon nanotubes," *Advanced Materials,* vol. 11, pp. 161-165, Jan 1999.

[30] B. Lukic, J. W. Seo, R. R. Bacsa, S. Delpeux, F. Beguin, G. Bister, A. Fonseca, J. B. Nagy, A. Kis, S. Jeney, A. J. Kulik, and L. Forro, "Catalytically grown carbon nanotubes of small diameter have a high Young's modulus," *Nano Letters,* vol. 5, pp. 2074-2077, Oct 2005.

[31] K. M. Lee, B. Lukic, A. Magrez, J. W. Seo, G. A. D. Briggs, A. J. Kulik, and L. Forro, "Diameter-dependent elastic modulus supports the metastable-catalyst growth of carbon nanotubes," *Nano Letters,* vol. 7, pp. 1598-1602, Jun 2007.

[32] L. Sun, R. P. S. Han, J. Wang, and C. T. Lim, "Modeling the size-dependent elastic properties of polymeric nanofibers," *Nanotechnology,* vol. 19, p. 8, Nov 2008.

[33] L. T. Ngo, D. Almecija, J. E. Sader, B. Daly, N. Petkov, J. D. Holmes, D. Erts, and J. J. Boland, "Ultimate-strength germanium nanowires," *Nano Letters,* vol. 6, pp. 2964-2968, Dec 2006.

[34] B. Wu, A. Heidelberg, J. J. Boland, J. E. Sader, X. M. Sun, and Y. D. Li, "Microstructure-hardened silver nanowires," *Nano Letters,* vol. 6, pp. 468-472, Mar 2006.

[35] A. Heidelberg, L. T. Ngo, B. Wu, M. A. Phillips, S. Sharma, T. I. Kamins, J. E. Sader, and J. J. Boland, "A generalized description of the elastic properties of nanowires," *Nano Letters,* vol. 6, pp. 1101-1106, Jun 2006.

[36] Q. H. Xiong, N. Duarte, S. Tadigadapa, and P. C. Eklund, "Force-deflection spectroscopy: A new method to determine the Young's modulus of nanofilaments," *Nano Letters,* vol. 6, pp. 1904-1909, Sep 2006.

[37] M. P. Manoharan, A. V. Desai, G. Neely, and M. A. Haque, "Synthesis and elastic characterization of zinc oxide nanowires," *Journal of Nanomaterials,* 2008.

[38] S. Hoffmann, F. Ostlund, J. Michler, H. J. Fan, M. Zacharias, S. H. Christiansen, and C. Ballif, "Fracture strength and Young's modulus of ZnO nanowires," *Nanotechnology,* vol. 18, May 2007.

[39] M. J. Gordon, T. Baron, F. Dhalluin, P. Gentile, and P. Ferret, "Size Effects in Mechanical Deformation and Fracture of Cantilevered Silicon Nanowires," *Nano Letters,* vol. 9, pp. 525-529, Feb 2009.

[40] S. G. Nilsson, X. Borrise, and L. Montelius, "Size effect on Young's modulus of thin chromium cantilevers," *Applied Physics Letters,* vol. 85, pp. 3555-3557, Oct 2004.

[41] E. W. Wong, P. E. Sheehan, and C. M. Lieber, "Nanobeam mechanics: Elasticity, strength, and toughness of nanorods and nanotubes," *Science,* vol. 277, pp. 1971-1975, Sep 1997.

[42] Y. Zhu and H. D. Espinosa, "An electromechanical material testing system for in situ electron microscopy and applications," *Proceedings of the National Academy of Sciences of the United States of America,* vol. 102, pp. 14503-14508, Oct 2005.

[43] C. W. Baek, Y. K. Kim, Y. Ahn, and Y. H. Kim, "Measurement of the mechanical properties of electroplated gold thin films using micromachined beam structures," *Sensors and Actuators a-Physical,* vol. 117, pp. 17-27, Jan 2005.

[44] L. W. Lin, A. P. Pisano, and R. T. Howe, "A micro strain gauge with mechanical amplifier," *Journal of Microelectromechanical Systems,* vol. 6, pp. 313-321, Dec 1997.

[45] F. Ericson, S. Greek, J. Soderkvist, and J. A. Schweitz, "High-sensitivity surface micromachined structures for internal stress and stress gradient evaluation," *Journal of Micromechanics and Microengineering,* vol. 7, pp. 30-36, Mar 1997.

[46] L. S. Fan, R. S. Muller, W. J. Yun, R. T. Howe, J. H. Huang, and Ieee, *SPIRAL MICROSTRUCTURES FOR THE MEASUREMENT OF AVERAGE STRAIN GRADIENTS IN THIN-FILMS*, 1990.

[47] C. J. Li, "Measurement of mean and gradient residual stresses in thin films using spiral microstructures," *Sensors and Actuators a-Physical,* vol. 155, pp. 181-187, Oct 2009.

[48] H. Seidel, L. Csepregi, A. Heuberger, and H. Baumgartel, "ANISOTROPIC ETCHING OF CRYSTALLINE SILICON IN ALKALINE-SOLUTIONS .1. ORIENTATION DEPENDENCE AND BEHAVIOR OF PASSIVATION LAYERS," *Journal of the Electrochemical Society,* vol. 137, pp. 3612-3626, Nov 1990.

[49] D. F. Zhang, J. M. Breguet, R. Clavel, L. Philippe, I. Utke, and J. Michler, "In situ tensile testing of individual Co nanowires inside a scanning electron microscope," *Nanotechnology,* vol. 20, Sep 2009.

[50] D. W. Carr, L. Sekaric, and H. G. Craighead, "Measurement of nanomechanical resonant structures in single-crystal silicon," *Journal of Vacuum Science & Technology B,* vol. 16, pp. 3821-3824, Nov-Dec 1998.

[51] X. M. Lu, T. Hanrath, K. P. Johnston, and B. A. Korgel, "Growth of single crystal nanowires in supercritical silicon solution from tethered gold particles on a silicon substrate," *Nano Letters,* vol. 3, pp. 93-99, Jan 2003.

[52] Y. Wu, Y. Cui, L. Huynh, C. J. Barrelet, D. C. Bell, and C. M. Lieber, "Controlled growth and structures of molecular-scale silicon nanowires," *Nano Letters,* vol. 4, pp. 433-436, Mar 2004.

[53] D. J. Zeng, X. L. Wei, J. Z. Liu, Q. Chen, X. D. Li, and Q. S. Zheng, "Tunable resonant frequencies for determining Young's moduli of nanowires," *Journal of Applied Physics,* vol. 105, p. 4, Jun 2009.

[54] D. W. Carr, S. Evoy, L. Sekaric, H. G. Craighead, and J. M. Parpia, "Measurement of mechanical resonance and losses in nanometer scale silicon wires," *Applied Physics Letters,* vol. 75, pp. 920-922, Aug 1999.

[55] I. De Vlaminck, J. Roels, D. Taillaert, D. Van Thourhout, R. Baets, L. Lagae, and G. Borghs, "Detection of nanomechanical motion by evanescent light wave coupling," *Applied Physics Letters,* vol. 90, p. 3, Jun 2007.

[56] S. S. Verbridge, L. M. Bellan, J. M. Parpia, and H. G. Craighead, "Optically driven resonance of nanoscale flexural oscillators in liquid," *Nano Letters,* vol. 6, pp. 2109-2114, Sep 2006.

[57] D. Galayko, A. Kaiser, L. Buchaillot, B. Legrand, D. Collard, and C. Combi, "Design, realization and testing of micro-mechanical resonators in thick-film silicon technology with postprocess electrode-to-resonator gap reduction," *Journal of Micromechanics and Microengineering,* vol. 13, pp. 134-140, Jan 2003.

[58] E. Colinet, C. Durand, L. Duraffourg, P. Audebert, G. Dumas, F. Casset, E. Ollier, P. Ancey, J. F. Carpentier, L. Buchaillot, and A. M. Ionescu, "Ultra-Sensitive Capacitive Detection Based on SGMOSFET Compatible With Front-End CMOS Process," *Ieee Journal of Solid-State Circuits,* vol. 44, pp. 247-257, Jan 2009.

[59] H. Krommer, A. Erbe, A. Tilke, S. Manus, and R. H. Blick, "Nanomechanical resonators operating as charge detectors in the nonlinear regime," *Europhysics Letters,* vol. 50, pp. 101-106, Apr 2000.

[60] M. Tabib-Azar, M. Nassirou, R. Wang, S. Sharma, T. I. Kamins, M. S. Islam, and R. S. Williams, "Mechanical properties of self-welded silicon nanobridges," *Applied Physics Letters,* vol. 87, p. 3, Sep 2005.

[61] B. Ilic, S. Krylov, L. M. Bellan, H. G. Craighead, and Ieee, "Dynamic characterization of nano oscillators by atomic force microscopy," in *Proceedings of the Ieee Twentieth Annual International Conference on Micro Electro Mechanical Systems, Vols 1 and 2*, ed New York: Ieee, 2007, pp. 286-289.

[62] J. M. Nichol, E. R. Hemesath, L. J. Lauhon, and R. Budakian, "Displacement detection of silicon nanowires by polarization-enhanced fiber-optic interferometry," *Applied Physics Letters,* vol. 93, p. 3, Nov 2008.

[63] R. R. He, X. L. Feng, M. L. Roukes, and P. D. Yang, "Self-transducing silicon nanowire electromechanical systems at room temperature," *Nano Letters,* vol. 8, pp. 1756-1761, Jun 2008.

[64] M. W. Li, R. B. Bhiladvala, T. J. Morrow, J. A. Sioss, K. K. Lew, J. M. Redwing, C. D. Keating, and T. S. Mayer, "Bottom-up assembly of large-area nanowire resonator arrays," *Nature Nanotechnology,* vol. 3, pp. 88-92, Feb 2008.

[65] E. Mile, G. Jourdan, I. Bargatin, S. Labarthe, C. Marcoux, P. Andreucci, S. Hentz, C. Kharrat, E. Colinet, and L. Duraffourg, "In-plane nanoelectromechanical resonators based on silicon nanowire piezoresistive detection," *Nanotechnology,* vol. 21, p. 7, Apr 2010.

[66] Q. L. Li, S. M. Koo, M. D. Edelstein, J. S. Suehle, and C. A. Richter, "Silicon nanowire electromechanical switches for logic device application," *Nanotechnology,* vol. 18, p. 5, Aug 2007.

[67] S. N. Cha, J. E. Jang, Y. Choi, G. A. J. Amaratunga, D. J. Kang, D. G. Hasko, J. E. Jung, and J. M. Kim, "Fabrication of a nanoelectromechanical switch using a suspended carbon nanotube," *Applied Physics Letters,* vol. 86, p. 3, Feb 2005.

[68] J. E. Jang, S. N. Cha, Y. J. Choi, D. J. Kang, T. P. Butler, D. G. Hasko, J. E. Jung, J. M. Kim, and G. A. J. Amaratunga, "Nanoscale memory cell based on a nanoelectromechanical switched capacitor," *Nature Nanotechnology,* vol. 3, pp. 26-30, Jan 2008.

[69] A. B. Kaul, E. W. Wong, L. Epp, and B. D. Hunt, "Electromechanical carbon nanotube switches for high-frequency applications," *Nano Letters,* vol. 6, pp. 942-947, May 2006.

[70] K. J. Ziegler, D. M. Lyons, J. D. Holmes, D. Erts, B. Polyakov, H. Olin, K. Svensson, and E. Olsson, "Bistable nanoelectromechanical devices," *Applied Physics Letters,* vol. 84, pp. 4074-4076, May 2004.

[71] Q. L. Li, S. M. Koo, C. A. Richter, M. D. Edelstein, J. E. Bonevich, J. J. Kopanski, J. S. Suehle, and E. M. Vogel, "Precise alignment of single nanowires and fabrication of nanoelectromechanical switch and other test structures," *Ieee Transactions on Nanotechnology,* vol. 6, pp. 256-262, Mar 2007.

[72] Q. L. Li, S. M. Koo, H. D. Xiong, M. D. Edelstein, J. S. Suehle, X. X. Zhu, D. E. Ioannou, and C. A. Richter, "Methods to characterize the electrical and mechanical properties of Si nanowires," in *Frontiers of Characterization and Metrology for Nanoelectronics: 2007*. vol. 931, D. G. Seiler, A. C. Diebold, R. McDonald, C. M. Garner, D. Herr, R. P. Khosla, and E. M. Secula, Eds., ed Melville: Amer Inst Physics, 2007, pp. 457-461.

[73] H. J. Fan, P. Werner, and M. Zacharias, "Semiconductor nanowires: From self-organization to patterned growth," *Small,* vol. 2, pp. 700-717, Jun 2006.

[74] X. M. H. Huang, X. L. Feng, C. A. Zorman, M. Mehregany, and M. L. Roukes, "VHF, UHF and microwave frequency nanomechanical resonators," *New Journal of Physics,* vol. 7, Nov 2005.

[75] T. Toriyama, Y. Tanimoto, and S. Sugiyama, "Single crystal silicon nano-wire piezoresistors for mechanical sensors," *Journal of Microelectromechanical Systems,* vol. 11, pp. 605-611, Oct 2002.

[76] J. Kedzierski, J. Bokor, and C. Kisielowski, "Fabrication of planar silicon nanowires on silicon-on-insulator using stress limited oxidation," *Journal of Vacuum Science & Technology B,* vol. 15, pp. 2825-2828, Nov-Dec 1997.

[77] V. Milanovic, L. Doherty, D. A. Teasdale, S. Parsa, and K. S. J. Pister, "Micromachining technology for lateral field emission devices," *Ieee Transactions on Electron Devices,* vol. 48, pp. 166-173, Jan 2001.

[78] N. Singh, A. Agarwal, L. K. Bera, T. Y. Liow, R. Yang, S. C. Rustagi, C. H. Tung, R. Kumar, G. Q. Lo, N. Balasubramanian, and D. L. Kwong, "High-performance fully depleted silicon-nanowire (diameter <= 5 nm) gate-all-around CMOS devices," *Ieee Electron Device Letters,* vol. 27, pp. 383-386, May 2006.

[79] K. D. Buddharaju, N. Singh, S. C. Rustagi, S. H. G. Teo, G. Q. Lo, N. Balasubramanian, and D. L. Kwong, "Si-nanowire CMOS inverter logic fabricated using gate-all-around (GAA) devices and top-down approach," *Solid-State Electronics,* vol. 52, pp. 1312-1317, Sep 2008.

[80] S. C. Rustagi, N. Singh, Y. F. Lim, G. Zhang, S. Wang, G. Q. Lo, N. Balasubramanian, and D. L. Kwong, "Low-temperature transport characteristics and quantum-confinement effects in gate-all-around Si-nanowire N-MOSFET," *Ieee Electron Device Letters,* vol. 28, pp. 909-912, Oct 2007.

[81] K. E. Moselund, D. Bouvet, M. H. Ben Jamaa, D. Atienza, Y. Leblebici, G. De Micheli, and A. M. Ionescu, "Prospects for logic-on-a-wire," *Microelectronic Engineering,* vol. 85, pp. 1406-1409, May-Jun 2008.

[82] V. Pott, K. E. Moselund, D. Bouvet, L. De Michielis, and A. M. Ionescu, "Fabrication and Characterization of Gate-All-Around Silicon Nanowires on Bulk Silicon," *Ieee Transactions on Nanotechnology,* vol. 7, pp. 733-744, Nov 2008.

[83] Y. J. Ai, R. Huang, Z. H. Hao, C. H. Fan, R. S. Wang, S. S. Pu, and Y. Y. Wang, "Top-down fabrication of shape controllable Si nanowires based on conventional CMOS process," *Physica E-Low-Dimensional Systems & Nanostructures,* vol. 43, pp. 102-105, Nov 2010.

[84] Y. Song, H. J. Zhou, Q. X. Xu, J. B. Niu, J. A. Yan, C. Zhao, and H. C. Zhong, "High-Performance Silicon Nanowire Gate-All-Around nMOSFETs Fabricated on

Bulk Substrate Using CMOS-Compatible Process," *Ieee Electron Device Letters,* vol. 31, pp. 1377-1379, Dec 2010.

[85] L. Doherty, H. B. Liu, V. Milanovic, and I. I. Ieee, *Application of MEMS technologies to nanodevices*, 2003.

[86] R. M. Y. Ng, T. Wang, M. Chan, and Ieee, "A. new approach to fabricate vertically stacked single-crystalline silicon nanowires," in *Edssc: 2007 Ieee International Conference on Electron Devices and Solid-State Circuits, Vols 1 and 2, Proceedings*, ed, 2007, pp. 133-136.

[87] R. M. Y. Ng, T. Wang, F. Liu, X. Zuo, J. He, and M. S. Chan, "Vertically Stacked Silicon Nanowire Transistors Fabricated by Inductive Plasma Etching and Stress-Limited Oxidation," *Ieee Electron Device Letters,* vol. 30, pp. 520-522, May 2009.

[88] O. Ozsun, B. E. Alaca, Y. Leblebici, A. D. Yalcinkaya, I. Yildiz, M. Yilmaz, and M. Zervas, "Monolithic Integration of Silicon Nanowires With a Microgripper," *Journal of Microelectromechanical Systems,* vol. 18, pp. 1335-1344, Dec 2009.

[89] M. Bopp, P. Coronel, C. Hibert, and A. M. Ionescu, "3D stacked arrays of fins and nanowires on bulk silicon," *Microelectronic Engineering,* vol. 87, pp. 1348-1351, May-Aug 2010.

[90] C. Liu, *Foundations of MEMS*: Pearson Education Inc., 2006.

[91] S. Pamidighantam, R. Puers, K. Baert, and H. A. C. Tilmans, "Pull-in voltage analysis of electrostatically actuated beam structures with fixed-fixed and fixed-free end conditions," *Journal of Micromechanics and Microengineering,* vol. 12, pp. 458-464, Jul 2002.